UNIVERSITÀ DEGLI STUDI DI PADOVA

DIPARTIMENTO DI FISICA E ASTRONOMIA GALILEO GALILEI

CORSO DI LAUREA MAGISTRALE IN FISICA

Investigation of ELISE beam properties by means of the diagnostic calorimeter

Relatore:
Dr. Gianluigi Serianni

Correlatore:
Prof. Dr. - Ing. Ursel Fantz

Controrelatore:
Dr. Andrea Pisent

Laureando:
Antonio Pimazzoni

16 Settembre 2014
Anno Accademico 2013-2014

Abstract

Neutral particle beams are used as auxiliary heating and current drive system for thermonuclear plasma of deuterium and tritium magnetically confined in a toroidal geometry. Two high power beams of 16.5 MW each, will be used at ITER, the international experiment on nuclear fusion under realisation in Cadarache (France).

In the last years a huge effort was dedicated to improving the understanding of the physics of neutral beam injectors (NBI) based on negative ion sources, since negative ions allow to reach higher beam energies (1 MeV is the ITER requirement) while keeping an acceptable neutralisation efficiency. The ion source that will be used for ITER NBI is an RF source, based on the prototype developed at Institut für Plasmaphysik (IPP) in the last decades.

This thesis focuses on the characterisation of the beam properties, in particular divergence and homogeneity, of the IPP test facility ELISE in different operational conditions. ELISE represents an important step in the development of NBI for ITER, since the extraction area of its ion source (about 1000 cm^2, i.e. half the size required for an ITER NBI) is much larger than the one of other existing RF sources, allowing to investigate phenomena which could be less evident on a small scale.

The study has been performed by means of the ELISE diagnostic calorimeter. The main function of the calorimeter is to stop the beam, but it is also equipped with thermocouples and is observed by an infrared camera in order to determine the beam power deposition profile. The contents of the thesis chapters are shortly listed below.

A brief introduction on nuclear fusion and on the neutral beam injectors is given in *Chapter 1*, discussing the use of plasmas, the main features of ITER and the necessity of additional heating systems. *Chapter 2* focuses on the neutral beam injectors (NBI) presenting their main elements. In particular the IPP prototype RF source is introduced and the main properties of beam optics are discussed. The test facility ELISE is described in *Chapter 3*, where a dedicated section is used to discuss the features of its beam diagnostics: the tungsten wire calorimeter, the beam emission spectroscopy (BES) and, in particular, the diagnostic calorimeter.

Chapter 4 moves into the calibration of the IR camera by correcting the image perspective and determining the emissivity value of the calorimeter surface, which is coated with a blackening layer to reduce its reflectivity. Additionally, a comparison between IR thermography and water calorimetry of the calorimeter is performed.The analysis performed on the IR images in order to determine beam divergence and homogeneity is described in *Chapter 5*. In *Chapter 6* the main results about beam optics are discussed and in particular the divergence evaluation is compared with the one from beam emission spectroscopy (BES), which is currently the diagnostic providing the divergence measurement. The discussion about beam homogeneity is the main topic of *Chapter 7*. Finally the main results and the possible future developments are discussed in *Chapter 8*.

Sommario

Fasci di particelle neutre vengono utilizzati in plasmi termonucleari di deuterio e trizio confinati magneticamente in una geometria toroidale, con il duplice scopo di fornire riscaldamento addizionale e indurre una corrente. Due fasci di potenza da 16.5 MW ciascuno, per esempio, saranno utilizzati per ITER, l'esperimento internazionale sulla fusione che verrà realizzato a Cadarache (Francia).

Negli ultimi anni molti sforzi sono stati profusi per incrementare la comprensione della fisica degli iniettori di particelle neutre (NBI) basati su sorgenti di ioni negativi. L'interesse verso questi ultimi nasce dal fatto che l'efficienza di neutralizzazione per un fascio di ioni negativi resta sufficientemente elevata (circa il 60 %) anche per energie molto grandi (1 MeV è il requisito per ITER). La sorgente di ioni che verrà utilizzata per il NBI di ITER è una sorgente RF, basata sul prototipo sviluppato all'Institut für PlasmaPhysik (IPP) negli ultimi decenni.

Questa tesi si concentra sulla caratterizzazione delle proprietà del fascio della test facility ELISE di IPP in varie condizioni sperimentali. In particolare l'interesse è rivolto a divergenza e omogeneità. ELISE rappresenta un passo importante nello sviluppo degli iniettori di particelle neutre per ITER, siccome l'area di estrazione della sua sorgente di ioni (circa 1000 cm^2, cioè più o meno metà di quella richiesta per un NBI di ITER) è molto più grande di quella delle altre sorgenti a radiofrequenza attualmente utilizzate, e ciò consente di investigare fenomeni che potrebbero essere meno evidenti su scale più piccole.

Lo studio è stato svolto per mezzo del calorimetro diagnostico. La sua funzione principale è fermare il fascio, ma esso è anche equipaggiato con delle termocoppie ed osservato con una termocamera a infrarossi (IR) per determinare la potenza depositata dal fascio sulla sua superficie. I contenuti dei capitoli di questa tesi sono descritti brevemente di seguito.

Una breve introduzione sulla fusione nucleare e sugli iniettori di particelle neutre è fornita nel *Capitolo 1*, dove vengono discussi l'utilizzo dei plasmi, le principali caratteristiche di ITER e la necessità di riscaldamento addizionale. Il *Capitolo 2* è incentrato sugli iniettori di particelle neutre introducendo i loro elementi principali. In particolare viene presentato il prototipo di sorgente RF di IPP e vengono discusse le principali proprietà dell'ottica del fascio.

La test facility ELISE è descritta nel *Capitolo 3*, in cui una sezione è appositamente dedicata alle diagnostiche del fascio: il calorimetro a fili di tungsteno, la spettroscopia Doppler (BES) e, in particolare, il calorimetro diagnostico. Nel *Capitolo 4* è trattata la calibrazione della camera IR, ottenuta correggendo la prospettiva dell'immagine e determinando l'emissività della superficie del calorimetro diagnostico, che è stata ricoperta da uno strato scurente al fine di ridurne la riflettività. Inoltre, viene eseguito un confronto tra la deposizione di potenza stimata dalla termografia IR e dalla calorimetria dell'acqua del circuito di raffreddamento.

L'analisi effettuata sulle immagini IR per determinare divergenza e omogeneità è descritta nel *Capitolo 5*. Nel *Capitolo 6* sono discussi i principali risultati sull'ottica del fascio e, in particolare, la stima della divergenza è confrontata con quella della spettroscopia Doppler, la diagnostica attualmente utilizzata per determinarla. La discussione sull'omogeneità è l'argomento principale del *Capitolo 7*. Infine i principali risultati e i possibili sviluppi futuri sono presentati nel *Capitolo 8*.

Contents

1 Introduction

1.1 Nuclear fusion and plasmas

The continuous and rapid increase of energy demand suggests searching for new energy sources. Fossil fuels, which are largely exploited, have in fact two big drawbacks: their amount is limited and their burning creates different toxic gases, increasing pollution. A promising candidate to be a reliable and clean new energy source with nearly inexhaustible fuel reserves is nuclear fusion.

Two light nuclei fuse together if they come to a very short distance from each other, so that the nuclear force is stronger than the Coulomb repulsion. For this purpose, a very high kinetic energy must be provided, but their fusion releases energy. As it may be seen on the left side of Figure 1 in fact, the fusion of two light nuclei in a heavier one (ligther than Fe) corresponds to an increase in the binding energy (which is negative), i.e. to an energy release.

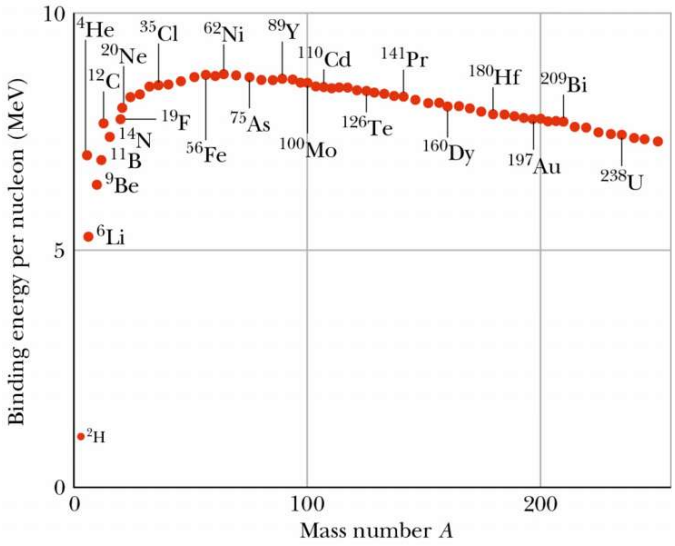

Figure 1: Binding energy per nucleon for different elements.

The most convenient fusion reaction to be realised is between two hydrogen isotopes, deuterium and tritium, since, as it may be seen in Figure 2, it has the highest cross section among the possible reactions.

The detailed reaction is the following

$$\mathrm{D} + \mathrm{T} \rightarrow {}^{4}\mathrm{He} + \mathrm{n} + 17.6\ \mathrm{MeV} \tag{1}$$

The released energy of 17.6 MeV is divided between the two products according to the inverse of their mass ratio: the helium nucleus carries 3.5 MeV, while the neutron carries 14.1 MeV.

Deuterium is available in seawater (30 g/m^3) whereas tritium is not a stable isotope and its lifetime is short (half life = 12.3 years), so it is not obtained in large quantity in nature. In a fusion reactor tritium will be obtained from lithium by the reaction

$$\mathrm{n} + {}^{6}\mathrm{Li} \rightarrow {}^{4}\mathrm{He} + \mathrm{T} + 4.8\ \mathrm{MeV} \tag{2}$$

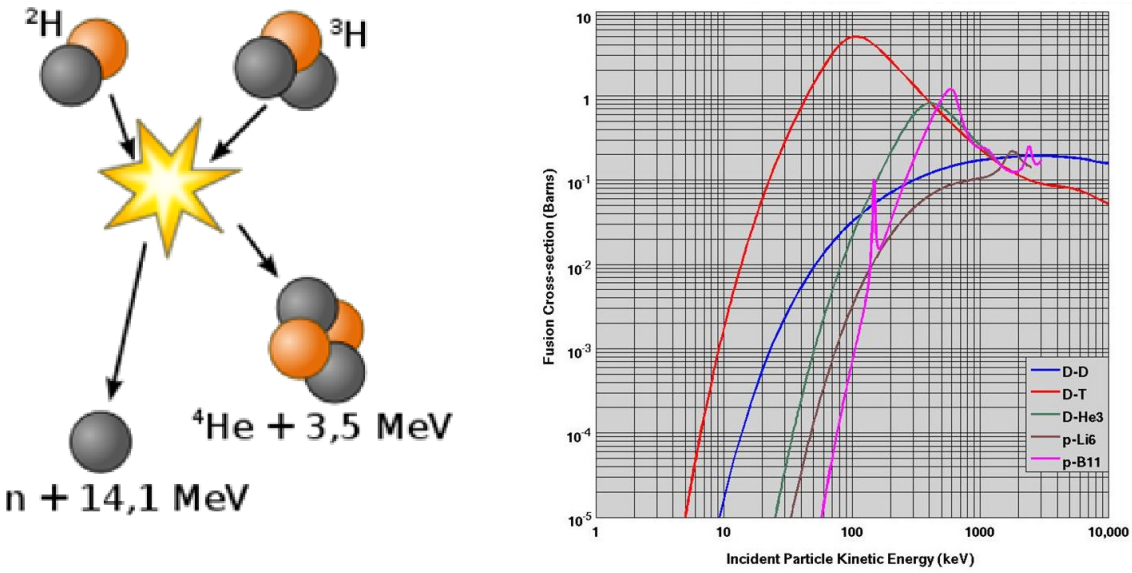

Figure 2: Left: Illustration of a fusion reaction between deuterium and tritium. Right: Cross section of various fusion reactions as a function of the kinetic energy of D (or p) impinging on a stationary target [1].

So the real fuels for a fusion power plant are deuterium and lithium; the latter is available in the earth crust [1].

The main advantage of nuclear fusion, with respect to fission, lies in its passive safety: it is so hard to achieve and sustain the physical conditions necessary for fusion (see below), that in any case of anomalous operation of the fusion device, it would be easy to stop it without consequences over a big scale. In addition, the nuclear waste produced by neutron activation of the materials composing the fusion device have a much shorter lifetime (some decades).

In order to have a sufficiently high reaction rate, high temperatures ($\sim 10^8$ K) must be achieved. In these physical conditions, matter is in plasma state.

A plasma is a collection of charged and neutral particles, which exhibit a collective behaviour. It may be created by heating a gas until atoms separate into electrons and positive ions and its formation is easier as temperature increases and pressure decreases. A plasma is quasi-neutral and any charge inside it is shielded by the plasma itself over a short distance, characterized by the so-called Debye length λ_D (Eq. 3)[2]

$$\lambda_\mathrm{D} = \sqrt{\frac{\epsilon_0 k_B T_e}{n e^2}} \tag{3}$$

where T_e is the electron temperature, n the electron density, e the electron charge, k_B the Boltzmann constant and ϵ_0 the permittivity of free space. Quasi-neutrality implies that if ions are singly charged, than the density of electrons and ions are the same and may be referred to as plasma density. It is important to notice that λ_D increases with increasing electron temperature T_e and with decreasing plasma density n. For a plasma density in the order of 10^{20} m^{-3} and an electron temperature of 10-15 keV (1 eV $\sim$ 11600 K) the order of the Debye lenght is few μm.

1.2 Plasma confinement: the tokamaks and ITER

1.2.1 Energy balance and plasma confinement

The operating regime for a fusion reactor can be obtained by equating power input and output, so that energy equilibrium holds.

The first input term is represented by the α-particles power deposition inside the plasma, and this is, as described above, about 1/5 of the energy produced by the fusion reactions. The other input term is given by additional heating (neutral beams or RF waves).

The output terms are given by transport and radiation, mainly due to bremsstrahlung effect. The physics of transport phenomena is not fully understood yet, but from a practical point of view they can be described in terms of the so called energy confinement time τ_E, by writing

$$\tau_E = \frac{W}{P_L} \tag{4}$$

where W is the total energy stored in the fusion plasma and P_L is the total power lost due to transport phenomena.

The ignition point is described by the triple product $nT\tau_E$, where n is the plasma density and T its temperature [3]. In a simple case one may neglect additional heating (ignition regime) and radiation obtaining (with T and E_α both in eV) [1]:

$$n\tau_E = \frac{12T}{\langle\sigma v\rangle E_\alpha} \tag{5}$$

where σ is the cross section for the fusion reaction shown in Figure 2 and E_α is the energy of the produced α-particles, i.e. 3.5 MeV. The minimum of the $n\tau_{\mathrm{E}}$ product as a function of T, is around T= 25 keV, and for this temperature the triple product should satisfy

$$nT\tau_E > 5 \cdot 10^{21}\ \mathrm{keVm^{-3}s} \tag{6}$$

To increase the triple product to the required values, two techniques have been developed: inertial confinement and magnetic confinement. The first one is based on heating and compressing through the use of lasers a tiny sphere (few mm) made by a mixture of deuterium and tritium [1]. Its basic idea is to enhance the triple product by enhancing the density. The second one is based on a plasma confinement in toroidal geometry through the use of magnetic fields: it enhances the triple product enhancing the confinement time. The following section will focus on the magnetic confinement and will briefly present the two most used configurations: tokamak and stellarator.

1.2.2 Magnetic confinement

It is known that a magnetic field creates a spatial anisotropy: a charged particle can move unaffected in the direction parallel to the field, whereas any motion in the perpendicular plane is affected by the Lorentz force:

$$\vec{F} = q\vec{v} \times \vec{B} \tag{7}$$

where $\vec{v}$ is the particle velocity, q its charge and $\vec{B}$ the magnetic field. Therefore the trajectory of a charged particle is helicoidal, with a circular projection in the plane normal

to the field. This circle is described by the Larmor radius r_{L} (Eq. 8) and the typical frequency of the motion is the so-called cyclotron frequency ω_{c} (Eq. 9)

$$r_{\mathrm{L}} = \frac{mv_{\perp}}{qB} \tag{8}$$

$$\omega_c = \frac{qB}{m} \tag{9}$$

The best configurations for magnetic confinement, i.e the ones which minimise the losses of charged particles, are in toroidal form. The most used nowadays are tokamak (Figure 3, on the left) and stellarator (Figure 3, on the right). In both cases the toroidal magnetic field is created by external magnetic coils. The generated magnetic field has two important features:

- it is not constant (1/R dependence on the distance from the center of the torus)
- its field lines are bent

Both these features create gradients of the magnetic field which are responsible for radial drifts of the confined charged particles, which degrade the plasma confinement [1]. For this reason it is important to add a poloidal field component, that induces a centripetal force. In tokamaks this field is induced by a toroidal current, the so-called plasma current, which is achieved by a central solenoid magnet. Additionally, this current helps to heat the plasma by ohmic heating. The effective operation temperature range for a reactor is between 10 and 40 keV, and in order to reach and sustain such temperatures the use of additional heating is mandatory.

In a stellarator the magnetic field structure is completely determined by the form of the surrounding coils. The main advantage of not having to externally drive a plasma current is that the instabilities due to the current density gradients are much alleviated. On the other hand the complex structure of the coils needed to achieve the necessary shape for the magnetic surfaces imposes high demands on the design and construction of the device.

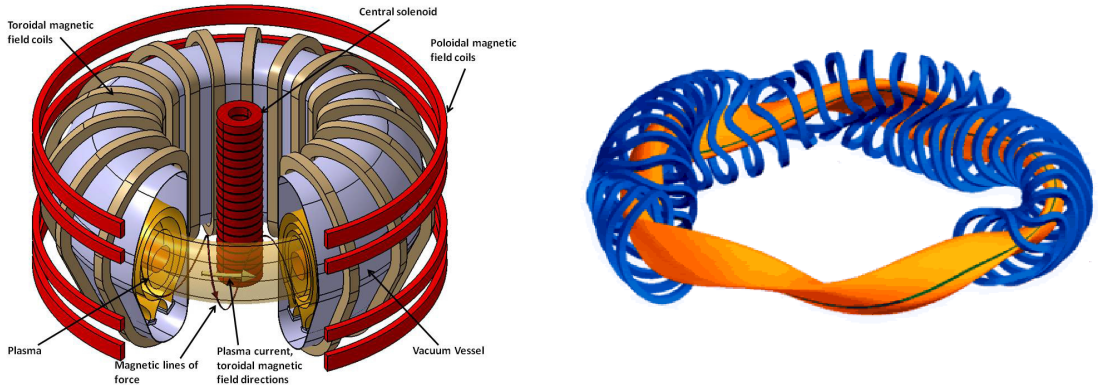

Figure 3: Left: Sketch of the tokamak configuration [1]; two groups of coils (toroidal and poloidal) and a central solenoid are clearly visible. Right: Sketch of the stellarator configuration [4]; current flowing in the twisted coils (in blue) generate both the toroidal and poloidal components of the magnetic field.

One important feature of the magnetic confinement, is that the energy confinement time increases with the reactor size [5]. Usually the major and minor radius of a tokamak

are in the order of some meters. See for example Table 1 in the next section where the main parameters of the tokamak ITER are listed.

1.2.3 ITER

The tokamak ITER, an overview of which is given in Figure 4, represents the most advanced project on nuclear fusion. Its facility is in Cadarache (France), and it is funded by EU, USA, Russia, Japan, India, China and South Korea. Its objective is to reach a Q=10 ratio between output and input power. ITER main parameters are listed in Table 1.

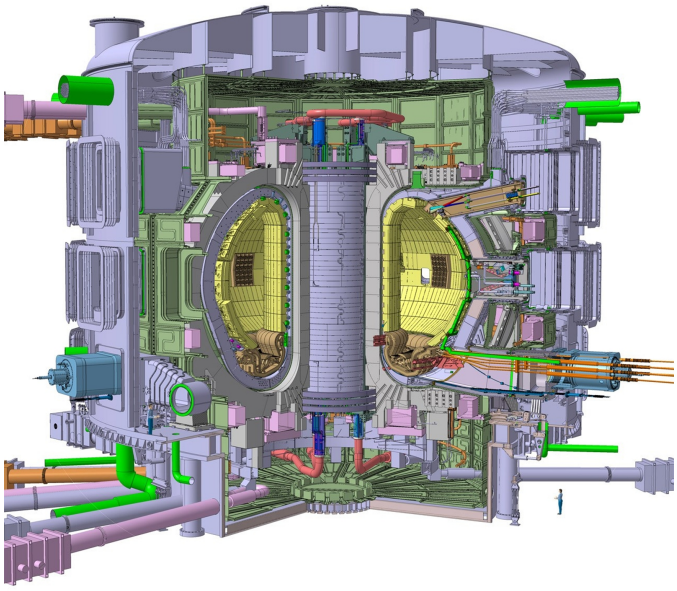

Figure 4: ITER cutaway view. An idea of the size of ITER is given by the human being on the right-hand side of the picture [6].

Before moving to D-T fusion, experimental campaigns will be performed in hydrogen and deuterium to test the various components of the machine. In order to heat the plasma to the necessary operation temperature ($\sim$15 keV), two different additional heating system will be used: RF waves and neutral beam injectors (NBI). The first one is based on generating RF waves and coupling them into the plasma. The used frequencies are close to the typical motion frequencies of the plasma particles, such as the ion or electron cyclotron frequency ($\sim$40-60 MHz and $\sim$170 GHz respectively) [6], in order to exploit resonances to achieve a better coupling and enhance the power deposition.

The second method, neutral beam injection, consists of producing deuterium (or hydrogen) ions, accelerating and neutralising them, so that the fast particles can penetrate the plasma despite of the magnetic field.

A very important feature of additional heating systems, especially needed for continuous operation, is their capability to drive a plasma current sustaining the poloidal field [1].

Parameter	Value
Fusion power	500 MW
Power gain factor Q	10
Pulse length	up to 3600 s
Plasma major radius	6.2 m
Plasma minor radius	2.0 m
Plasma current	15 MA
Toroidal field at 6.2 m radius	5.3 T

Table 1: ITER main parameters [6].

1.3 Main features of a neutral beam injector

For producing a beam of neutral hydrogen/deuterium particles it is necessary to create ions, accelerate them through a suitable potential difference and re-neutralise them. The use of deuterium ions requires a system for radiation protection since energetic neutrons are radiated by the reactions involving D in the beamline. For this reason in many experimental campaigns studying the NBI, hydrogen is used instead of deuterium.

Since the neutralisation efficiency (as discussed below) is minor than 100 %, in NBI systems it is necessary to deflect the remaining high energetic ions before they approach the magnetic field which confines the plasma in the torus. This is achieved by a magnetic field in all present facilities; in the case od ITER instead, an electric field will be used. The scheme of principle of a neutral beam injector satisfies all these needs. As shown in Figure 5, it consists of four main parts: an ion source, an accelerator, a neutraliser and a residual ion dump (RID). Topics of this thesis are the ion source and the accelerator, which will be described in more detail in chapter 2.

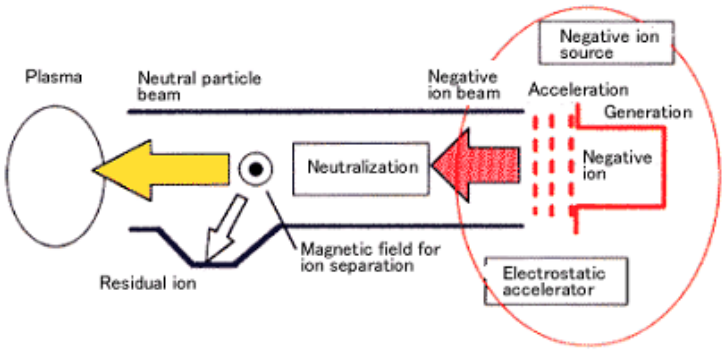

Figure 5: Scheme of a neutral beam injector dedicated to the Japanese tokamak JT-60U [7]. Negative ions are generated in the ion source (on the right), accelerated by an electrostatic accelerator and then neutralised. The remaining charged particles are deflected and dumped onto a magnetic residual ion dump, so that the beam particles approaching the plasma (on the left) are neutral.

The plasma is heated by the reactions between beam and plasma particles, which are charge exchange (Eq. 10) and ionizations due to collisions with ions (Eq. 11) or electrons (Eq. 12).

$$\mathrm{H_{beam}} + \mathrm{H^+_{plasma}} \rightarrow \mathrm{H^+_{beam}} + \mathrm{H_{plasma}} \tag{10}$$

$$\mathrm{H_{beam}} + \mathrm{H^+_{plasma}} \rightarrow \mathrm{H^+_{beam}} + \mathrm{H^+_{plasma}} + \mathrm{e^-} \tag{11}$$

$$\mathrm{H_{beam}} + \mathrm{e^-} \rightarrow \mathrm{H^+_{beam}} + 2\mathrm{e^-} \tag{12}$$

The beam intensity I is a function of the penetration depth x and of the initial beam intensity I_0 as

$$I = I_0 e^{-x/\lambda} \tag{13}$$

with λ given by

$$\lambda = n\left(\sigma_{\mathrm{cx}} + \sigma_{\mathrm{i}} + \frac{\langle \sigma_{\mathrm{e}} v_{\mathrm{e}} \rangle}{v_{\mathrm{beam}}}\right) \tag{14}$$

where σ_{cx} and $\sigma_{\mathrm{i,e}}$ are the cross-section for charge exchange and for the two ionizations respectively, $\langle \sigma_{\mathrm{e}} v_{\mathrm{e}} \rangle$ is the reaction rate of the collisions with electrons and n is the plasma density.

In such a way it is possible to determine an energy range allowing the beam to enter the plasma and deposit power in its centre, where the confinement is the highest. For a tokamak with the size of ITER and a plasma density of 10^{20} $\mathrm{m^{-3}}$, an injector in the 100 keV range would lead a beam to being absorbed in the external region of the torus. For this reason the beam energies has to be at least in the order of hundreds of keV.

For ITER injectors the required power is 33 MW (16.5 MW $\times$ 2 injectors) and the energy has been raised to 1 MeV mainly for two reasons [8, 9]. First there is a limit to the maximum current density that may be extracted from the ion source (see section 2.2) and second the efficiency for driving a plasma current in the torus is higher for higher beam particle energy.

For such a high beam energy the use of negative ions is mandatory. The neutralisation efficiency of positive ions in fact, drops with increasing energy, while for negative ions it remains at acceptable values, around 60 %, as it can be seen in Figure 6.

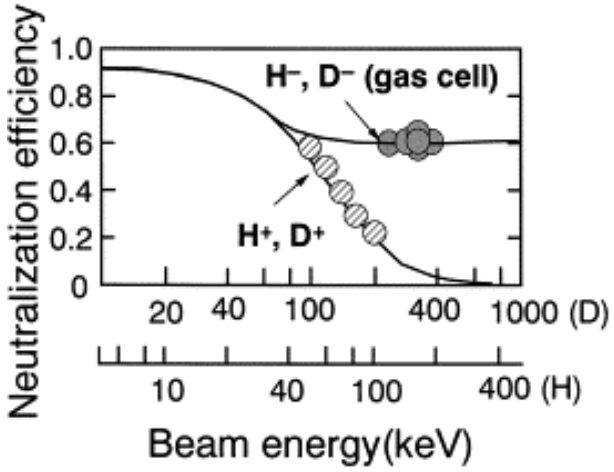

Figure 6: Neutralisation efficiency for hydrogen ions as a function of energy. The circles refer to measurements performed at the NBI system of the tokamak JT-60U [10].

The main reason why it is easier to neutralise negative ions lies in the low binding energy of the additional electron, which is 0.75 eV. On the other hand because of this low binding energy it is more difficult for them to survive in the plasma of the ion source.

There are many critical aspects which affect the beam and have to be taken into account. First of all, since within the extraction system some negative ions are neutralised by reactions with the background gas (Eq. 15), the current that has to be extracted from the ion source is larger than the necessary accelerated current. In general the neutralization which occurs in the extraction system is referred to as *stripping*. Calculations performed for ITER estimate a stripping fraction of about 30 % [11].

Downstream the acceleration system is the so-called drift region. In this region the most important reactions are neutralization (Eq. 15) of H^- in H_0 and the ionization of the background gas due to the collisions with fast H_0 (Eq. 16).

$$H^- + H_2 \rightarrow H^0 + e + H_2 \tag{15}$$

$$H^0 + H_2 \rightarrow H^0 + e + H_2^+ \tag{16}$$

The creation of positive ions in the drift region is also a very important aspect for the beam optics. Since in this region the electric field is negligible, these secondary particles can create a plasma, shielding the potential self-induced by the beam. This phenomenon is known as *space charge compensation (SCC)* and is fundamental for the beam optics, allowing a beam of charged particles not to further diverge because of Coulomb repulsion [12].

The beam of ITER NBI will be formed by many sub-beams, usually called *beamlets* (see section 2.2). The beamlet *divergence* is a measure of the beamlet widening and is therefore related to the width of the particle velocity distribution in the beamlet, that is given by a bell-shaped function (often a Gaussian is assumed). Throughout this thesis, the half 1/e width of this distribution will be used when referring to divergence.

Another important feature of the beam is its *homogeneity*. Inhomogeneity is defined as the maximum difference between the current from a beamlet and the average current of all beamlets. Divergence and inhomogeneity for ITER NBI system should be respectively below 7 mrad and below 10 % [13].

Together with negative ions also electrons from the source plasma are co-extracted. This represents one of the main issues to deal with in negative ion sources: electrons have to be dumped because they cannot pass the magnetic field at the edge of the torus and thus they could not enter the plasma of ITER. Since they could deposit a very high power density load on the surface they hit, they are filtered before they are accelerated at full energy. Nevertheless, the amount of co-extracted electrons has to be kept as low as possible: the ITER requirement is to have a ratio between *co-extracted electrons* and ions below 1. Electron dumping will be explained in section 2.2.

ITER main requirements for one injector are summarised in Table 2.

Up to now the ITER requirements for a NBI have been fulfilled only separately at different test facilities. In particular the foreseen current density and pulse length have been achieved at IPP [14, 15] while the foreseen particle energy has been achieved at JAEA [16]. For this reason a dedicated test facility has been commissioned to the EU and is being realised at the Consorzio RFX in Padova, Italy [17, 18]. Both the full size ion source and injector will be developed in the two testbeds SPIDER (**S**ource for the **P**roduction of **I**ons of **D**euterium **E**xtracted from an **R**F plasma) [19] and MITICA (**M**egavolt **ITER**

Injector and **C**oncept **A**dvancement) [20], respectively. An intermediate step between the currently used small sources (extraction area of few hundreds of cm^2) and the testbed SPIDER is the IPP test facility ELISE, described in section 3, whose ion source has an extraction area of about 1000 cm^2, which is half of the ITER requirement.

Parameter	**Hydrogen**	**Deuterium**
Power delivered to ITER	16.5 MW	16.5 MW
Extraction Area	0.2 m^2	0.2 m^2
Extracted current density	$\geq$340 A/m^2	$\geq$290 A/m^2
Accelerated current	$\geq$ 49 A	$\geq$ 40 A
Accelerated ion energy	0.87 MeV	1 MeV
Ratio of co-extractred electrons to ions	$<$ 1	$<$ 1
Source Pressure	0.3 Pa	0.3 Pa
Beam divergence	$\leq$ 7 mrad	$\leq$ 7 mrad
Beam inhomogeneity	$<$ 10 %	$<$ 10 %

Table 2: Main parameters of one ITER NBI.

2 Neutral beam injection

As anticipated in section 1.3, a neutral beam injector consists of four main parts. In this thesis the focus is laid on the ion source and on the acceleration, while neutralisation and residual ion dumping will not be treated. Processes for negative ion production (and destruction), the role of caesium, the multi-grid system used for acceleration are the main topics that will be discussed in this chapter.

2.1 Ion source

For NBI two types of ion sources are commonly used: arc sources and RF sources. In the former electrons are produced by driving a current in tungsten filaments, heating them up to 2000-3000K. The thermionic produced electrons are then accelerated up to 100 eV to ionise a gas creating a plasma in which negative ions are produced. Filaments are consumed because of the sputtering caused by the impinging ions and they have to be changed regularly. The duration estimate in the case of ITER is about six months [21].

In the RF sources an oscillating electromagnetic field is induced in the gas by means of RF coils, and again electron acceleration leads to gas ionisation forming a plasma. The great advantage of RF sources with respect to arc sources is that they are almost maintenance free. This is one of the reasons why they have been chosen for the ITER NBI system [22].

RF sources have been developed at IPP in Garching in the last decades, where most of ITER NBI ion source requirements have been fulfilled separately at different test facilities using the IPP prototype RF source.

Already in 2005 at BATMAN (**BA**varian **T**est **MA**chine for **N**egative ions) the requirements regarding the extracted current densities, the source pressure and the electron to ion ratio were fulfilled or excedeed with a small extraction area ($<$0.01 m^2) and pulse length below 6 s. A pulse length up to 3600 s has been achieved at MANITU (**M**ulti **A**perture **N**egative **I**on **T**est **U**nit), with an extraction area of 0.03 m^2 [23]. An overview of IPP prototype RF source is given in Figure 7.

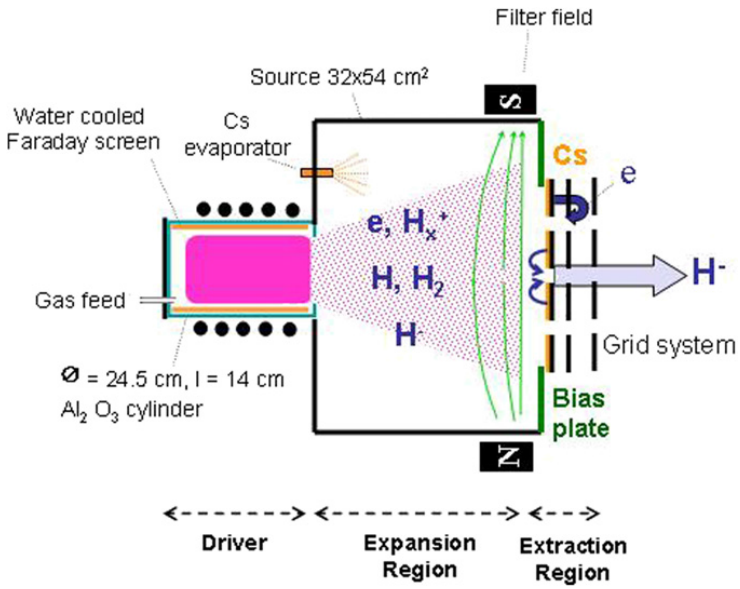

Figure 7: Schematic view of IPP prototype RF source [24].

The prototype negative ion source consists of three parts: driver, expansion region and extraction region. The driver, whose design is shown in Figure 8, is the cylindrical region where the RF is coupled to the plasma. It is formed by a RF coil connected to an oscillator. The coil is wrapped around an Al_2O_3 cylinder, the back side of which is covered with the so-called driver back plate. The coil is water cooled and the alumina cylinder is shielded from the plasma by a Faraday screen [23]. The typical RF frequency is about 1 MHz and the RF power is tens of kW. Inside the driver, electron temperature and density are in the order of $T_e \sim 10$ eV and $n_e \sim 10^{18}$ m^{-3} respectively [24].

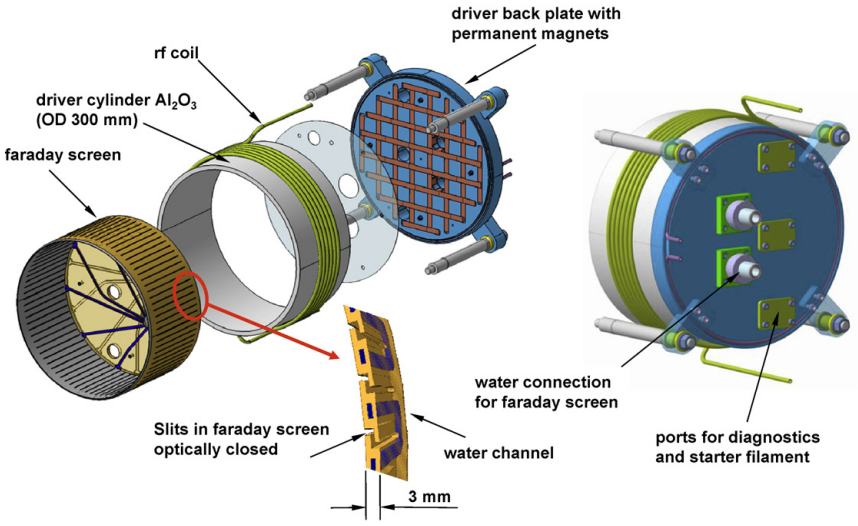

Figure 8: Design of the drivers for the ion source of the IPP test facility ELISE [25].

In the expansion region the plasma expands and, as a result of this expansion process, a first cooling occurs.

The extraction region is represented by a system of two grids, the so-called plasma grid (PG), facing the plasma of the ion source, and the extraction grid, which is kept at a more positive potential (5-10 kV). Negative ions are extracted through the plasma grid and accelerated by means of this potential difference U_{ex}.

A third grid kept at ground potential, the so-called grounded grid, completes the acceleration system that will be discussed further in section 2.2. The three grids contain a large number of apertures and are water cooled to remove the heat load due to the impinging particles.

The ion production in the ion source is achieved through both volume and surface processes [26, 27]. The volume process is the dissociative attachment obtained after the excitation of high vibrational levels in the electronic ground state of the H_2 molecule.

$$H_2 + e \rightarrow H_2^*(v) + e \tag{17}$$

$$H_2^*(v) + e \rightarrow H + H^- \tag{18}$$

The surface production processes are based on the conversion of hydrogen particles impinging on the source walls. They can be divided in two branches: atomic and ionic, depending whether the hydrogen particles approaching the wall are neutral or positive ions (H^+, $H_2{}^+$, $H_3{}^+$).

$$H, H^+ + e \rightarrow H^- \tag{19}$$

A high efficiency for this H^- production process is correlated to a low work function, which is in general achieved through the evaporation of a caesium into the source and the subsequent formation of Cs layers on the wall surfaces [28, 29].

For introducing the caesium in the source, a caesium oven is installed on its backplate. Then Cs is distributed during vacuum phases and plasma pulses. In order to avoid accumulation of a too large amount of caesium on the source walls, its surfaces are generally kept around 35-40 °C, a temperature slightly higher than the caesium melting point, which is 28 °C.

To optimise the negative ion production, also the plasma grid is kept at a suitable high temperature (about 100-150 °C) [30]. The background physical reason why keeping the PG temperature in this range is beneficial for the source performances is however not fully understood yet.

Handling the caesium distribution in the source volume is not easy and this is the main limit of the surface processes. Volume processes are much easier to handle but at the operation pressure of 0.3 Pa (required for ITER NBI) the ion production achieved through them is not enough to fulfill ITER requirements at a sufficiently low ratio of co-extracted electrons to extracted H^- [23]. For this reason exploiting the surface processes is mandatory.

Since the additional electron of H^- ions is weakly bound (its binding energy is 0.75 eV) negative ions have a low survival length in the source (few centimeters), therefore most of the extracted H^- are those created close to the extraction area. The most important re-neutralization processes that may occur are detachment (Eq.20 - 22) and mutual neutralization (Eq. 23 - 25) .

$$H^- + e \rightarrow H + 2e \tag{20}$$

$$H^- + H \rightarrow H_2 + e \tag{21}$$

$$H^- + H_2 \rightarrow H + H_2 + e \tag{22}$$

$$H^- + H^+ \rightarrow 2H \tag{23}$$

$$H^- + H_2^+ \rightarrow H_2 + H \tag{24}$$

$$H^- + H_3^+ \rightarrow 2H_2 \tag{25}$$

In order to reduce the amount of co-extracted electrons, and additionally reduce the H^- re-neutralisation in the plasma of the ion source, the electron density and temperature in the plasma close to the PG have to be reduced. For this reason a magnetic field is created in front of the plasma grid.

This filter field, yielded by permanent magnets or by a current I_{PG} flowing through the plasma grid, magnetise the electrons, which can transverse this region mainly by Coulomb collisions, whose cross section decreases for increasing speed, since $\sigma(v) \sim v^{-4}$ close to the PG [31]. So the filter field helps reducing the electron density and temperature T_e, which

is generally between 1 and 2 eV. The typical order of magnitude of the magnetic filter field is few mT.

As shown in Figure 9 for the IPP test facility ELISE, also the ion current is decreased by increasing the magnetic field (in this case achieved by a current flowing through the plasma grid), but since the ions have a larger mass, they are less affected by the filter field, and the ratio j_e/j_H between the electron and ion extracted current densities largely decreases. Furthermore, the filter field is responsible for a deflection of the negative ion beam in the vertical direction. At ELISE, for example, the deflection of the beam is in the order of 5-10 cm at a distance of 3.5 m for a PG current around 2 kA, in hydrogen. For the ITER NBI, the deflection of the beam due to the magnetic filter field will be compensated for by a suitable arrangement of the permanent magnets in the extraction grid [32].

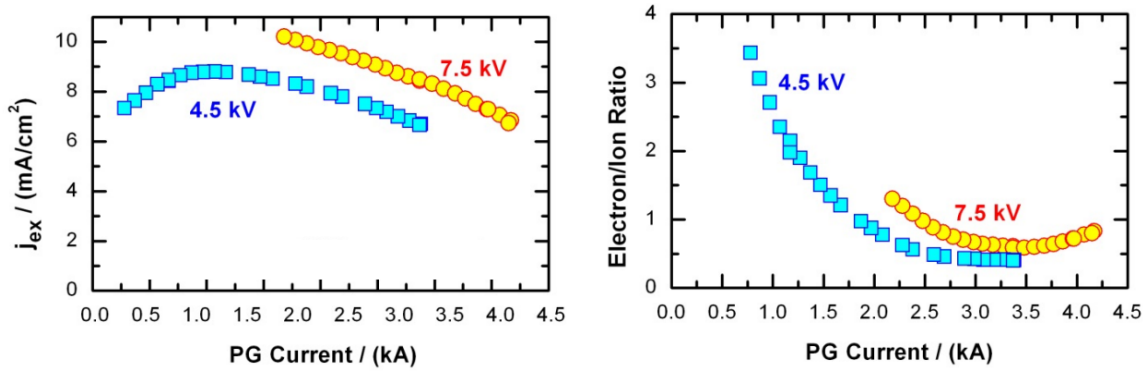

Figure 9: Effect of the PG current (i.e. of the filter field) on the source performance at ELISE for different extraction voltages. Left: negative ion extracted current density. Right: Electron to ion ratio. Operation in hydrogen, source filling pressure of 0.5 Pa [33].

Another technique that helps reducing the amount of co-extracted electrons is biasing the plasma grid positively with respect to the source (few tens of V). The bias power supply is usually operated in a current controlled mode. Increasing the bias current I_{bias} (and thus additionally the bias voltage), the potential distribution in the plasma region close to the PG changes, leading to a reduction of the electron to ion ratio, as shown in Figure 10.

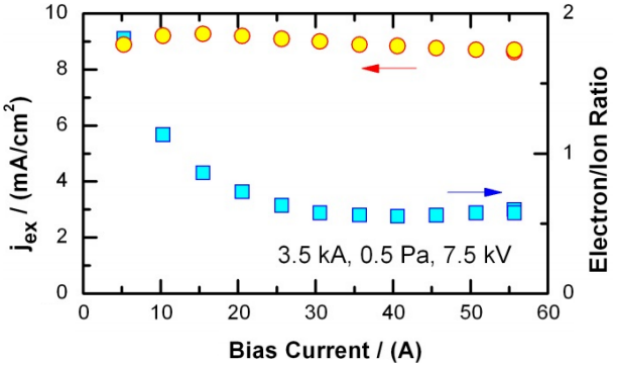

Figure 10: Effect of the bias current on the ion source performance at the test facility ELISE: extracted current density (in yellow) and electron to ion ratio (in blue). Operation in hydrogen, $U_{ex} = 7.5$ kV, $I_{PG} = 3.5$ kA, source filling pressure of 0.5 Pa [33].

2.2 Extraction and acceleration

As mentioned in section 2.1, the extraction and acceleration system at the IPP test facilities consists of three grids: the plasma grid (PG), facing the plasma of the ion source and kept at negative potentials, the extraction grid (EG), at a more positive potential, and the grounded grid (GG), as shown in Figure 11. Therefore the total supplied voltage U_{HV} is divided in two steps: extraction potential U_{ex} and acceleration potential U_{acc}.

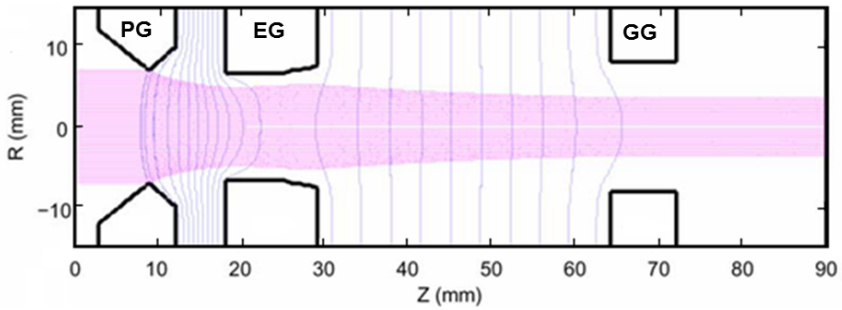

Figure 11: Example of beam optics simulation for the test facility SPIDER [34]. The equipotential lines are drawn in blue and the particle trajectories in magenta. Potential were set to $U_{\mathrm{ex}} = 9.8$ kV and $U_{\mathrm{HV}} = 100$ kV.

The reason for this two-step acceleration lies in the necessity to dump the co-extracted electrons before they are fully accelerated. This filtering of the electrons is achieved by a magnetic field, which is created by permanent magnets installed in the extraction grid as shown in Figure 12. The field lines of this deflection field and those of the filter field lie in perpendicular planes (see again Figure 12). Since the magnetic deflection is related to the Larmor radius, which is proportional to the square root of the particles mass, the negative ions are much less affected.

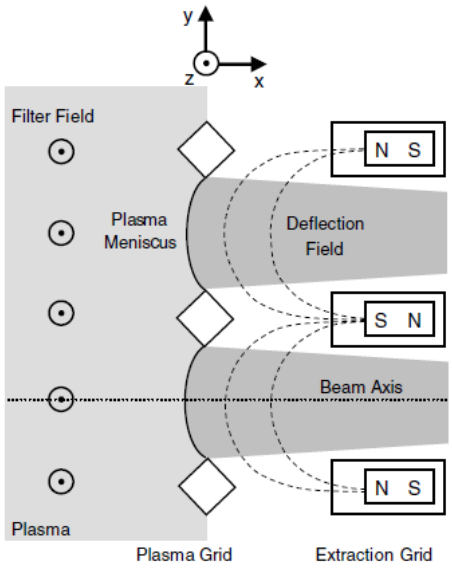

Figure 12: Schematic of the magnets disposition in the extraction grid [35]. The lines of deflection field created by these magnets are perpendicular to those of the filter field.

The power deposited on the extraction grid by the co-extracted electrons is removed by a cooling system and the limit of this power represents the limit to the co-extracted

electron current. This current is directly correlated to the maximum amount of extracted negative ions, since when increasing the ion current, by increasing the extraction voltage U_{ex}, also the electron current increases. This leads to a strong increase in the power load on the EG that is given by the product between the electron current and the extraction voltage.

The potential surface U = 0 V (with respect to the ion source) has the shape of a meniscus, determined by the extraction voltage, the size of the apertures, and plasma parameters [36].

Because of the space charge of each beamlet, there is a limit in the maximum current that may be extracted. Representing the beamlet as a plane diode of length d, under a potential difference U, this limit is expressed by the Child-Langmuir law [36]:

$$j_{ex} = \frac{4\epsilon_0}{9}\sqrt{\frac{2Ze}{m}}\frac{U^{3/2}}{d^2} \tag{26}$$

where Z is the atomic number of the extracted particles.

An important parameter for characterising the beam optics is the so-called *perveance*, which in this thesis will be indicated by Π. Perveance is defined by

$$\Pi = \frac{I}{U^{3/2}} \tag{27}$$

where I is the extracted current and U the extraction voltage. From the Child-Langmuir law it is possible to determine its maximum

$$\Pi_0 = \frac{4\pi\epsilon_0}{9}\sqrt{\frac{2Ze}{m}}\frac{R^2}{d^2} \tag{28}$$

which depends only on the geometry of the extraction aperture (R is the aperture radius) and the type of charged particles the current is made of (atomic number Z and mass m). The value Π_0 increases with the square root of the atomic number Z and decreases with the square root of the mass. This means for example that Π_0 is different for hydrogen and deuterium.

The meaning of perveance may be better understood by thinking of the three-grids as a system of two lenses. Starting from the ratio between U_{ex} and U_{acc} that produces the best beam optics, any change in the extraction voltage corresponds to a shift of the focal point of the first lense along the beamlet axis. Both a forward or a backward shift with respect to the optimum turn into a widening of the beam itself, which means a larger divergence. In general the normalized perveance Π/Π_0 is used instead of perveance, since it allows to compare accelerators with different geometries. As it may be seen in Figure 13, starting from the lowest normalised perveance (about 0.04 in the Figure), for increasing perveance the beam divergence decreases and reaches a minimum. This point is called the perveance optimum. For higher perveances, the beam divergence increases again. The region in which divergence decreases for increasing divergence (below the optimum) is usually called under-perveant region while the region in which divergence increases for increasing perveance is called over-perveant region .

The perveance optimum may also be very broad. For example at ELISE, the test facility concerned in this thesis (see section 3.1), the optimum of the (normalised) perveance in hydrogen lies between 0.15 and 0.25.

It must be considered however, that the beamlet divergence depends also on the ratio between the extraction voltage and the acceleration voltage and on the onset position of the space charge compensation, which depends on the pressure in the drift region (downstream the grounded grid). Higher pressure means an earlier onset of the SCC i.e. a lower beamlet divergence, whereas lower pressure means a later onset of the SCC i.e. a larger beamlet divergence (see the solid lines in Figure 13). On the other hand, the higher the pressure in the drift region, the higher the pressure in between the grids. This means that the stripping is higher and the accelerated current lower.

The pressure in the drift region should be a compromise between the two necessity of low stripping and good space charge compensation. At ELISE for example, the pressure in the drift region during the pulses is in the range of 10^{-4} mbar.

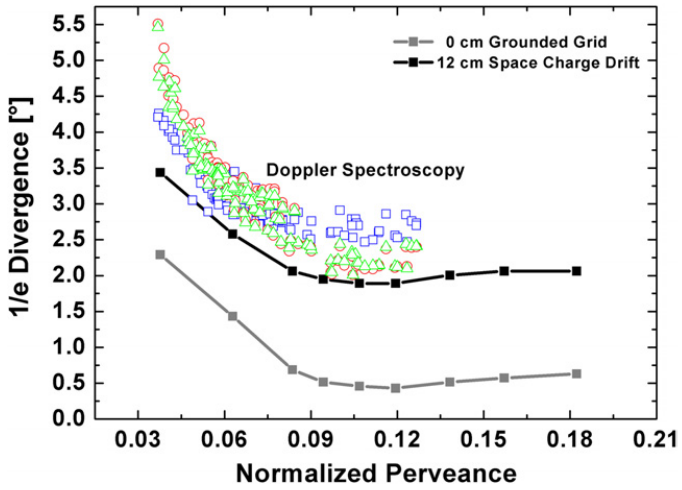

Figure 13: Divergence versus normalized beam perveance at test facility MANITU [37]. Points represent measurements, lines are given by simulations assuming the space charge compensation to be achieved at different distances from the grounded grid.

3 The ELISE test facility

As mentioned in section 2.1, the ITER target with respect to the current density was already achieved at IPP test facility BATMAN with an extraction area of about 70 cm^2. The test facility ELISE (see Figure 14), whose extraction area is half of that required for an ITER NBI, has been designed as an intermediate step between these small sources and the full size ITER source, whose extraction area will be about 2000 cm^2. The main features of the test facility are described in section 3.1, while section 3.2 focuses on the beam diagnostics which are used at ELISE.

3.1 ELISE purpose and design

The aim of the ELISE design is to be as close as possible to the ITER ion source, but some modifications have been implemented allowing a better diagnostic access. The ion source of ELISE, an overview of which is given in Figure 16, has the same width and half the height (1.0 m $\times$ 0.9 m) as those required for ITER ion source. Another important difference with respect to the design of an ITER NBI, is the total applied voltage, which is up to 60 kV at ELISE, much lower than 1 MV. In addition, the maximum design voltage has not been achieved up to now ($U_{\mathrm{HV}} < 45$ kV has been used), therefore the beamlet divergence at ELISE is generally larger than what is required for an ITER NBI. Throughout this thesis, the typical range in hydrogen is 2°-3°, and divergences below 1° are very seldom achieved. The main parameters of ELISE are summarised in Table 3, at the end of this section.

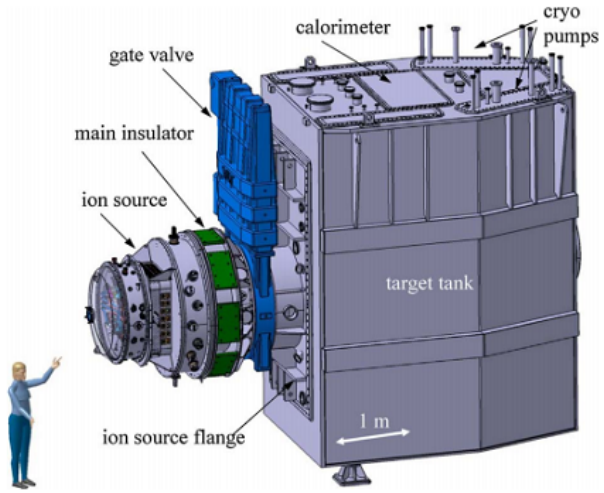

Figure 14: Overview of ELISE test facility [38].

Accelerating a current of 20 A (half of the ITER requirements in deuterium) with a 60 kV potential difference, a negative ion beam with a power up to 1.2 MW can be achieved at ELISE. To stop the beam a copper calorimeter (1.2 m $\times$ 1.2 m $\times$ 0.04 m) is placed on the beam axis at a distance of 3.5 m from the grounded grid (see section 3.2.1).

In principle ELISE can be operated for 1h, confirming all the results obtained by the smaller facilities regarding other parameters of interest such as current density, electron/ion ratio, etc, but due to the limitations of the IPP HV system only pulsed extraction is possible (10 s beam pulse every 180 s). Since the long pulse test facility MANITU has

indicated that this kind of operation should have no influence on the source performance, this was not to be considered as a real limit [39].

A scheme of the trigger timing for 20 s RF pulses operation is shown in Figure 15. The delay between the beginning of the HV phase and of the RF pulse is necessary to stabilise the plasma before extraction. The RF is terminated about three seconds after the HV phase to facilitate spectroscopic measurement inside the source.

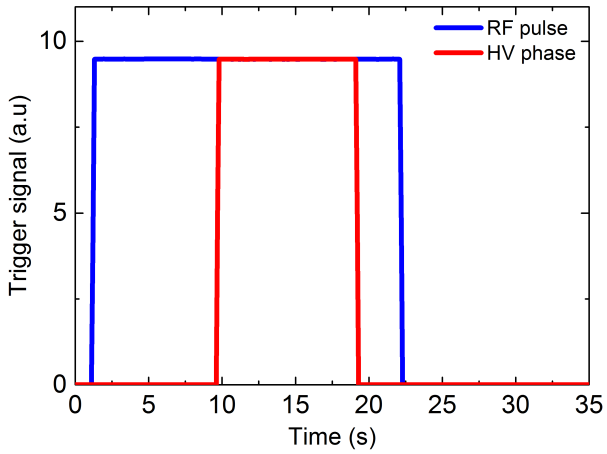

Figure 15: Scheme of the trigger signals at ELISE. The blue signal is the RF pulse, the red is the HV phase.

ELISE operates both in hydrogen and deuterium, so a concrete housing surrounds the test facility for radiation protection during D^- operation.

The ion source, shown in Figure 16, is a vessel with thin (between 6 and 15 mm) stainless steel walls inside which cooling channels run [25].

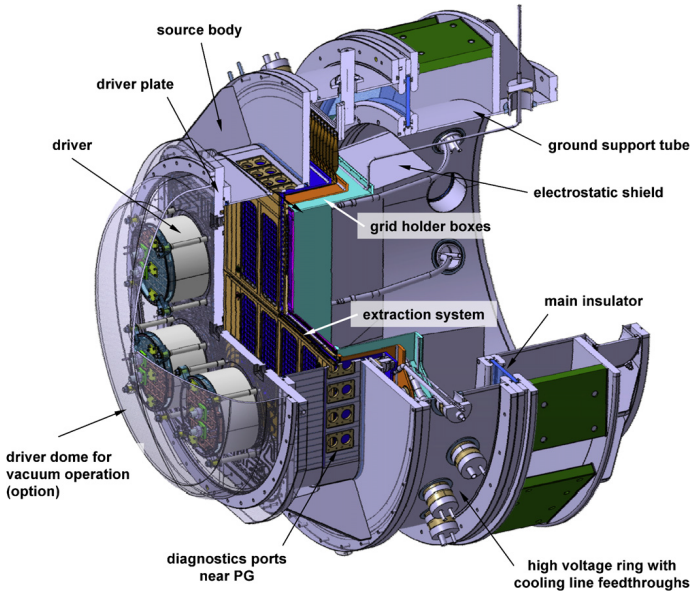

Figure 16: ELISE source with the extraction system and the HV insulation [38].

Caesium is evaporated in the source by two Cs ovens and, in order to improve caesium conditioning, the wall temperatures are kept at about 40°C. The back side of the source

vessel is closed by the driver plate, which is cooled due to the power load (few tens of kW) resulting from the backstreaming positive ions which are produced in the drift region. The source inner surfaces are coated with a 1 mm copper layer to have an uniform temperature distribution and 10 μm thick nickel layer on top to prevent copper sputtering [40] and the reactions between copper and caesium.

The four RF drivers, consisting of Al_2O_3 cylinders protected by cooled Faraday shields, are positioned in the back plate. The RF coils are twisted around the driver cylinders, as shown in Figure 8 (see section 2.1). Two horizontal coils are connected in series to one RF generator delivering a power up to 180 kW. Therefore the maximum RF power of the ELISE ion source is 2 $\times$ 180 kW.

The extraction and acceleration system is composed of three grids, as discussed in section 2.2: plasma grid (PG), extraction grid (EG) and grounded grid (GG). Every grid is formed by two identical segments [41]. In each grid segment there are 4 groups of Ø14 mm apertures (5 $\times$ 16 apertures, spacing 20 mm $\times$ 20 mm), as can be seen in Figure 17, so the ELISE beam is formed by 640 beamlets divided in 8 beamlet groups.

In order to enhance the H^- production on the PG surface, it is cesiated and operated at temperatures up to 150 °C. In addition, a current up to 8 kA can be driven vertically through the PG, shown in Figure 17, to generate the magnetic filter field.

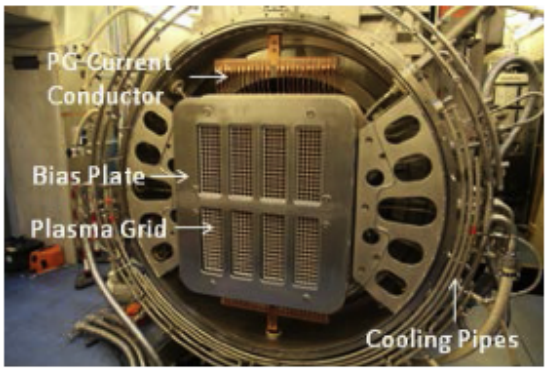

Figure 17: Plasma grid and bias plate of ELISE. A current up to 8 kA may be driven vertically through the PG [42].

As discussed in section 2.1, this field is necessary to cool down electrons and reduce their density, but it is also responsible for a deflection of the beam itself in vertical direction. This deflection could be upward or downward depending on the direction of the field. Throughout this thesis the vertical shift of the beam due to the PG current is downward. Moreover, the plasma grid is biased positively (20-30 V) with respect to the source. As mentioned in 2.2, this bias helps reducing the amount of co-extracted electrons. Finally, the so-called *bias plate* is installed in front of the PG (Figure 17) and electrically connected to the source walls. The plate extends the source potential near the PG apertures, reducing the biased area. This helps increasing the effect of the bias itself on the amount of co-extracted electrons [30].

The source of ELISE is kept at high potential (up to -60 kV) while the tank and the calorimeter are at ground potential. HV insulation is achieved via a vacuum tight main insulator with an inner diameter of 1.3 m. A scheme of the ELISE HV circuit is shown in Figure 18.

The currents flowing back from the different components to the power supply are

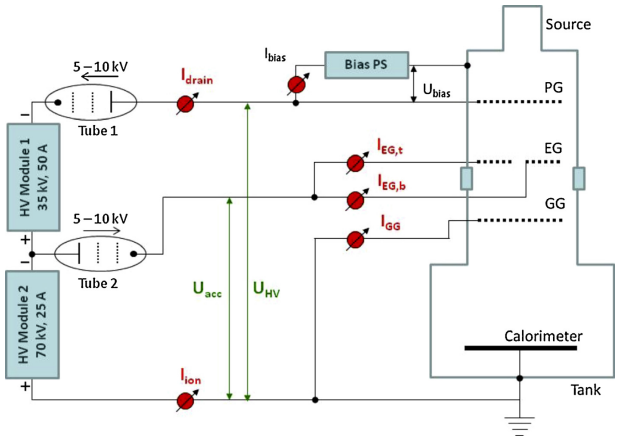

Figure 18: Scheme of ELISE HV circuit with voltage and current measurement [42]. I_{drain} is the current flowing from the power supply to the source; $I_{\mathrm{EG,t}}$ and $I_{\mathrm{EG,b}}$ are the current on the upper and lower side of the extraction grid, respectively; I_{GG} is the current on the the grounded grid. I_{ion} is the current flowing back from the ground potential to the power supply. A dedicated power supply is used for the current I_{bias}, providing the bias of the PG.

measured individually.

At the perveance optimum it is reasonable to assume that the current on the extraction grid ($I_{\mathrm{EG,t}} + I_{\mathrm{EG,b}}$) is only due to the deflected electrons while the current on the calorimeter and on the grounded grid, whose sum is the current flowing back from ground potential to the power supply, are due mostly to negative ions [43]. This means that the electron to ion ratio $j_{\mathrm{e}}/j_{\mathrm{H}}$ can be derived from the ratio between the total current impinging on the extraction grid I_{EG} and the ion current I_{ion}.

The base pressure in the tank of ELISE is around 10^{-6} mbar and it is provided by two turbomolecular pumps, for a total pumping speed of 2×2200l/s (for nitrogen). In addition also a roots blower pump with a pumping speed of 300 l/s is used and a cryopump system with a speed of 2 × 350000 l/s is installed in the chamber. The cryopumps reduce the pressure in the source to 10^{-7} mbar (10^{-4} mbar during a pulse).

As mentioned above, the ELISE test facility has been equipped with a large number of diagnostic accesses for both the ion source plasma and the beam. In this thesis only the beam diagnostics will be considered, a description of which is given in the following section.

Parameter	**Value**
Isotopes	Hydrogen, Deuterium
Source size	1.0 m × 0.9 m
Extraction area	0.1 m^2
Number of apertures	640
Total voltage	$\leq$ 60 kV
Extraction voltage	$\leq$ 12 kV
Pulse length	3600 s plasma, 10 s beam extraction every 180 s

Table 3: ELISE main parameters.

3.2 The ELISE beam diagnostics

Used as beam diagnostics at ELISE are a diagnostic calorimeter, a tungsten-wire calorimeter and beam emission spectroscopy (BES). The setup of these diagnostics is shown in Figure 19 and will be discussed in the next sections.

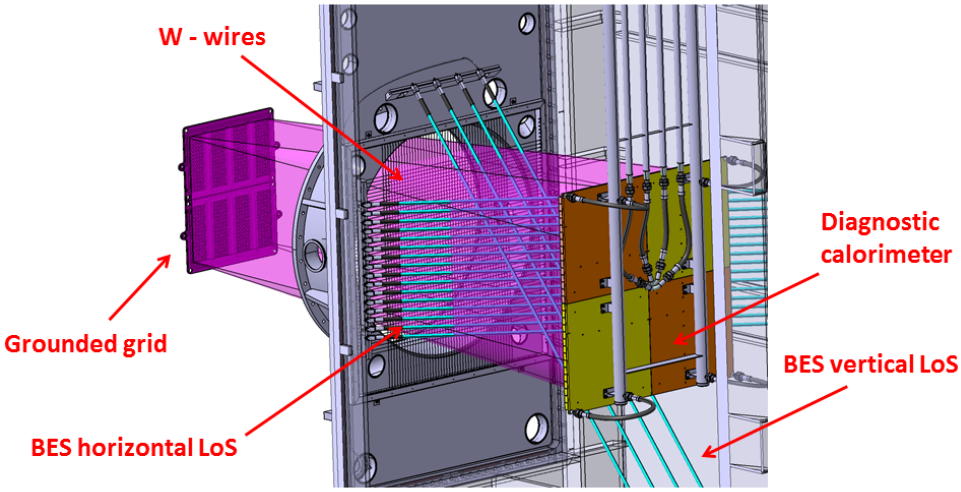

Figure 19: CAD drawing of ELISE beam diagnostics. Courtesy of R. Nocentini (IPP). The grounded grid is on the left side of the Figure, while the diagnostic calorimeter is on the right. In the middle the tungsten wires may be seen. The 16 horizontal and 4 vertical lines of sight (LoS) for beam emission spectroscopy are represented by the light blue lines.

3.2.1 Diagnostic calorimeter

The diagnostic calorimeter, shown in Figure 20, is placed at a distance of 3.5 m downstream the GG and its functions are to stop the beam and to provide diagnostics of the beam itself. For this latter purpose the calorimeter is observed via an infrared (IR) camera and is equipped with thermocouples (TCs), whose positions in the calorimeter are given by the red dots on the right side of Figure 21. From the power deposition on the calorimeter surface it is possible to determine, a 2D profile of the accelerated current density, from which beam divergence and signals of the uniformity may be derived. Deriving divergence and uniformity evaluation from the IR images of diagnostic calorimeter is the main task of this thesis.

The calorimeter is made out of copper and is formed by 30 $\times$ 30 blocks. Each block has a depth of 25 mm, a 38 mm $\times$ 38 mm surface and their spacing is 2 mm, so the total width and height of the calorimeter are 1.2 m each. The blocks are connected on the backside on four panels. When referring to these panels in the following, they will be numbered from left to right and from top to bottom, as shown in Figure 20.

In order to reduce their reflectivity, the surface of the copper blocks facing the beam has been covered, with a Molybdenum Disulfide coating (D-321R), selected among other coatings, after tests on a simple beam dump calorimeter [45]. The determination of the emissivity of this blackening layer, which is fundamental to calibrate the IR measurements, is described in section 4.3.

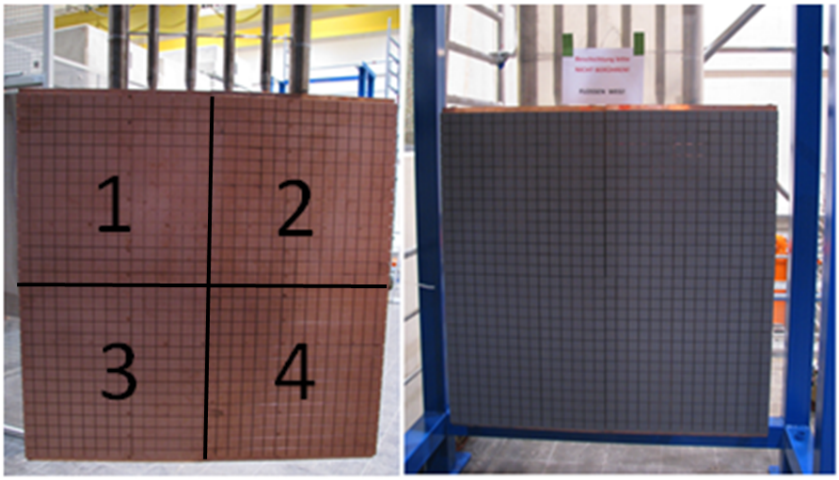

Figure 20: Diagnostic calorimeter before and after coating. Black lines represents the separations between the panels. The panel numbering introduced in this picture will be used in the following sections.

The maximum power load on the calorimeter is 1.2 MW (20 A $\times$ 60 kV). For a beam with 2° divergence, this means a maximum power density of 3 MW/m^2. From simulations it was found that for a similar power, the temperature at the end of the beam-on phase is about 300-350°C. This is very important since a temperature below 450°C is necessary for not damaging the brazing of the various calorimeter components [44].

In a coordinate system in which x is the horizontal axis, y the vertical one and the origin is given by the centre of the diagnostic calorimeter, the projections of the eight beamlet group centers on the calorimeter surface for a non deflected beam are at y = $\pm$ 20 cm and x = -24, -8 ,8, 24 cm, as it is shown in Figure 21 (left). When referring to the beamlet groups in the following they will be numbered as in Figure 21.

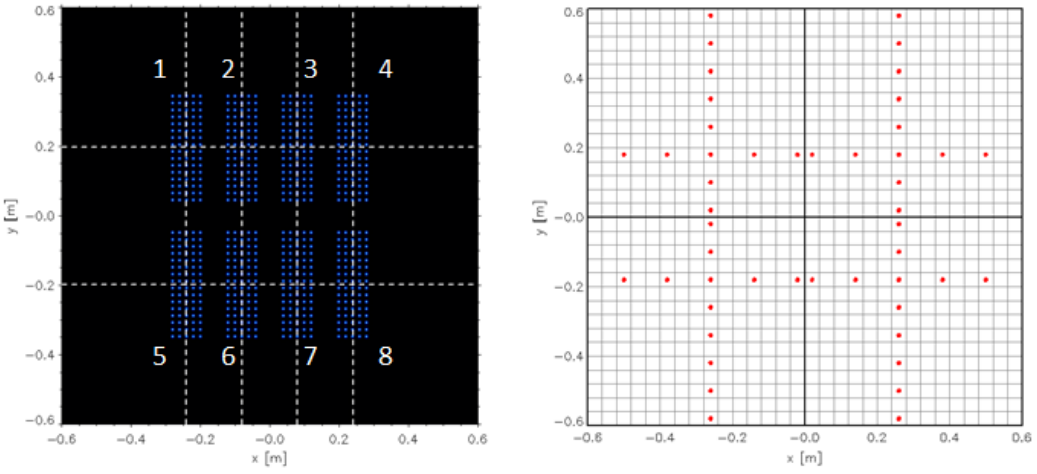

Figure 21: Left: Projection of the grid geometry on the calorimeter surface (in black). Blue circles represent the grid apertures, the white dashed lines pass through the beamlet group centers. Right: Position of the thermocouples (in red) on the diagnostic calorimeter. Horizontal and vertical lines are placed along the centers of the two beamlet group rows and of the two external beamlet groups columns (at about y = $\pm$20 cm and x = $\pm$ 24 cm respectively).

The heat deposited by the beam on the 900 copper blocks is transferred to the back side of the calorimeter where it is removed by the cooling system through a very small brazed area (thermal resistor), which connect the blocks to the calorimeter back plate, as shown in Figure 22. This permits to remove the heat in between two HV phases but to consider each block as "inertial" during the 10 s phase of the beam.

As indicated in Figure 22, the cooling system is formed by four inlet channels, one for each calorimeter panel, and one outlet channel. The temperature of the cooling water is measured by four KTY19 thermoresistors, one for each channel, and its flow by a flowmeter, so it is possible to have a calorimetric evaluation of the total power deposited on the calorimeter by the beam.

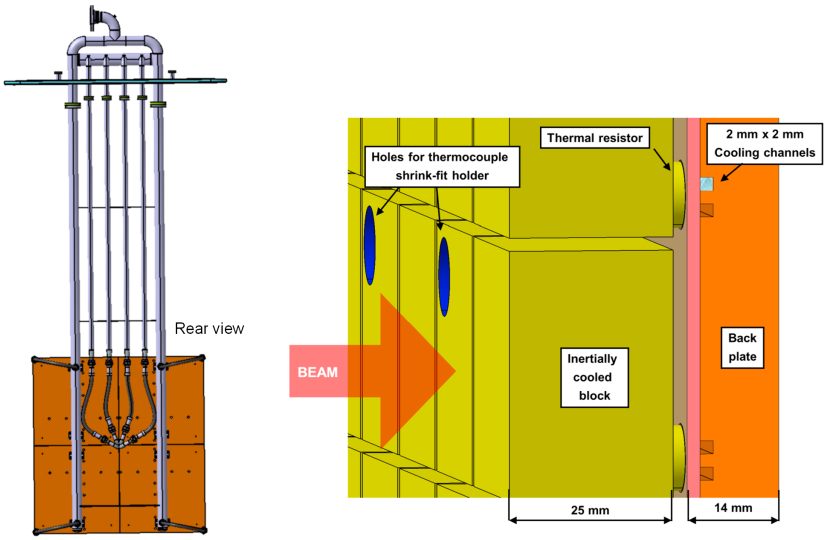

Figure 22: Left: Cooling channels of the diagnostic calorimeter. Right: Scheme of the block cooling from the back plate[44].

Despite the large ratio between the durations of the beam-on and the beam-off phases (10 seconds every 180 seconds), cooling is not always sufficient to reduce the temperature to its starting value before a new beam is extracted, especially at high beam power. See for example Figure 23, where a simulated temperature signal of a thermocouple over consecutive pulses is shown.

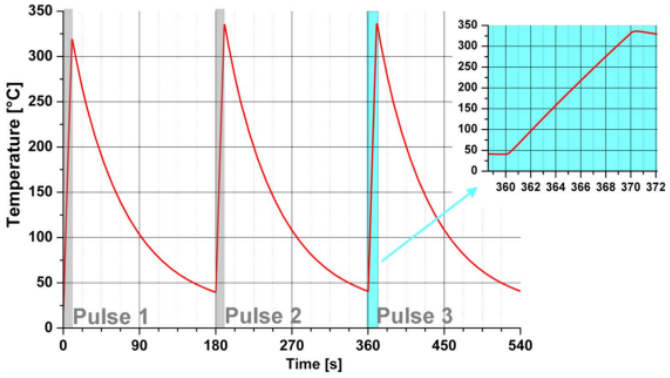

Figure 23: Simulation of thermocouple signal over consecutive pulses for a power density of 3 MW/m^2 [44].

As shown on the right side of Figure 22, for every block the thermal resistor through which heat is exchanged with the cooling channel is placed close to one of the block vertices. For this reason, as it will be discussed later, the temperature within a block may present high differences (up to 10 °C out of 200 °C after the beam-on phase for a power load of 1.5 MW/m^2) between the part closer to the cooling pipes and the opposite one (see Figure 24).

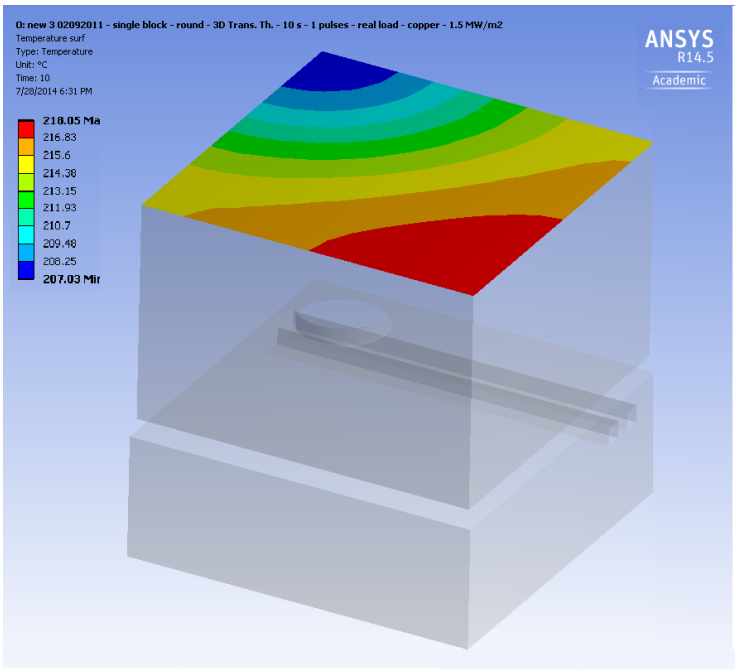

Figure 24: ANSYS simulation of temperature profile over a block surface at the end of the beam-on phase, with a power density of 1.5 MW/m^2. Courtesy of R.Nocentini (IPP).

The calorimeter is observed by a FLIR[1] A655sc camera with a field of view of 45° × 34° installed to one of the ports of the vacuum tank. Its resolution is 640 x 480 pixels and its spectral range is 7.8 - 14 μm. For every pulse, the camera receives a trigger signal about five seconds before the HV phase and it acquires IR images for one minute recording the 10 seconds beam-phase and the first part of the beam-off one. Since the camera is placed in a side port, the image is distorted and has to be corrected (see Figure 25). This aspect will be considered in section 4.2.

Furthermore the actual camera field of view (FOV) is limited by the port itself as shown in Figure 25.

For this reason in the image corners also part of the support of the camera (which is out of focus) may be seen. This of course affects the temperature measurement, as will be discussed in section 5. Nevertheless the area of the diagnostic calorimeter where the negative ion beam impacts is almost completely visible.

As mentioned above, thermocouples of type K NiCr- Ni were brazed in 48 blocks (Figure 21) providing temperature profiles along 4 lines. The temperature signals from these TCs have been used to absolutely calibrate the IR measurements over the whole calorimeter blocks, i.e to determine their emissivity (see section 4).

An example of the TC profiles along horizontal and vertical lines is given in Figure 26, where the temperature increase (due to the beam power deposition on the surface) mea-

[1]FLIR Systems, Inc., www.FLIR.com

sured by the thermocouples of the upper horizontal line and of the left vertical line are shown for ELISE pulse #6188, whose IR image was shown in Figure 25.

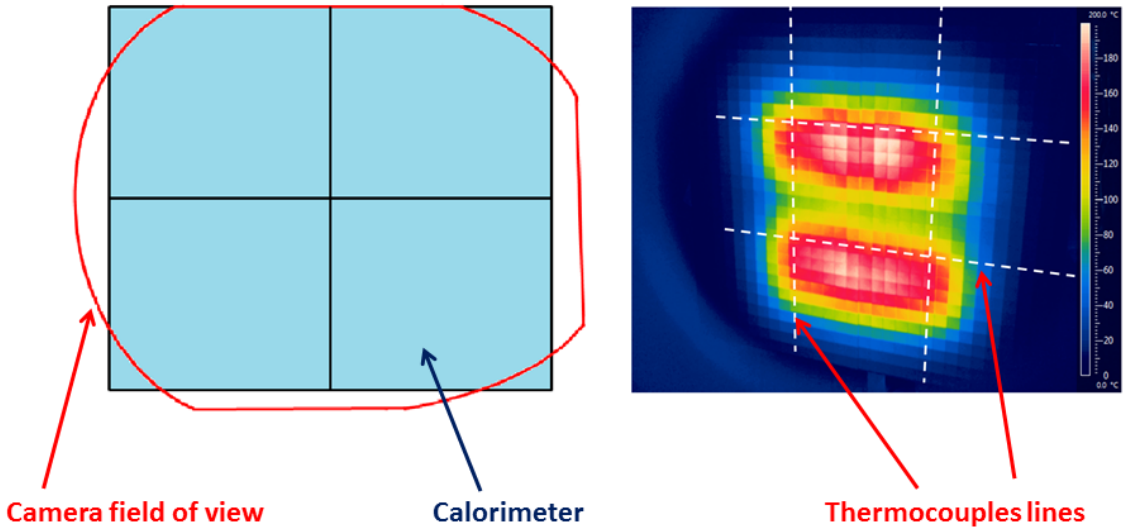

Figure 25: Left: Field of view of the IR camera. Right: IR image of the ELISE calorimeter after a beam phase for ELISE pulse #6188 (the background temperatures before the beam have been subtracted). The white dashed lines correspond to the TC position. The colorbars refers to the temperature increase induced by the beam power deposition.

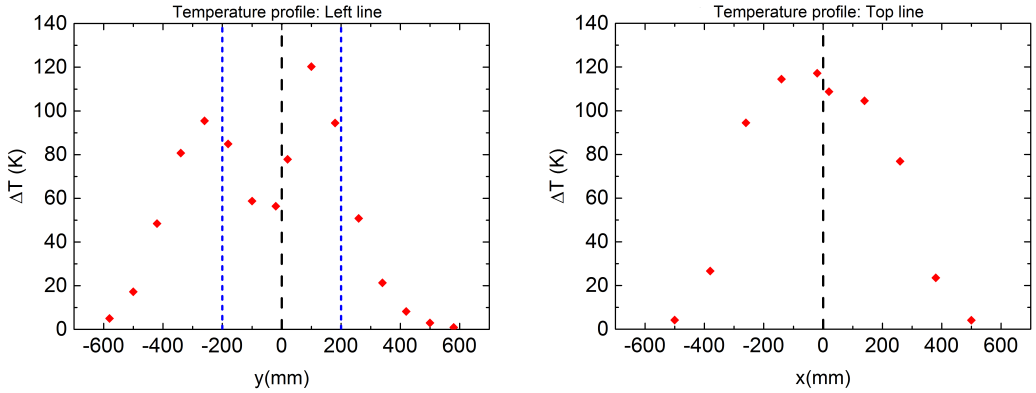

Figure 26: Thermocouple measurement of the temperature increase induced by the beam power deposition for ELISE pulse #6188. Left: Left vertical line of thermocouples; the black dashed lines represent the separation between the upper and the lower half of the calorimeter. The blue dashed lines give the expected position in vertical direction for the beamlet groups centers of the upper and lower half. Right: Upper horizontal line of thermocouples; the black dashed lines represent the separation between the left and the right half of the calorimeter.

The vertical profiles have a local minimum in the central part, meaning that divergence of pulse # 6188, about 1.5° according to beam emission spectroscopy (see section 3.2.3), is low enough to distinguish the two rows of beamlet groups. It is also possible to notice the vertical shift of the beam due to the magnetic filter field. Since the two rows of beamlet groups are well separated in fact (see Figure 25), the two maxima of the vertical

temperature profile for a non-deflected beam shoul be at the same vertical position of the projections of the beamlet group centers (±20 cm), that is not the case in Figure 26, where these positions are identified by the blue dashed lines.

The temperature profile along the horizontal line is given by a bell-shaped curve. The reason why in the central part the temperature increase is higher is that in the center the number of superimposing beamlets is larger than at the borders. For very low divergences four peaks corresponding to the beamlet groups should be seen. Another aspect that is interesting to notice in the horizontal profile is the huge temperature difference (8-9 K out of 115 K) between the two central thermocouples, which is not expected by looking at the IR image from Figure 25. This aspect will be considered again in section 4.3.

From the thermocouples datasheet, with a junction reference temperature of 0 °C, their error on temperature measurement is the larger one between ± 2.5 °C and the 0.75 % of the temperature expressed in °C. This is the error that will be used for calculation in the following. Various effects however suggest that it is reasonable to expect a (difficult to quantify) larger error. For example the temperature of the junction, which is about 20 °C, may have some fluctuations in the order of 2-3 °C. Furthermore, the acquisition system for the thermocouples is formed by two branches, two different electronic chains, one for panels 1 and 4 and the other for panels 2 and 3. The difference between the two measurement systems was determined with an oscilloscope to be a delay of about 5 ms between the signals measured by the two chains.

3.2.2 W-wire calorimeter

This calorimeter is positioned 1.8 m downstream the grounded grid. It is made by 100 tungsten wires spaced by 20 mm, and drawn vertically and horizontally in two vertical planes, spaced by 10 mm in the beam direction. The wires are heated by the beam and emit light. By observing them via an optical camera CCD it is possible to determine a profile of the beam. In order to have a low response time, the wires are thin (thickness: 0.2 mm). To compensate the wires expansion caused by their heating up, spring-loaded holders are used. At the moment this diagnostics is only qualitative since its calibration is not straightforward due to the difficult evaluation of the various heat exchange processes. However this calorimeter gives a basic idea of the beam position and homogeneity and future calibration could provide another instrument to determine a 2D map of the beam power density. Examples of W-wires images are shown in Figure 27.

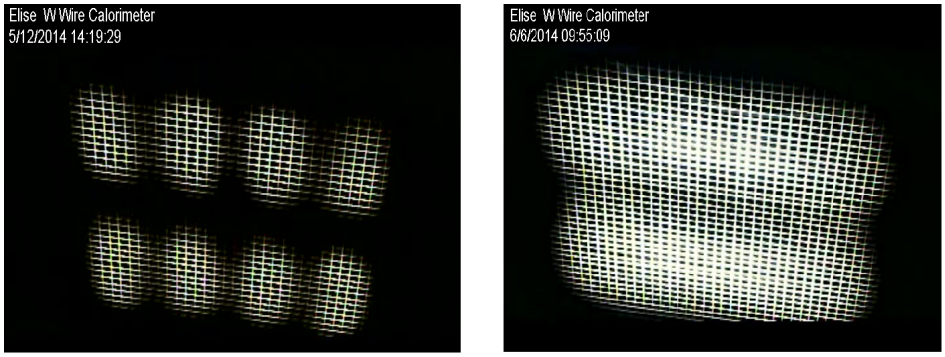

Figure 27: Photographs of the beam heating the tungsten wire calorimeter taken during two beam pulses at ELISE. Left: ELISE pulse #7268. Right: ELISE pulse #7911.

The main parameters of the shown pulses are listed in Table 4. The pulse on the left has a very low divergence, about 1°, so the beamlets group are clearly distinguishable. The pulse on the right has a much larger divergence, about 3°, so the single groups cannot be distinguished.

Parameters	**Pulse #7268**	**Pulse #7911**
Isotope	Deuterium	Hydrogen
divergence (on BES LoS #19)	0.89°	3.17°
Normalised perveance Π/Π_0	0.30	0.22
Extraction voltage	4.5 kV	7.5 kV
Acceleration voltage	25.1 kV	27.9 kV
Extracted current	9.5 A	20.9 A
RF power	125 kW	200 kW

Table 4: Main parameters of ELISE pulses #7268 and #7911.

3.2.3 Beam emission spectroscopy (BES)

Beam emission spectroscopy is based on the Doppler effect and it allows to measure the beamlet divergence and homogeneity. The Doppler effect is responsible for a shift in the central wavelength of an emission line emitted by a particle which is moving with a non-zero speed in the direction parallel to the optical axis of the detector (spectrometer).

Let θ be the angle between the optialc axis and the trajectory of the radiating particle (see Figure 28), then the wavelenght λ_0 is shifted to

$$\lambda = \frac{1 + \beta \cos\theta}{\sqrt{1-\beta^2}} \lambda_0 \tag{29}$$

where $v = \beta c$ is the particle velocity, and c is the light velocity.

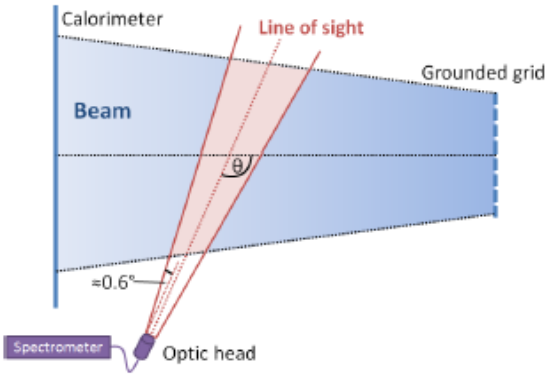

Figure 28: Scheme of one BES line of sight (in red). θ is the angle between the LoS and the beam axis.

BES system at IPP test facilities uses the (n = 3) excitation of Balmer line (H_α) due to its high intensity in the beam and its easy detectibility (it is in the visible wavelength range). Atoms in state n = 3 are created in the collision of the ions with the residual gas. For a negative hydrogen beam, the main reactions are:

$$\underline{H^-} + H_2 \rightarrow \underline{H^0}(n = 3) + H_2 + e \tag{30}$$

$$\underline{H^0} + H_2 \rightarrow \underline{H^0}(n = 3) + H_2 \tag{31}$$

$$\underline{H^0} + H_2 \rightarrow \underline{H^0} + 2H^0(n = 3) \tag{32}$$

where slow and fast particles are distinguished by underlining the latter.

In the case of the beam, a typical spectrum of the H_α emission for θ larger than 90° can be seen in Figure 29. The unshifted H_α peak (1) is present at $\lambda_0 = 656.3$ nm, while a second peak (2) appears at smaller λ: this is the Doppler-shifted peak. A third peak (3) appears between (1) and (2): this is the so-called stripping peak caused by negative ions whose electron is stripped (see section 1.3) inside the EG apertures before they reach the full acceleration energy. For stripping calculation see [11].

Given a beam with a certain divergence, its particle have a velocity distribution in the plane which is orthogonal to the beam itself. This distribution is responsible for the broadening of the shifted peak (2) in Figure 29, so the beam divergence δ is proportional to the width of the Doppler shifted peak. In general the half 1/e width is used to evaluate divergence in ELISE BES spectra.

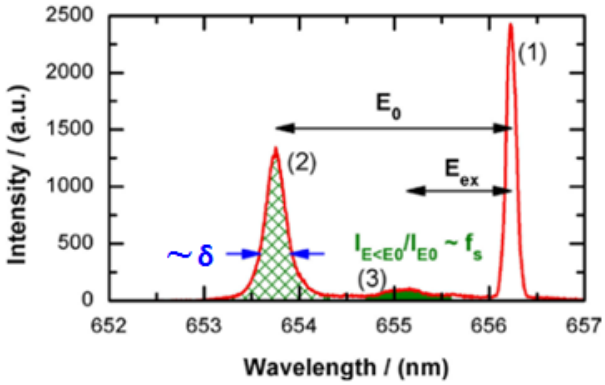

Figure 29: Typical spectrum of a negative ion beam from BES [46]. The beam divergence δ is proportional to the width of the shifted peak, which is due to neutrals at full acceleration energy.

Doppler-shifted spectroscopy is a simple and robust tool since no absolute calibration is necessary, it is non-invasive and the presence of magnetic fields or high potentials does not disturb the recorded spectra. At ELISE, the beamlet divergence is generally much higher than what is required for ITER NBI (around 2-3 °in average, however larger than 1°), so 2 meter downstream the grounded grid, i.e. where BES diagnostics is located, beamlets are generally superimposed. In addition, since each LoS goes through many beamlets, BES cannot give the divergence of the single beamlet, but an averaged divergence of the beamlets along the line of sight.

The Doppler shift spectroscopy system at ELISE is based on 20 LoS: 20 collimator lenses are installed on the ion source flange. Every lense focuses the collected light on an optic fibre which is conntected to an Acton[2] spectrometer which is equipped with a CCD.

[2]Princeton Instruments (Roper Industries Inc.), www.princetoninstruments.com

The aperture angle of the lines of sight, indicated in Figure 28, was measured to be about 0.6°.

The spectrometer spatial resolution is 7 pm/pixel and its apparatus profile, i.e. the measured intrinsic width of a line, is 0.042 nm. The main features of the apparatus are kept into account for correcting the BES evaluation of divergence.

As shown in Figure 19, 16 LoS are arranged in horizontal direction, providing a vertical divergence profile, and 4 are arranged in vertical direction, providing a horizontal divergence profile. The reason for this difference in the number of LoS used in the two direction is that most of the possible inhomogeneities in the beam divergence are expected to occur in the vertical direction, due to the horizontal direction of the filter field, which leads to a vertical deflection of the beam. In the following, ELISE horizontal LoS will be numbered from bottom to top with numbers from 1 to 16, whereas the vertical ones will numbered from right to left using numbers from 17 to 20. Using again a coordinate system whose x axis is horizontal, y axis vertical and the origin is given by the center of the diagnostic calorimeter, BES vertical LoS are placed at x= -24, -8, 8, 24 cm that are the position of the centers of the beamlet groups introduced in section 3.1, whereas the horizontal are in between y= -37.5 cm and y= 37.5 cm with a 5 cm spacing. In the following, when single divergence estimates will be given for a beam, one of the two central vertical LoS, #19, will be used.

The angle of observation of the various LoS with respect to the beam is 50°. This means that, according to Eq. (29) in the typical BES spectra at ELISE, the Doppler shifted peak appears at λ which are larger than λ_0.

Presently, BES is the only diagnostics used to evaluate divergence at ELISE, so it will be largely used for comparison in section 6.1, when divergence will be evaluated from the data of the diagnostic calorimeter.

The error on the divergence determined by BES depends on the absolute value of the divergence and generally it is above 10 %. In the range 1.5-3 °, for example, it is reasonable to assume a 20 % error in the measurements [47].

4 Calibration of the IR camera

As mentioned in section 3.2.1, the main task of this thesis is to characterise the ELISE beam in terms of divergence and homogeneity by means of IR images of the diagnostic calorimeter.

In this chapter it is described how the acquired IR images are used to determine a 2D map of the power density deposited by the beam on the calorimeter: this is the first step of the performed analysis.

By means of IR thermography, some principles of which are discussed in section 4.1, for each pixel of the camera, a temperature can be determined, providing a 2D map of the temperature on the calorimeter surface. Under the reasonable assumption that the specific heat of copper does not change significantly in the range of temperatures that may be reached by the calorimeter during ELISE operation (between 20 °C and 400 °C), the power deposited by the beam is proportional to the temperature increase and can be derived by simple calorimetric calculations (see later in this Chapter), as the copper blocks are inertially cooled.

In order to use IR thermography to determine a 2D map of the temperature two requirements are mandatory:

- Correction of the perspective, since the IR image, as shown in Figure 25 (see section 3.2.1), is taken by looking the calorimeter from a side port. This aspect will be considered in section 4.2

- Camera calibration: the proper emissivity of the calorimeter surface has to be determined, and whether this value changes from block to block (coating uniformity) or in time has to be assessed. This calibration could be done by matching the camera measurements with the thermocouples. See section 4.3.

Actually the camera measures the temperature of the blackening layer deposited on the block surface while the thermocouples measure the temperature in the block volume, 1 cm below the block surface. So, in principle the two temperatures are different, but in practice, this difference can be neglected in the beam-off phase, when thermal equilibrium between the block volume and its surface is achieved. For this reason the beam-off phase has been used for comparing the results of the temperature measurements from the thermocouples and the IR camera.

Directly after switching off the beam, the difference between the maximum temperature on the block surface and the temperature in the thermocouple location is very high. From simulations performed in ANSYS (see Figure 30) with a beam power density of 1.5 MW/m^2, i.e. half of the maximum design power, the surface temperature is about 220 °C, while the block one is about 180 °C, so the difference is around 20 % . After 2 seconds the temperature difference is below 1 %, so the block can be considered to be in thermal equilibrium, and the two temperatures can therefore be compared (see Figure 31).

These simulations do not consider the influence of the coating layer, that will be discussed in section 4.2.

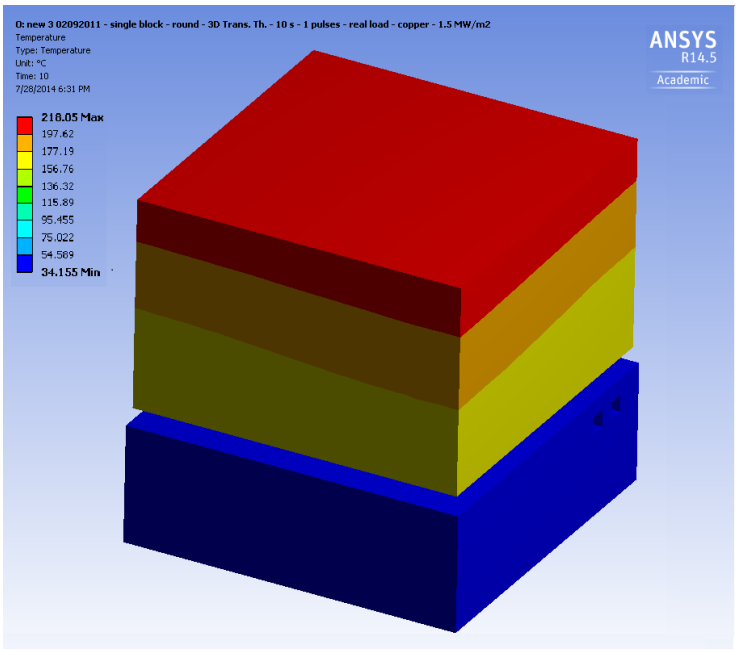

Figure 30: Simulation of the temperature profile inside a block at the end of the beam-on phase for a power density of 1.5 MW/m^2. Courtesy of R. Nocentini (IPP).

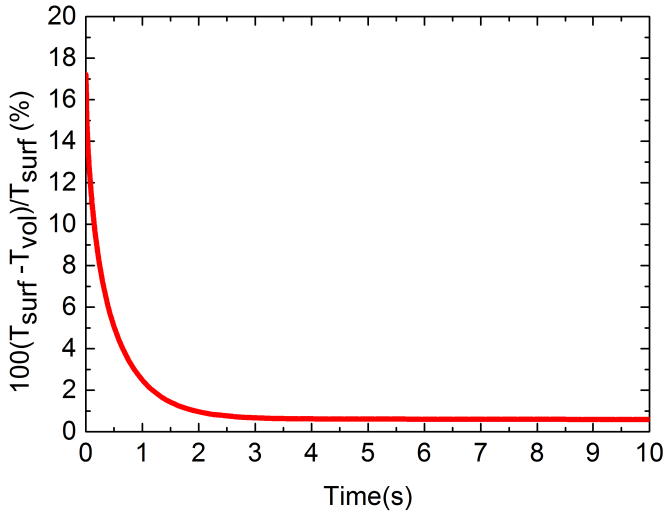

Figure 31: Time evolution of the difference (in percentage) between TC and (the maximum of) the surface temperature in the beam-off phase. Data are taken from ANSYS simulation with the power load of 1.5 MW/m^2 over a single block. Courtesy of R. Nocentini (IPP).

4.1 Principles of thermography

A blackbody is an object which absorbs all radiation impinging on it at any wavelenght and, according to Kirchhoff's law, it is also capable of emission at any wavelenght. To be more precise, Kirchhoff's law states that its absorptance α_λ and its emissivity ϵ_λ are the same at any wavelength. The spectral distribution of a blackbody radiation is described by Planck's formula:

$$w_\lambda = \frac{8\pi hc^2}{\lambda^5(e^{hc/\lambda kT} - 1)} \tag{33}$$

where w_λ is the intensity of the radiation emitted at the wavelength λ, h is the Planck constant, k the Boltzmann constant, c the speed of light and T is the temperature of the blackbody. By integrating Eq. (33) over the whole spectrum, one gets the Stefan-Boltzmann law for a blackbody.

$$W = \sigma T^4 \tag{34}$$

which gives the intensity W of the radiation emitted by the blackbody, where σ is the so-called Stefan-Boltzmann constant.

A blackbody is an ideal emitter and in general the emittance of a body is lower than a blackbody's one. The emittance of a body is described by the so-called emissivity ϵ, whose range is [0,1], where 1 represents a blackbody. In the following an average emissivity ϵ of the coating layer in the camera spectrum will be determined.

There are three processes preventing a real object from acting like a blackbody: absorption, reflection and transmission. They are described through three parameters (wavelength dependent) called absorptance (α_λ), transmittance (τ_λ) and reflectance (ρ_λ) which must obey Eq. 35.

$$\alpha_\lambda + \rho_\lambda + \tau_\lambda = 1 \tag{35}$$

So the effects of other radiation sources and the role of the environment in which the camera and the radiating object are placed have to be taken into account. Referring to Figure 32, representing the scheme of the IR measurement, let T_{obj} be the object temperature and W_{obj} be its radiated power (as a blackbody), let T_{refl} be the temperature of other radiating objects, whose radiation is reflected by the object surface and therefore seen by the camera, W_{env} the power radiated by the environment and τ an average value of its transmittance. Then the total power on the camera is

$$W_{\text{tot}} = \epsilon\tau W_{\text{obj}} + (1-\epsilon)\tau W_{\text{refl}} + (1-\tau)W_{\text{env}} \tag{36}$$

Assuming the camera to produce an output signal S proportional to the received power W, than the signal due to the object may be extracted as

$$S_{\text{obj}} = \frac{1}{\epsilon\tau}S_{\text{tot}} - \frac{1-\epsilon}{\epsilon}S_{\text{refl}} - \frac{1-\tau}{\epsilon\tau}S_{\text{atm}} \tag{37}$$

Once S_{tot} is measured and S_{refl} and S_{env} are estimated, S_{obj} is obtained.

In summary, for the IR data analysis, the parameters that have to be known to evaluate temperatures are:

- the object emissivity ϵ
- the object distance D_{obj}
- the temperature of the environment T_{env}
- the reflected ambient temperature T_{refl}

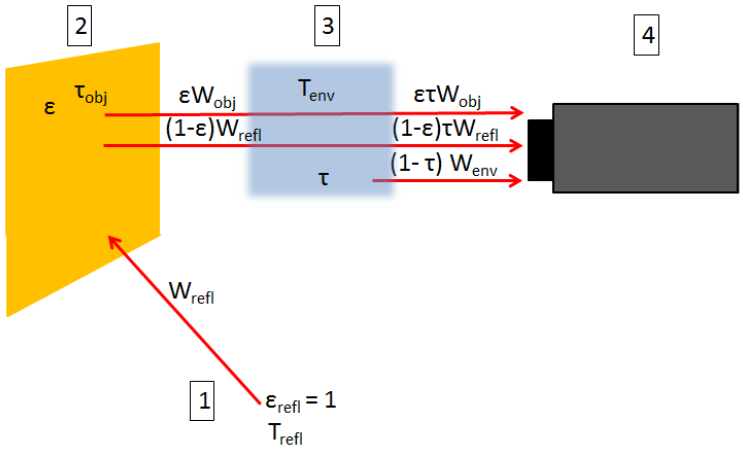

Figure 32: Scheme of the IR measurement. 1) Surroundings, 2) Calorimeter, 3) Environment, 4) Camera [48].

For the analysis an average distance of 2 m can be determined from the positions of the calorimeter and of the port in which the camera is placed, while the emissivity of the blackening layer will be determined in section 4.3. For the temperatures T_{env} and T_{refl} reasonable values will be presented in the following.

4.2 Data processing

As mentioned in 4.1, to describe the beam its total power deposition is used. For this reason the temperature increase caused by the power deposited during the beam phase onto the calorimeter is evaluated by the difference between the frame just before the beam and a frame after the beam. From Figure 33, in which the frame before the beam has been subtracted to obtain the temperature increase, it may be seen that the IR temperature signal exhibits a considerably more rapid increase than the TC signal when the beam hits the calorimeter surface. After this rapid increase, the two signals grow with a similar slope and after the beam is switched off, if the emissivity of the camera is set properly, they are superimposed in the cooling phase.

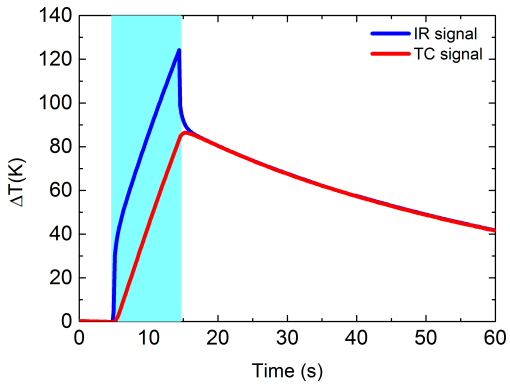

Figure 33: Comparison between TC and IR temperature signals for a proper emissivity value. The shaded region represents the beam-on phase.

The difference between the temperature of the block surface and volume (30 °C out of

120 °C at the end of the beam-on phase) is larger, in percentage, than what was found by simulation in which the layer was not considered (Figure 30), suggesting that this difference is not only due to the finite conductivity of Cu, but also to the adhesion of the blackening layer to the block surface.

The difference between the two signals (IR camera and TC) however, can still be considered negligible about 2 seconds after the beam is switched off (see Figure 33). For this reason, in the following, the temperature increase ΔT due to the beam power deposition is evaluated by considering a frame 1.8 s after the HV phase. In addition, looking at the TC signal, the temperature difference between this frame and the instant immediately after the beam, is quite small (the cooling rate is about 0.1-0.2 °C per frame, see below), therefore this temperature is a good estimate of the temperature at the location of the thermocouples when the beam is switched off.

The temperature within a block, as discussed in 3.2.1, may present high differences between the part closer to the cooling pipes and the opposite one (see Figure 24). For this reason, and also for smoothing local coating disuniformities, the pixel temperatures are averaged inside each block.

As discussed at the end of section 4.1, in order to evaluate temperatures, some parameters have to be set. The temperature T_{refl} is mainly determined by the presence of the cryopumps, whose behaviour is not exactly reproducible. The value $T_{\mathrm{refl}} = 14$ °C has been chosen from the analysis on the previously used beam dump calorimeter [45]. An average distance of 2 m between camera and calorimeter has been considered and T_{env} was fixed to 20 °C.

The influence of T_{refl} on the results of temperature measurements is higher when the temperature of the investigated radiating object, i.e. the calorimeter, gets closer to it. This means that the temperature measured on the border blocks of the calorimeter (those which are less heated by the beam and therefore have a temperature quite close to T_{refl}) may present a larger systematic error due to fluctuations of T_{refl} around the set value. This error could turn into an error in the emissivity estimate for those blocks. The estimate for the inner blocks is, of course, more robust.

The sampling frequency of 6.25 Hz (so one frame every 0.16 s) represents a compromise between the accuracy in the reconstruction of the time evolution of the calorimeter temperature and the data storage. The total acquisition time was set to 1 minute, so 375 frames. Also this choice is a compromise between the capability to describe the cooling phase and the data storage. With the present settings, each video has a dimension of about 230 MB. To estimate the beam power deposition however, only two frames are necessary, one before and one after the beam.

The software provided by FLIR together with the camera itself, allows to set all of the parameters described above and to determine online the temperatures of some user-defined spots or profiles. The data are saved in a *.seq file, a movie in which calibration constants and the data corresponding to each pixel and each frame are saved.

In order to have maximum freedom in the data analysis, it was desirable to access the camera raw data. For this reason a non-disclosure agreement was signed between IPP and FLIR, which allowed to access both the raw data (the pixel counts) and all the constants together with the formulas used for the temperature evaluation. In principle this permits to define different settings parameters, such as distances or emissivities, for the different pixels.

A program for reading the *.seq file as a binary file was therefore developed and is now used for data analysis. So far, the reading of the *.seq file has been done off-line, but

next step will be to use this program for online extraction and analysis of the raw data, in order to have information on the beam power deposition directly after the beam pulse is off.

Instead of correcting the perspective, lines were drawn in the IR image along the separations between the blocks, thus defining the geometry of the calorimeter, as shown in Figure 34. These lines can clearly be seen (especially in the beam-on phase) since the temperature at the position of the separation is lower than within the blocks (see the left side of Figure 35),

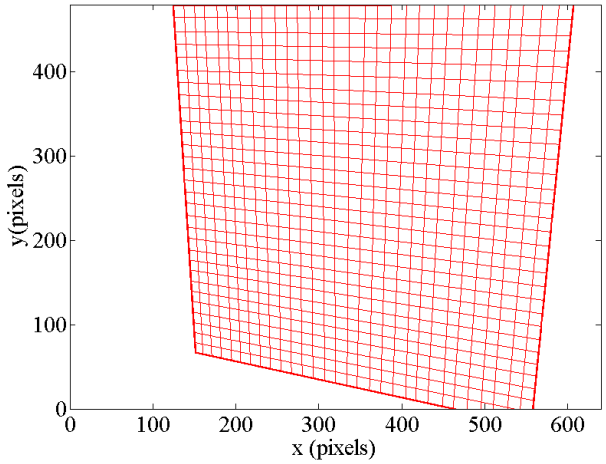

Figure 34: Position and dimension of the calorimeter in the pixel coordinate system of the IR camera. The red lines represent the separations between the blocks.

By determining from one IR image the positions of the pixels which are closer to the two extremes of each of these lines, their equations in the pixel coordinate system were determined and, by solving the linear system of equations associated to the block separation lines, the positions of each block vertices (in pixels) have been found. Since as just discussed, in the separations between the blocks the temperature profile is not continuous, the pixel closer to the block sides were neglected as shown in Figure 35.

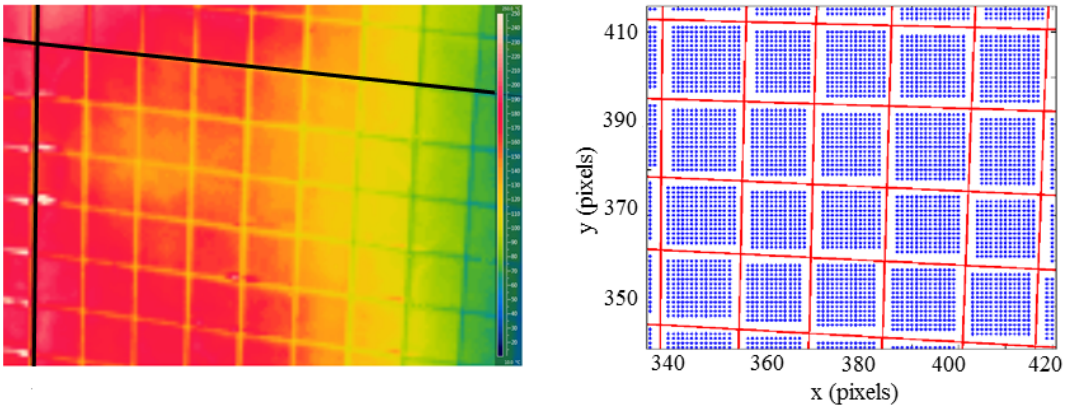

Figure 35: Left: Zoom of an IR image. Black lines are the two axes of the calorimeter. Right: Zoom of the calorimeter geometry. Red lines represent the separations between blocks, blue points the pixels selected for the temperature evaluation.

After extracting the pixel counts of the pixels for the selected frames, one before the

beam and one 1.8 s after the beam, they can be converted in temperature, according to the calibration formula given by FLIR.

4.3 Emissivity determination

The camera calibration procedure consists mainly in determining an emissivity ϵ that is suitable to describe the coating of the calorimeter i.e that allow to match the determined temperatures to the results from the TCs.

As discussed in section 4.1 the intensity W of the radiation emitted by an object may be written as a function of its temperature T, its emissivity ϵ and some other parameters depending on the conditions in which the measurement is performed. Neglecting for simplicity the last ones this means that W may be written as

$$W = f(T, \epsilon) \tag{38}$$

The formula used for calculations is not trivial, however it can be inverted extracting ϵ as a function of the temperature and of the radiation intensity

$$\epsilon = g(T, W) \tag{39}$$

The intensity of the radiation is derived from the pixel counts of the camera and temperature is measured by the TCs under the previously motivated assumption that this can be used as an estimate for the surface temperature in the beam-off phase. What is found, is the ϵ value for which the temperature derived from the IR camera is in agreement with the thermocouple results.

This calculation was performed for the cooling phase, when the temperature within each block is more uniform. Since after the beam-on phase the temperature does not always return to its previous value (see section 3.2.1), the calibration has been done by taking into account the data of the first beam of each operation day, so that no influence from the previous pulses is registered.

For each pulse, the data of 25 frames (every 10 frames, so every 1.6 s) in the cooling phase have been extracted (see the red circles in Figure 36) and used to get a single emissivity value for each block hosting a thermocouple.

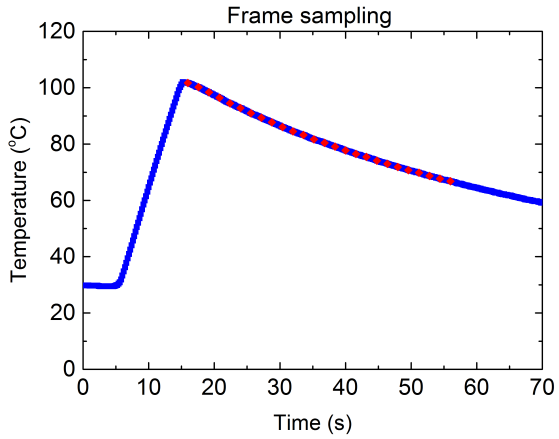

Figure 36: Typical temperature signal from a thermocouple. Red circles represent the frames used for the emissivity determination.

It has to be noted that due to the electronic chain each thermocouple has a different temperature offset. This offset may vary a lot from TC to TC, even within panels with the same electronics, for example panels 2 and 3, as shown in Figure 37.

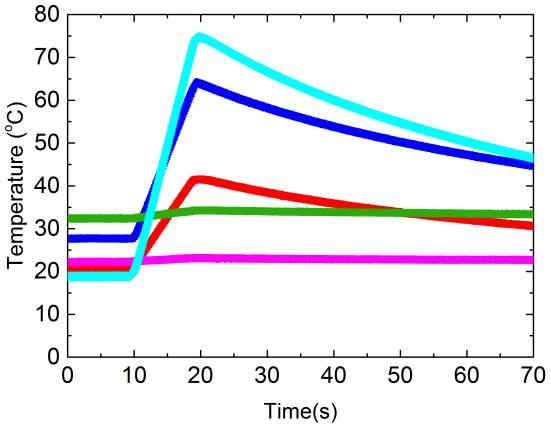

Figure 37: Signals from different thermocouples from panels 2 and 3. Different temperature offsets are evident before the beam-on phase, in the range 0-10 s.

For the power deposition estimate this is not a problem since temperature differences are used, but for the calibration of the IR camera an absolute temperature is needed. So the thermocouples are used to measure the temperature increase ΔT, and the initial temperature of the blocks is determined by measuring the water temperature in the cooling channels of the four panels, whose offset for a reference temperature of 20 °C has been measured separately.

The errorbars for a single measurement (matching of one TC for one frame in one shot) have been obtained by propagation of the thermocouples and KTY19 measurement uncertainties (mentioned in section 3.2). These errorbars are around the 5-6 % for the outer thermocouples, where temperature increase is lower, and around 2 % for the inner ones, most heated by the beam. Averaging over the selected frames the statistical error for the ϵ determination in one pulse is around 1 %.

By averaging in time (that is day by day) the values of ϵ found for each block associated to a TC, it is possible to get four emissivity 1D profiles along the TC lines shown in Figure 21 and assess the coating uniformity. These profiles are shown in Figures 38 and 39. The shaded regions correspond to the regions of the calorimeter which are more heated by the beam. In the horizontal direction this is between x = -30 cm and x = 30 cm. This range was chosen as reference since the external beamlet groups have centers in x = $\pm$ 24 cm and the half width of a beamlet group (at the GG) is 5 cm. In the vertical direction two areas have been shaded. They have been determined with the same principle, considering an average downward deflection of the beam of 6 cm and the vertical half width of the beamlet groups (at the GG) of about 15 cm. So they have been centered at y = 14 cm and y = -26 cm respectively and have a width of 30 cm.

From Figures 38 and 39, it can be seen that emissivity exhibits local minima in the most heated regions. This could suggest that the power deposition by the beam is eroding and degradating the coating and so reducing its emissivity.

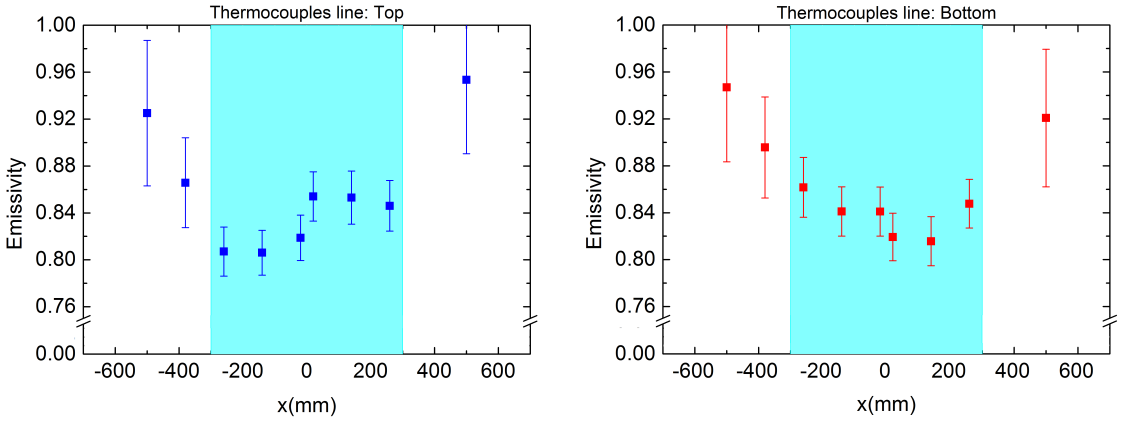

Figure 38: Emissivity profiles along horizontal TC lines as time average (day by day) of the values of the analysed pulses. The shown errorbars are those of the single measurement (matching of one TC for one frame in one shot). Left: top TC line. Right: bottom TC line. The shaded region corresponds to the parts of the calorimeter which are more heated by the beam.

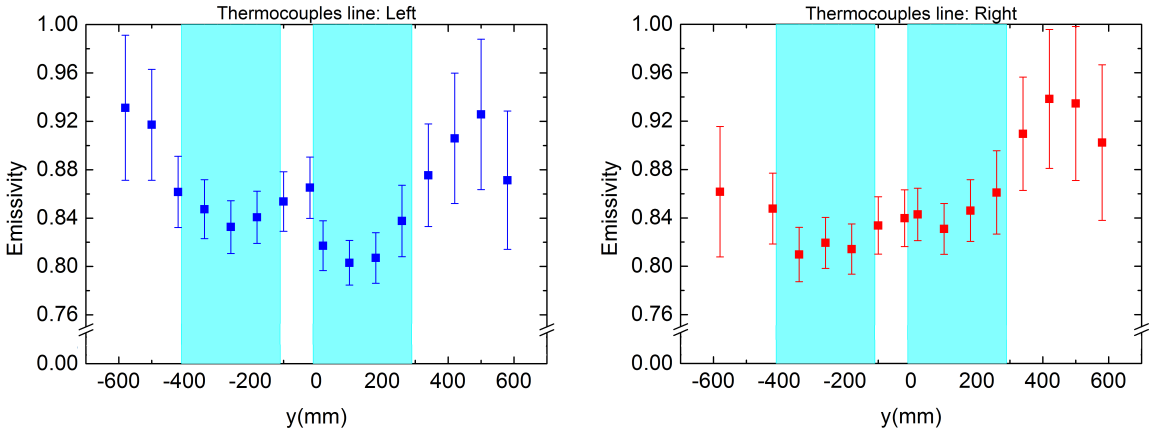

Figure 39: Emissivity profiles along vertical TC lines as time average (day by day) of the analysed pulses. The shown errorbars are those of the single measurement (matching of one TC for one frame in one shot). Left: left line. Right: right line. The shaded region corresponds to the parts of the calorimeter which are more heated by the beam.

Considering the trend of ϵ with respect to time for a central TC (coordinates x = 20 mm, y = 180 mm), shown in Figure 40, some scatter is clearly visible, but also a decreasing trend seems to occur. The errorbars displayed in Figure 40, are those of single measurements, that are around 2 % for a central thermocouple.

This decreasing trend is in agreement with the hypothesis of some coating erosion due to the beam itself. These results may be verified by an optical inspection of the calorimeter coating during the next opening of the tank, meanwhile they suggest to continue monitoring the coating emissivity regularly.

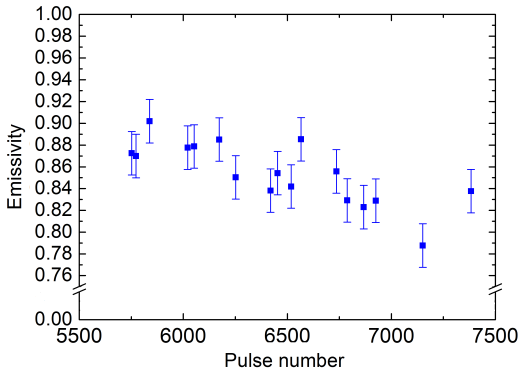

Figure 40: Emissivity estimate vs time (as pulse number) for a central thermocouple. The shown errorbars are those of the single measurement (matching of one TC for one frame in one shot).

From Figures 38 and 39 it can be seen that the emissivity estimates found in panel 2 and 3 are slightly higher than in panels 1 and 4. The average in panel 1 and 4 is 0.83, whereas in panel 2 and 3 it is 0.86, two slightly different values.

4.4 Test of the emissivity calibration

To test whether this calibration, performed with low power pulses ($\Delta T < 60°$), the first pulses of each operation day, is valid also for higher power pulses, additional measurements have been performed.

A matching between the result of IR camera and thermocouples on a horizontal and vertical line was performed for a pulse with higher power (in the middle of an operation day). In this test, whose results are shown in Figures 41 and 42, ϵ was set to $\epsilon = 0.85$ (a global average) for all the calorimeter blocks . Temperature differences between the frame before the beam and the one 1.8 s after have been used to neglect the TC offset due to the electronic chain.

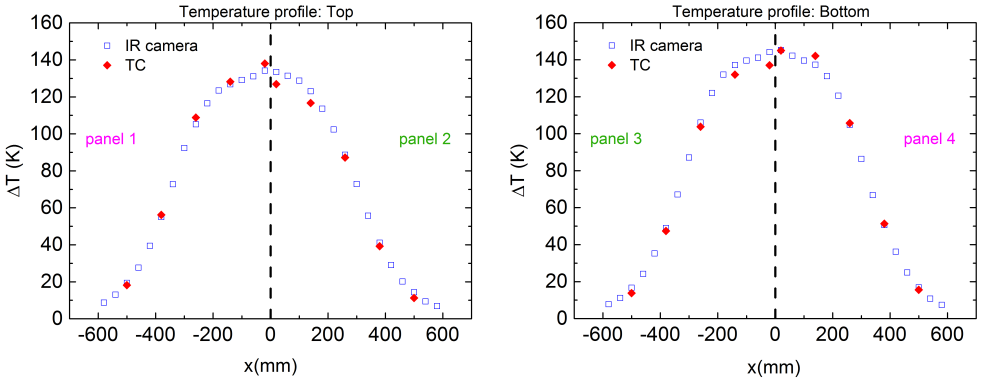

Figure 41: Temperature measurements along horizontal TC lines for ELISE pulse # 6461. The red series gives the TC measurements, the blue one gives the results from the IR camera for $\epsilon = 0.85$. The black dashed line represents the vertical axis of the calorimeter.

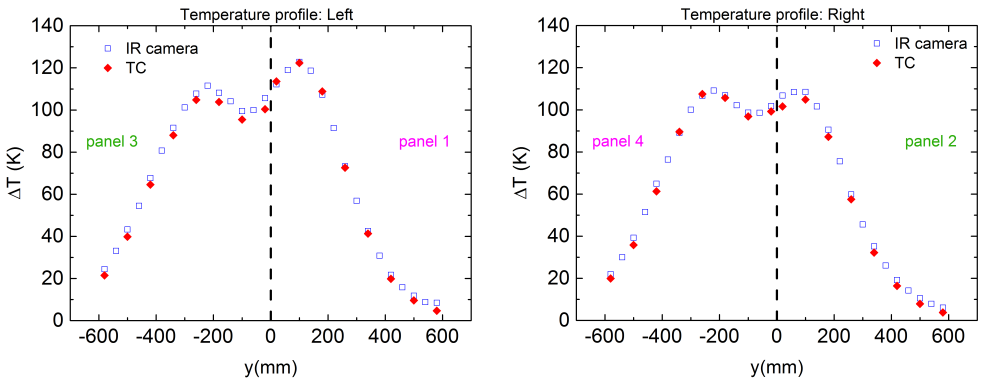

Figure 42: Temperature measurements along vertical TC lines for ELISE pulse # 6461. The red series gives the TC measurements, the blue one gives the results from the IR camera for $\epsilon = 0.85$. The black dashed line represents the horizontal axis of the calorimeter.

The horizontal and vertical profiles from the two diagnostics are quite similar. In both cases it is possible to see bell-shaped horizontal profiles, with a flatter region in their center, and the vertical profiles have a local minimum in the central part, meaning that divergence of pulse # 6461 is low enough to distinguish the rows of groups.

As a reminder, from the thermocouple datasheet, for a junction reference temperature of 0 °C, the maximum error on one measurement is the higher between 2.5 °C and 0.75 % of the measured temperature. Some points have a difference between the TC and IR measurements that is around 7 °C out of 140 °C, about 5 %.

Moreover, it is reasonable that the error on the TC measurement is higher than what is derived from the data sheet, so a 5 % difference is a good result. Some reasons could lie for example in the electronic chain or in the temperature of the reference junction of the thermocouples, which is about 20 °C and presents some fluctuation in the order of 2-3 °C. However, one thing has to be noticed: the points standing out of the discussed statistical error range lie in panels 2 and 3 that, as discussed in section 3.2.1, have the same electronic chain, whereas the differences in panel 1 and 4, which have another electronic chain, are generally within the errorbars.

A possible explanation for this behaviour are emissivity differences. In this case however, emissivity of panel 2 and 3 should be quite higher than 0.86 (the average calculated before). It was found that a perfect matching can be achieved for the upper line by setting to $\epsilon = 0.83$ the emissivity of panel 1 and 4 (the average calculated before) and to $\epsilon = 0.91$ the emissivity of panel 2 and 3. The results are shown on the left side of Figure 43. Such huge difference in the emissivity (10 %) is not expected, at least not with this strange scheme in which panels in opposite positions have the same behaviour. This scheme is more likely to be due to the different electronic chains. Since, with respect to the results of section 4.3, the emissivity which has to be changed for achieving a better matching is the one of panels 2 and 3, while the previously estimated $\epsilon = 0.83$ gives an almost perfect agreement between the two diagnostics in panel 1 and 4, it is reasonable to assume that the different emissivity evaluation is due to the electronic chains of panels 2 and 3 and consider the estimate $\epsilon = 0.83$ as more robust.

Assuming $\epsilon = 0.83$ as a correct emissivity estimate, the temperature measured by the TC in panels 2 and 3 is always lower than the estimate from the camera and a slight miscalibration of the electronics of panel 2 and 3, resulting in a gain different from expected, could be considered as an explanation for the differences in the temperature

measurement.

Setting $\epsilon = 0.83$ and assuming an under-estimate around 6-7 % in panels 2 and 3, the measurements of the two diagnostic are in fact in very good agreement (see the right side of Figure 43).

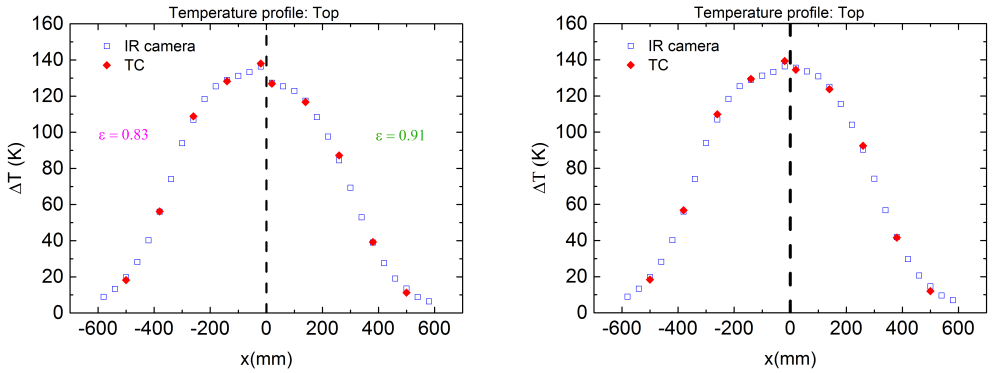

Figure 43: Left: Matching of the results of the temperature measurements from the TCs and the IR camera along the upper line of TCs. Left: By setting $\epsilon = 0.83$ in panel 1 and $\epsilon = 0.91$ in panel 2. Right: By setting $\epsilon = 0.83$ for all the calorimeter blocks and assuming a miscalibration of 6 % for the TCs of panel 2. The black dashed line represents the vertical axis of the calorimeter. ELISE pulse #6461.

Considering a pulse with lower power (about half of the previuos one, and in the order of those used for the calibration) the differences which are found in panel 2 and 3 assuming again an average of $\epsilon = 0.85$, are less evident, as it is shown in Figure 44.

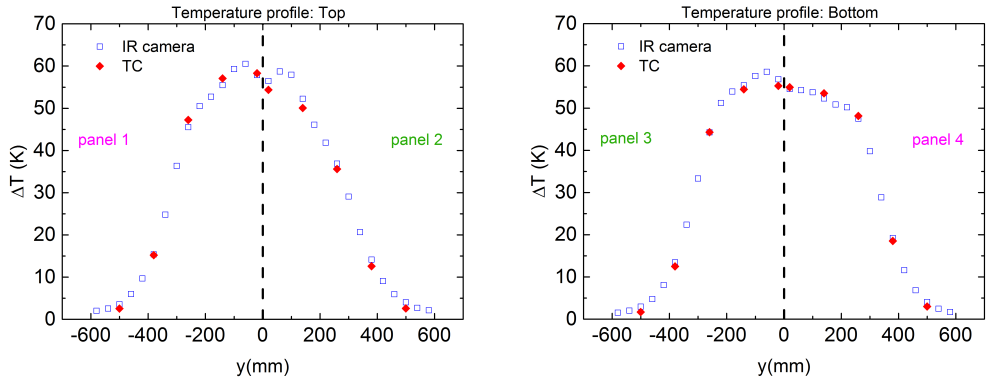

Figure 44: Temperature measurements along vertical TC lines for ELISE pulse # 5752. The red series gives the TC measurements, the blue one gives the results from the IR camera for $\epsilon = 0.85$. The black dashed line represents the horizontal axis of the calorimeter.

The value of emissivity which fits best the data of panels 2 and 3 is found to be $\epsilon = 0.88$, while $\epsilon = 0.83$ can guarantee again a good matching for panels 1 and 4 (see Figure 45, on the left). Again the signals of panel 2 and 3 may be matched satisfactorily also assuming a sistematic error of 6-7 % in the TC measurement (Figure 45, on the right).

The fact that $\epsilon = 0.83$ can provide a good agreement between the measurement of the two diagnostics in a wide temperature range (ΔT = 30-150°C) for panels 1 and 4, while the emissivity value to obtain a similarly good agreement for panels 2 and 3 has to be changed

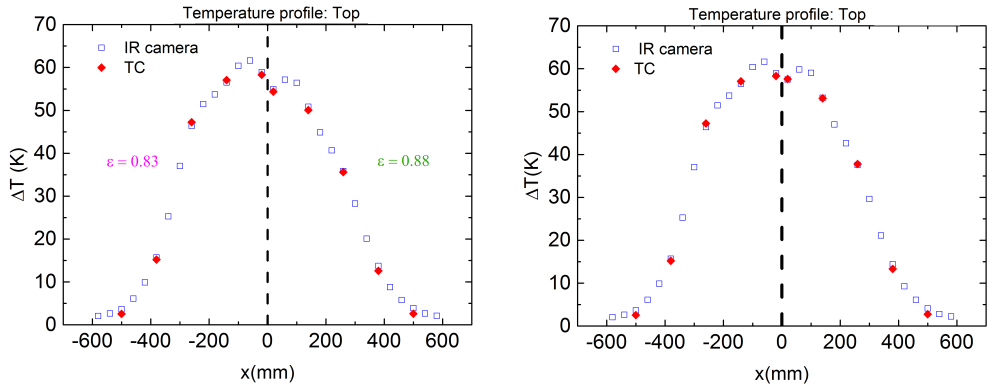

Figure 45: Matching of the results from TCs and IR camera along the upper line. Right: By setting $\epsilon = 0.83$ for the TCs in panel 1 and $\epsilon = 0.88$ for the TCs in panel 2. Right: By setting $\epsilon = 0.83$ for all the calorimeter blocks and assuming a miscalibration of 6 % for the TCs of panel 2. The black shaded line represents the vertical axis of the calorimeter. ELISE pulse #5752.

(from 0.86 to 0.91) suggests that $\epsilon = 0.83$ is a better emissivity estimate and that a slight miscalibration in the electronic chain of panels 2 and 3 is a reasonable option. In particular the latter hypothesis is supported by the fact that it allows to achieve a good agreement between the two diagnostics in the investigated temperature range (ΔT = 30-150 °C) [3]. The goodness of this choice will be however tested again in the next section, in which the estimate of the power deposited by the beam on the calorimeter surface obtained by the data from the IR camera, will be compared to the estimate of the beam power deposition from the water calorimetry.

4.5 Comparison with water calorimetry

Calorimetry allows to determine the heat absorbed by an object from its temperature increase. In the case of the diagnostic calorimeter, two calorimetric estimates can be performed. One of them is from the water flowing in the cooling channels and the other from the copper blocks on the front side of the calorimeter. Since the heat deposited on the blocks surface is transferred to the back side of the calorimeter where it is removed by the cooling system, the two estimate should be compatible. It is however reasonable to expect a slightly lower estimate from IR thermography. The temperature increase of the blocks surface (the one which is seen by the IR camera) is in fact due to the portion of the beam which directly hit the surface. The power which is deposited in the separations between the blocks instead, does not determine an increase of the surface temperature, but it however heats the back plate and is removed by the cooling. The ratio between the total surface of the blocks and the calorimeter surface is given by

$$R = \frac{900 \times (0.038\ \text{m} \times 0.038\ \text{m})}{1.2\ \text{m} \times 1.2\ \text{m}} \sim 0.90 \tag{40}$$

For this reason, if the camera is well calibrated, the ratio between the two power estimates, is expected to be between 0.90 and 1.

[3] Just before the deadline to submit this thesis, the hypothesised miscalibration of the elecronic chain of panels 2 and 3 was confirmed experimentally.

In the case of IR thermography, since the blocks are inertially cooled, an average value of the power deposited by the beam can simply be determined as

$$P = \frac{c_{Cu}\rho_{Cu}V\Delta T}{\Delta t} \tag{41}$$

where ΔT is the block temperature increase, Δt the beam duration, V the block volume, c_{Cu} the specific heat and ρ_{Cu} the density of copper.

For the water calorimetry the principle is the same with all the quantities referred to water, but an integration to infinity is performed, to consider all the deposited power. So the total deposited power is estimated as

$$P = \frac{\int_0^\infty c_{\mathrm{H_2O}} m_{\mathrm{H_2O}} \Delta T(t) dt}{\Delta t} \tag{42}$$

The comparison is done on the estimated current densities on the four calorimeter panels, that are proportional to the deposited power since the power may also be written as:

$$P = IU_{\mathrm{HV}} = jAU_{\mathrm{HV}} \tag{43}$$

where U_{HV} is the total voltage, A the area of the grid apertures and j the current density, under the assumptions that all the power is carried by particles at full energy and that the current density is flat across the apertures and uniform in the various apertures.

Since it is not straightforward to determine from which part of the grids the particles impinging on each panel come from, the area A used for calculation is the total extraction area (985 cm^2) and what is determined is an estimate of the portion of the accelerated current density which impinges on each of the panels.

As it may be seen in Figure 46, the results of the two determinations of the current densities are correlated, and the slope of the straight lines that best fits the data is in the previuosly defined range for 3 panels out of 4: only panel 1 gives a slope below 0.90.

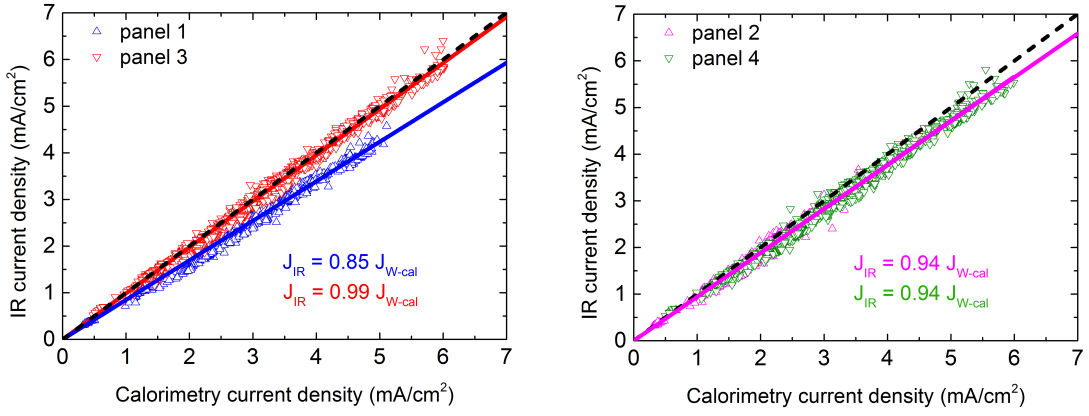

Figure 46: Current densities on the four panels: IR thermography vs water calorimetry. Left: Panels 1 and 3. Right: Panels 2 and 4.The black dashed lines represent the bisector of the first quadrant.

The temperature measured by the camera depends only on the measured radiance, the setting parameters and the chosen emissivity. Since settings are kept fixed, this result

allows to conclude that the chosen emissivity is suitable for meaningful power evaluation. It is also possible to find a reasonable explanation for the different slopes which are found in the four panels.

Since in principle the IR measurement is identical in the four panels, the reason for this could be found in the water calorimetry. For example the water flows cooling each of the four panels are not measured, but they are simply assumed to be all equal to 1/4 of the total water flow.

Because of the beam downward deflection due to the magnetic filter field, a larger power is expected on the lower panels. This result is found by both diagnostics (Figure 47). Looking at the percentages of the total current impinging on the four panels, water calorimetry provides equal power on the two lower panels and a difference around 20% for the two upper ones, whereas thermography reduces this difference to 10%, as shown in Figure 47, indicating a more homogeneous beam.

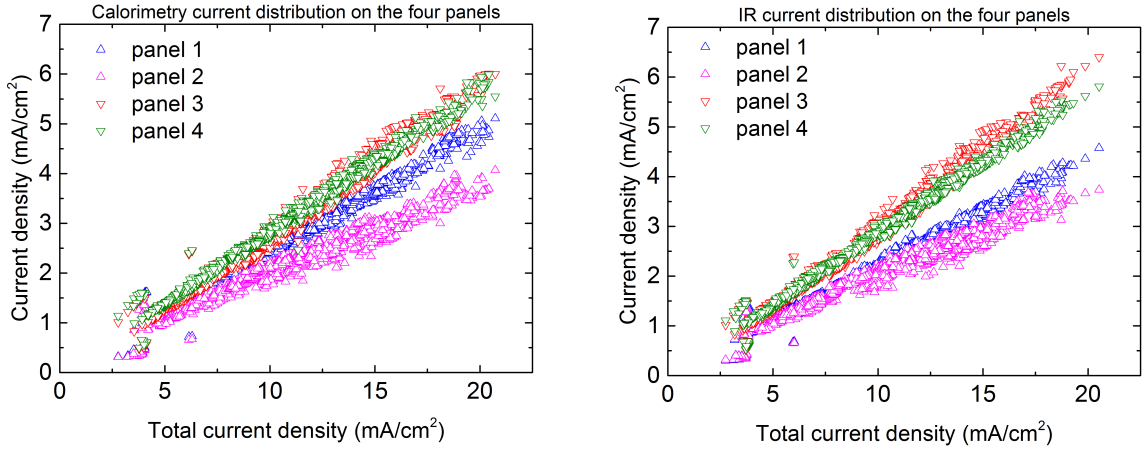

Figure 47: Current on the four panels with respect to the total. Left: water calorimetry. Right: IR thermography.

In conclusion, an emissivity value $\epsilon = 0.83$ can be considered a good average in time (days and months) and space (the calorimeter surface) for the analysis performed in this thesis.

5 IR data analysis

The main objective of the data analysis presented in this thesis is to provide a characterisation of the beam of the ELISE test facility. In particular, beamlet divergence and beam homogeneity will be determined from the IR image of the calorimeter. The divergence of the single beamlets cannot be derived directly from the IR image, because at 3.5 m from the grounded grid, for the typical divergences measured at ELISE (larger than 1°) beamlets are not distinguishable. However, the widening of the beamlets is correlated with a measurable widening of the beamlet groups.

Also the definition of homogeneity given in section 1.3 has to be adapted for the same reason. A reasonable approach is to apply the definition to the beamlet groups considering homogeneous a beam in which the current (and so the power) associated to each beamlet group does not differ more than 10 % from the average of all the beamlet group currents (or powers).

5.1 Fit of the power density profile

The power density profiles obtained with the IR camera are fitted via eight Gaussian sub-beams, one for each beamlet group. This fit should provide the main features of the beam such as its divergence and homogeneity.

The number of free parameters was set to 14: 8 amplitudes $A_1,\dots A_8$, 4 widths $\sigma_{\mathrm{x_{top}}}$, $\sigma_{\mathrm{x_{low}}}$, $\sigma_{\mathrm{y_{top}}}$, $\sigma_{\mathrm{y_{low}}}$, and 2 vertical positions y_{top} and y_{low}, one for each row of beamlet groups.

This number of free parameters results from a compromise between the fit capability of reproducing the data (χ^2 minimization) and the physical meaning of the fit itself. Fits in which all widths and positions were left free for example, gave non-meaningful results in many cases, such as very different deflections, amplitudes or widths for beamlet groups in the same row, due to the partial superposition of the beamlet groups. The choice of a Gaussian to fit the beamlet group shape is also a compromise. At the plasma grid the beamlet groups have a rectangular shape, with a height that is about three times their width. Since the beam is divergent a more elliptical shape is found after 3.5 m, and the sizes of the two axes get more similar for larger divergences. If divergence is not too low (below 0.8°), which seldom is the case for ELISE pulses, the data can be fitted satisfactorily using Gaussian.

The positions of the centers in the horizontal direction are assumed to be the projection of the beamlet group centers, whereas those in the vertical one, y_{top} and y_{low}, are left free, since a vertical shift due to the magnetic filter field always occur. Amplitudes can describe beam homogeneity and widths can be correlated with divergence, this is the reason why different widths between the upper and lower part are assumed as a possibility. So, letting $u(x, y)$ be the power density on the calorimeter, it could be written as:

$$u(x,y) = \sum_{i=1}^{4} A_i \exp[-\frac{(x-x_i)^2}{2\sigma_{x_{\mathrm{top}}}^2} - \frac{(y-y_{\mathrm{top}})^2}{2\sigma_{y_{\mathrm{top}}}^2}] + \sum_{i=5}^{8} A_i \exp[-\frac{(x-x_i)^2}{2\sigma_{x_{\mathrm{low}}}^2} - \frac{(y-y_{\mathrm{low}})^2}{2\sigma_{y_{\mathrm{low}}}^2}] \quad (44)$$

The index numbering the Gaussians grows from left to right and from top to bottom, so that $i = 1$ refers to the upper-left and $i = 8$ to the lower-right, according to the convention introduced in section 3.2.1 (see Figure 21).

In order to check the general applicability of this fit, two examples for different divergences are given in the following. Some of the beam parameters for the two pulses, together with the fit results, are listed in Table 5.

The fit result for a pulse with large divergence ($div_{19} = 3.25°$), in which not even the beamlet groups are distinguishable, is displayed in Figure 48.

The residuals, shown in Figure 48(c), are calculated as the difference between the data and the fitting function. It has to be noted that residuals are very large in the calorimeter vertices on the left side of the image. The reason for this is the limit to the camera field of view given by the port in which it is placed, already discussed in section 3.2.1. These points have been neglected in the fitting procedure and, excluding them, residuals are below 5 %, meaning that the fit describes quite well the data and can be considered satisfactory.

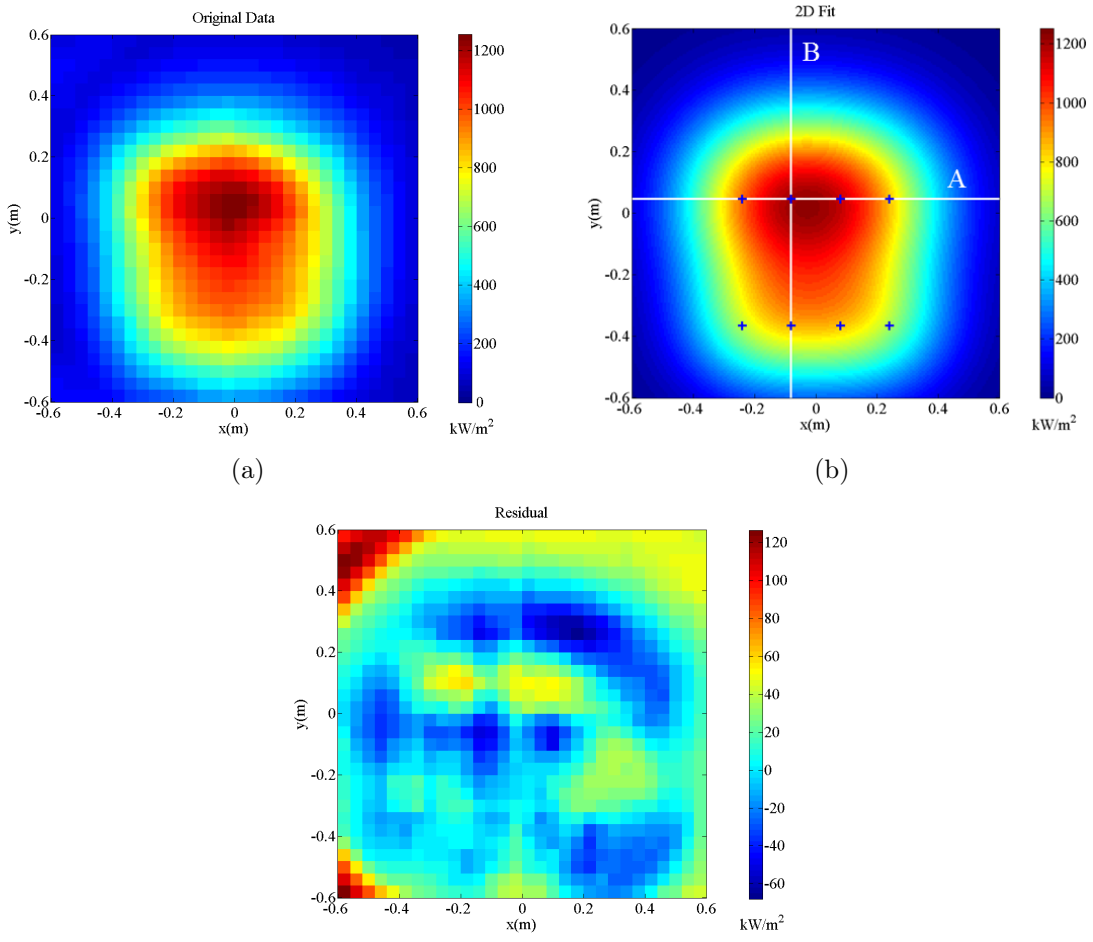

Figure 48: Fit of the power density 2D profile of ELISE pulse #5938, divergence $div_{19} = 3.25°$. a) Raw data with 30 × 30 blocks resolution from the calorimeter. b) Fit results. Blue crosses represents the Gaussian centers. 1D profiles are extracted along the white lines. c) Residuals calculated as the difference between the original data and the fit.

For comparison the 1D profiles of power density along vertical and horizontal lines are shown in Figures 49. The horizontal line goes through the beamlet group centers of the upper row, the vertical one through the centers of groups #2 and #6: these lines are drawn in white in Figure 48(b). The data and the fit of the 2D power density profile for a pulse with small divergence ($div_{19} = 1.17°$) are displayed in Figure 50.

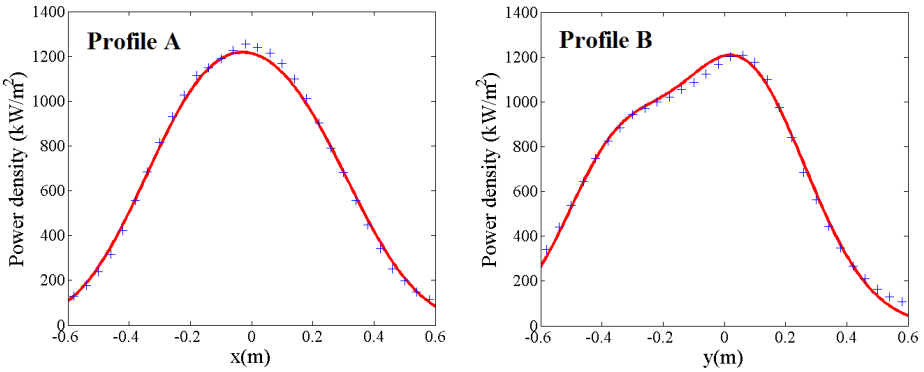

Figure 49: 1D profiles of power density for ELISE pulse #5938. The blue crosses give the camera measurement, the red curve is the fit. Left: horizontal profile (along line A of Figure 48(b)). Right: vertical profile (along line B of Figure 48(b)).

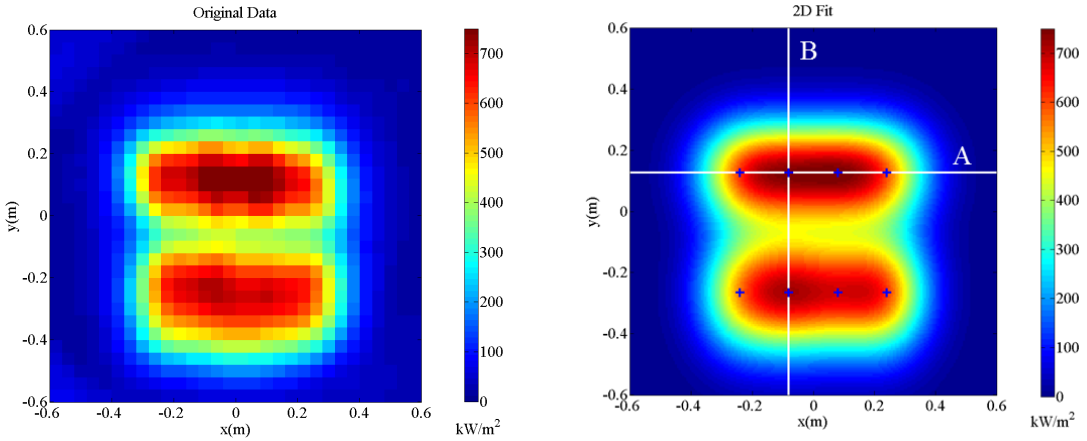

(a) (b)

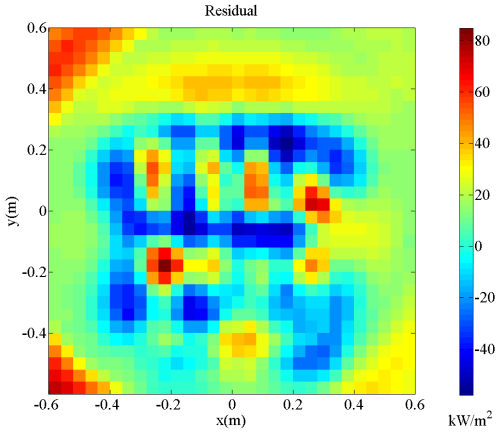

(c)

Figure 50: Fit of the power density 2D profile of ELISE pulse #6308, divergence $\mathrm{div}_{19} = 1.17°$. a) Raw data with 30 × 30 blocks resolution from the calorimeter. b) Fit results. Blue crosses represents the Gaussian centers. 1D profiles are extracted along the white lines. c) Residuals calculated as the difference between the original data and the fit.

In this case the residuals are up to 10 %, but the fit can still be considered satisfactory. These higher residuals with respect to the pulse with larger divergence are reasonable, since for low divergence the shape of the beamlet groups is more rectangular and therefore more difficult to fit with Gaussians. In general the uncertainty which is found on the fit parameters is below 5 %. The 1D profiles of power density along vertical and horizontal lines are shown in Figures 49.

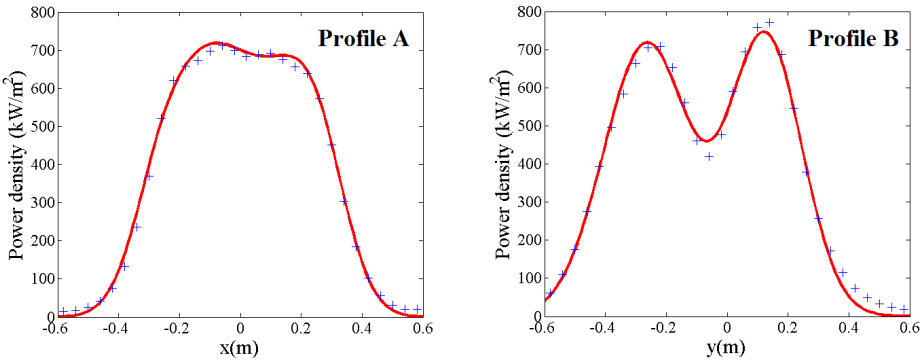

Figure 51: 1D profiles of power density for ELISE pulse #6308. The blue crosses give the camera measurement, the red curve is the fit. Left: horizontal profile (along line A of Figure 48(b)). Right: vertical profile (along line B of Figure 48(b)).

Parameters	**Pulse #5938**	**Pulse #6308**
divergence on Los #19	3.25°	1.17°
Normalised perveance Π/Π_0	0.154	0.266
Extraction voltage	9.2 kV	4.6 kV
Acceleration voltage	30.3 kV	25.0 kV
Extracted current	19.8 A	12.1 A
Fit parameters	**Pulse #5938**	**Pulse #6308**
y_{top}	(5.8±0.2) cm	(12.6±0.2) cm
y_{low}	(-35.2±0.3) cm	(-26.5±0.2) cm
A_1	(463±17) kW/m^2	(456±8) kW/m^2
A_2	(365±24) kW/m^2	(418±10) kW/m^2
A_3	(400±24) kW/m^2	(447±10) kW/m^2
A_4	(325±15) kW/m^2	(425±8) kW/m^2
A_5	(380±11) kW/m^2	(418±8) kW/m^2
A_6	(287±18) kW/m^2	(480±9) kW/m^2
A_7	(266±18) kW/m^2	(402±10) kW/m^2
A_8	(379±11) kW/m^2	(493±7) kW/m^2
$\sigma_{\text{x}}^{\text{top}}$	(19.8±0.3) cm	(10.9±0.2) cm
$\sigma_{\text{x}}^{\text{low}}$	(17.4±0.2) cm	(10.1±0.2) cm
$\sigma_{\text{y}}^{\text{top}}$	(19.9±0.2) cm	(11.9±0.2) cm
$\sigma_{\text{y}}^{\text{low}}$	(19.7±0.2) cm	(14.0±0.2) cm

Table 5: Main parameters of pulses #5938 and #6308.

5.2 Beam simulation

In order to find a relation between the beamlet divergence and the widths of the beamlet groups on the calorimeter surface, some simulations have been performed in IDL.

The beam power was simulated as the superposition of 640 Gaussians, one for each beamlet, reproducing the geometry of the grids. It has to be noted that the performed simulations are not simulation of the source processes or of the beam optics, but simply provide the expected 2D power profile for given power and divergence, upon assuming that the divergence remains constant along the beamlet path. For these reasons for example, no vertical shift is observed in the Figures of this section and the Gaussian centers are always found in the position of the projections of the beamlet group centers on the calorimeter.

Fixing the power of each beamlet, their divergence was changed in order to obtain a relation between the beamlet divergence and the widths of the fitting Gaussians. All the beamlets are considered to have the same power and the same divergence, i.e. the beam is assumed to be homogeneous.

By fitting the resulting power profile on the calorimeter surface it is possible to determine the widths of the fitting Gaussians as function of the beamlet divergence. Before fitting the resulting 2D power profile at the calorimeter distance, the image has been divided in 30×30 blocks and, in order to reproduce the experimental spatial resolution, an average was calculated in each of them, so that the procedure applied to the data from simulation is the same as for the camera data.

For very low divergence, the fit does not make sense since in the 2D power profile rectangular shapes are still visible and fitting with Gaussian fails, but for divergences larger than 1°, the fit works fine, giving residuals below 10 %, which decrease for increasing divergence.

Figure 52 shows the fit result for a simulated beam in which the beamlet divergence was set to $\delta = 1.4°$, while Figure 53 gives, for the same divergence, the 1D profiles along the horizontal line passing through the centers of the beamlet groups in the upper row, and along the vertical line passing through the centers of groups #2 and #6 (the same profiles used in section 5.1).

The fit can be considered satisfactory since it gives the main features of the beam in terms of shape and power (amplitude). However, the band structure of the residuals (see Figure 52(c)) evindences some limits of the used fit. These limits can be more easily understood from Figure 53, where it can be seen that in the horizontal profile, the fitting curve is always above the data, and in the vertical one, the two profiles cross each other many times.

This effect is strongly reduced for larger divergence, confirming that the fit capability of reproducing the 2D map of the power density deposited by the beam increases with the beam divergence. An example is given in Figures 54 and 55, both referring to a pulse in which the beamlet divergence was set to $\delta = 2.8°$. For this divergence, the residuals have still a band structure in the vertical direction, meaning that the two profiles cross each other many times, but their magnitude is much lower (few %). The improvement of the fit result is even more clear by looking at the 1D profiles (Figure 53) which are almost perfectly superimposed.

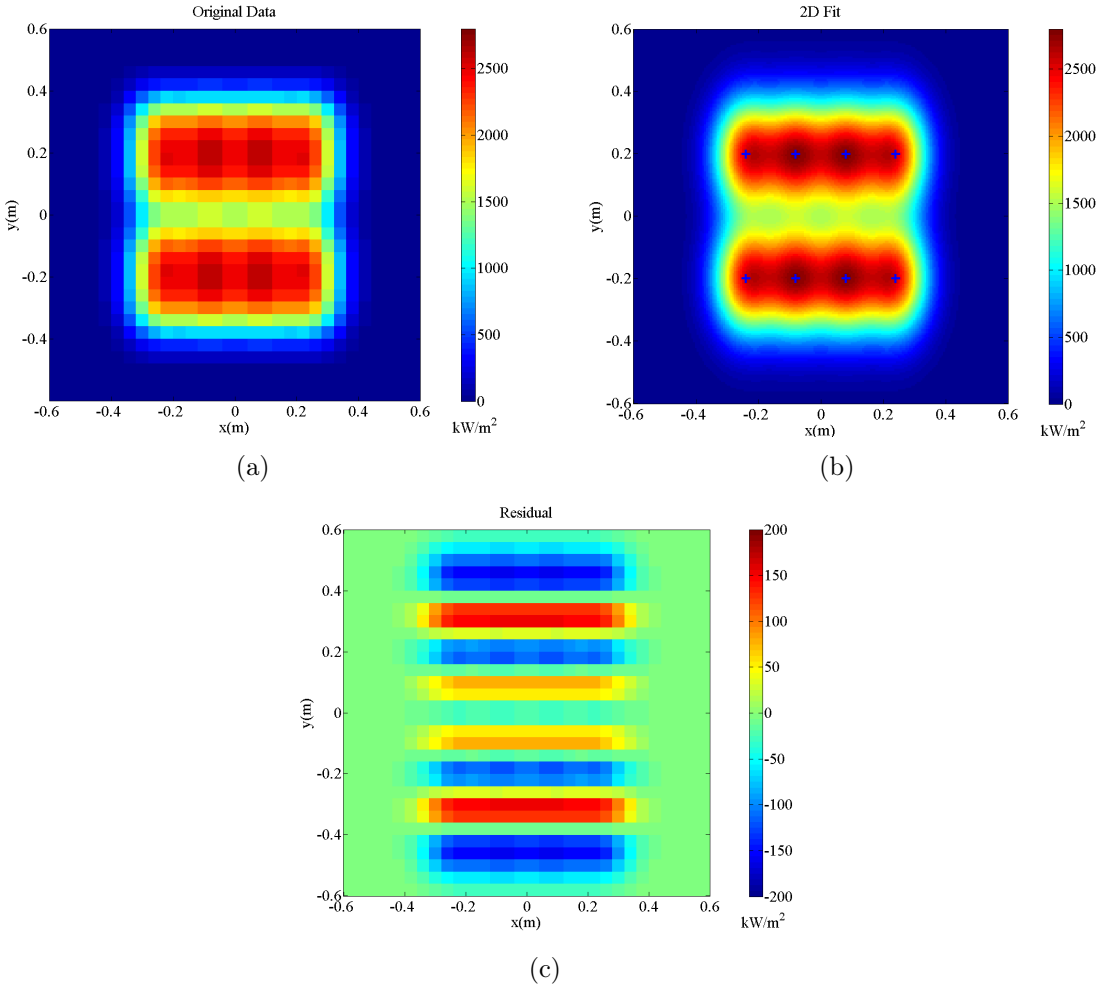

Figure 52: Fit of the beam simulated power density 2D profile on the calorimeter surface for a beamlet divergence $\delta = 1.4°$. a) Data from simulation with 30×30 blocks resolution of the calorimeter. b) Fit results. Blue crosses represents the Gaussian centers. c) Residuals calculated as the difference between the data from simulation and the fit.

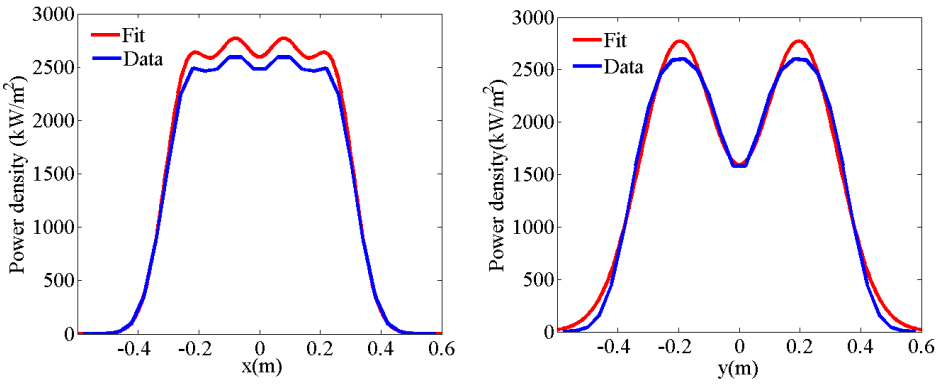

Figure 53: Power density 1D profile for a beamlet divergence $\delta = 1.4°$. Left: horizontal profile. Right: vertical profile. The blue curve represent the simulated data, the red one gives the profile resulting from the fit.

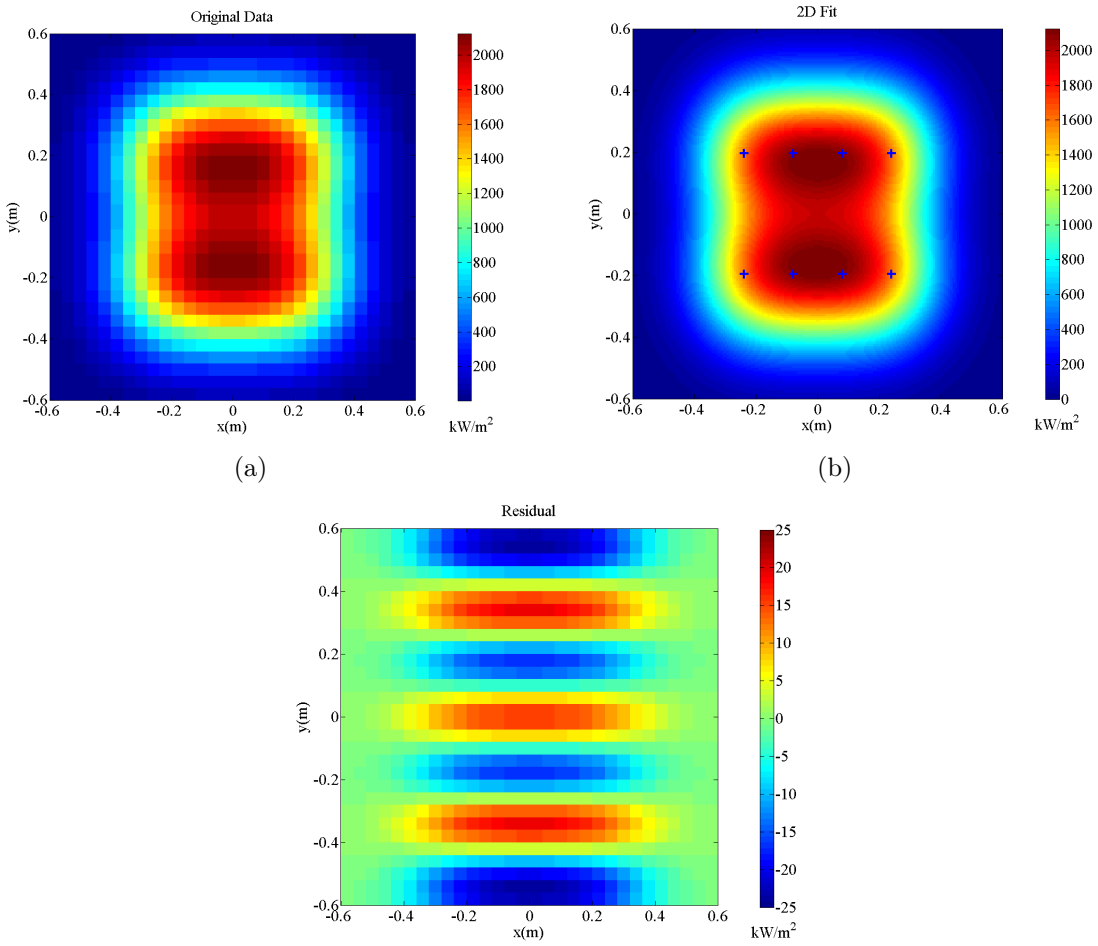

Figure 54: Fit of the beam simulated power density 2D profile on the calorimeter surface for a beamlet divergence $\delta = 2.8°$. a) Data from simulation with 30×30 blocks resolution of the calorimeter. b) Fit results. Blue crosses represents the gaussian centers. c) Residuals calculated as the difference between the data from simulation and the fit.

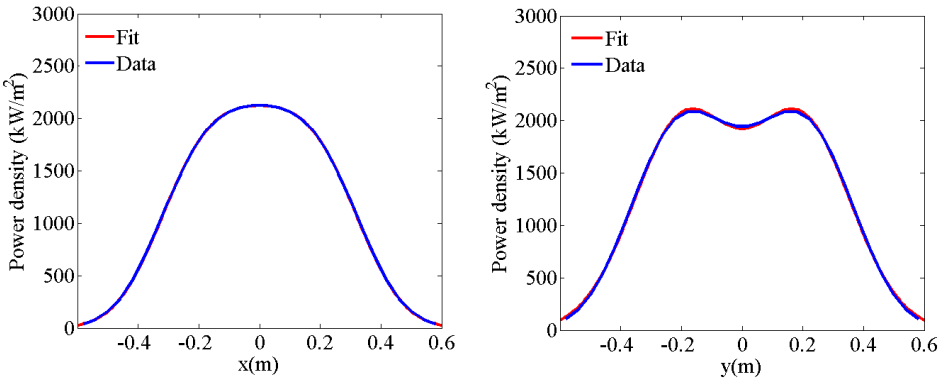

Figure 55: Power density 1D profiles for a beamlet divergence $\delta = 2.8°$. Left: horizontal profile. Right: vertical profile. The blue curve represent the simulated data, the red one gives the profile resulting from the fit.

The trend of Gaussian widths with the beamlet divergence obtained from the described simulations is displayed in Figure 56. Since the beamlet group has an intrinsic width given by the aperture disposition in the grids, a saturation of the widths for low divergence is expected. This kind of saturation can be seen for σ_y. The saturation value is about 10 cm, corresponding to a half 1/e width of 14 cm, which compared to the initial beamlet group half width of 16 cm (8 beamlet $\times$ 20 mm) is a reasonable result. The saturation of the horizontal width is expected to occur at a value in the order of $\sigma_x = 3.5$ cm since the initial half width of the beamlet group in the horizontal direction is about 5 cm. This saturation cannot be seen in the picture and could probably occur for smaller divergence. These curves may be used to derive divergence from the Gaussian widths obtained by fitting the experimental data, as it will be done in section 6. For doing so, σ_x will be described by a straight line and σ_y by a parabola (displayed in Figure 56) since these function reproduce best the data in the divergence interval that will be considered in the following (1.5° - 4.5°).

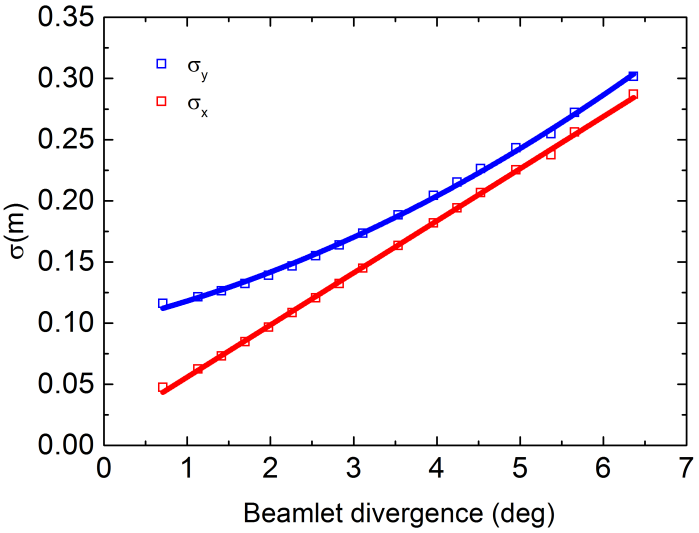

Figure 56: Results of simulations performed in IDL: Widths of the Gaussians used for fitting the beamlet groups vs beamlet divergence.

6 Beam shift and divergence

In chapter 5 the capability of a fit based on eight Gaussians (one for each beamlet group) to reproduce the data from the IR camera was verified. Additionally, the scaling of the fit parameters with beamlet divergence when applied to simulated data, in which no aspect of the ion source but the grid geometry is taken into account, were checked. In this chapter also the dependence of the fit parameters from the source parameters, such as the perveance or the plasma grid current (i.e strength of the magnetic field) will be tested. In particular it is expected that the current flowing through the plasma grid generates a vertical deflection of the beam.

The trend of the widths (σ_x and σ_y from the fit) with perveance is compared with the one of divergence, discussed in section 2.2 and shown in Figure 13. At ELISE the value of normalised perveance is seldom above the perveance optimum (between 0.15 and 0.25 for pulses in hydrogen): this means that in general, an increase of the perveance leads to a decrease of the divergence.

Moreover, to test the reliability of the IR data analysis, the results about the beamlet divergence will be compared with the ones from the BES. In the following when comparing with BES, LoS #3 will be used for the lower part and LoS #11 for the upper part. Their positions are y_3 = -27.5 cm and y_{11} = 12.5 cm, both 7.5 cm below the projection of the beamlet group centers. For this reason they are the most suitable to be used for comparison, since the average downward shift of the beam on the calorimeter surface is about 6-8 cm (see below). The divergence measured on the vertical LoS are very similar. In the following, one of the two central LoS, #19, will be used as vertical LoS.

6.1 Benchmark tests and comparison with the BES

This analysis can be divided in three parts. First tests have been done on pulses in which only one of the two generators was used, i.e. the plasma was generated either in the two upper or the two lower drivers only. In this case there is only "half" of the beam, so only superposition in the horizontal direction occurs. The results of this analysis are shown in section 6.1.1. Then, for pulses with both generators, statistical analysis has been performed. In this part, hydrogen and deuterium will be analysed separately because they have different optics since, as discussed in section 2.2, the normalised perveance in deuterium, for the same current, extraction voltage and geometry, is larger by a factor $\sqrt{m_D/m_H} = \sqrt{2}$. Results in hydrogen are summarised in section 6.1.2 while results in deuterium are in section 6.1.3.

The vertical deflection of the beam due to the magnetic field induced by the PG current will be discussed in section 6.2.

6.1.1 Scan with one generator

The investigated groups of pulses are performed in deuterium and represent two scans in the extraction voltage U_{ex}. The other parameters were not changed and are listed in Table 6.

The trends of the beamlet group widths with respect to divergence, measured by BES, and normalised perveance are shown in Figures 57 and 58 respectively. The widths σ_x and σ_y increase with increasing divergence (Figure 57) and their trend over the perveance reproduces the one of divergence itself (discussed in section 2.2).

Parameter	Value
Isotope	Deuterium
Acceleration voltage	25.1 kV
RF power	85 kW
PG current	3.3 kA
Source pressure	0.3 Pa

Table 6: Source parameters in the U_{ex} scans with only the upper or lower drivers.

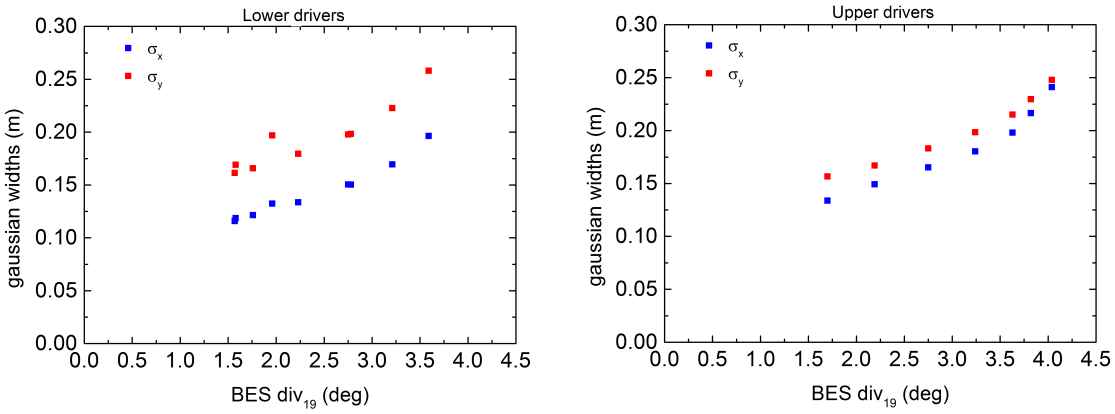

Figure 57: Beamlet group widths vs divergence measured by BES on LoS #19. Left: Plasma generation in the lower drivers only. Right: Plasma generation in the upper drivers only. The main parameters of these pulses are given in Table 6.

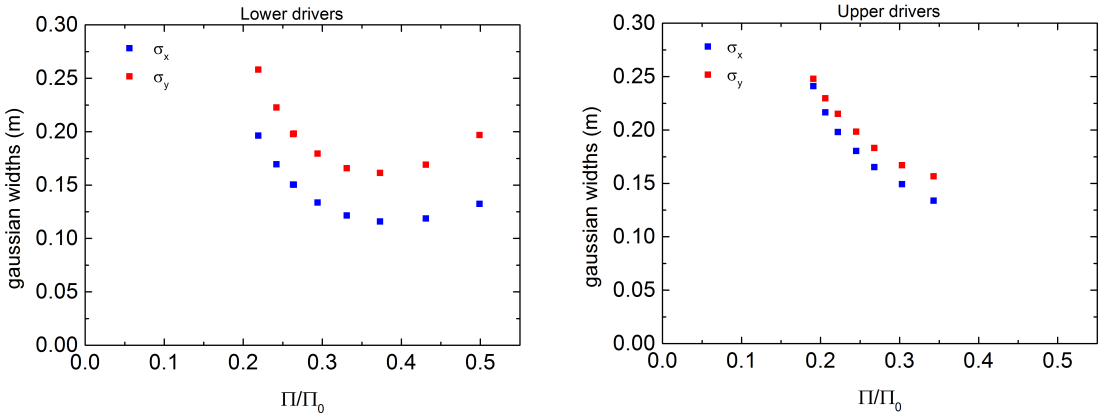

Figure 58: Beamlet group widths vs normalised perveance. Left: Plasma generation in the lower drivers only. Right: Plasma generation in the upper drivers only. The main parameters of these pulses are given in Table 6.

In particular, in the under-perveant region, the beamlet divergence should decrease for increasing perveance, while in the over-perveant region, an increase of perveance should lead to an increase of divergence. In the pulses in which only the lower drivers were used (see the left side of Figure 58), the perveance optimum is found around $\Pi/\Pi_0 = 0.35$, that is reasonable for deuterium since $0.35/\sqrt{2} \sim 0.25$, which is the above-mentioned value

for hydrogen. Moreover, in this group of pulses, perveances higher than the optimum are achieved and the expected inversion in the trend (an increase of divergence for increasing perveance after the optimum) can also be seen. In the group of pulses in which only the upper drivers were used, the normalised perveance does not exceed 0.35, so it is reasonable that no inversion is seen.

6.1.2 Hydrogen pulses

This section describes the investigation of the trend of the beamlet group widths with respect to divergence (given by the BES) and perveance. To this purpose it is not necessary to introduce any particular filtering of the data. The idea is in fact to simply verify that larger divergences give larger widths. No particular selection was done on the database and thus a certain dispersion of the data is expected, as source conditioning (i.e the status of the caesiation) could be very different, leading to different performances (different currents) even with identical externally set source parameters.

The correlation of the widths with the divergence measured by BES, was analysed for the whole database, excluding the pulses in which the fit result had to be considered unreasonable (at very low or very high divergences).

If the beam is homogeneous it is reasonable to have a correlation between the beamlet group widths σ_x and σ_y in the upper part and those in the lower part. This correlation occurs for the horizontal width σ_x, but is instead quite poor for the vertical one σ_y (see Figure 59).

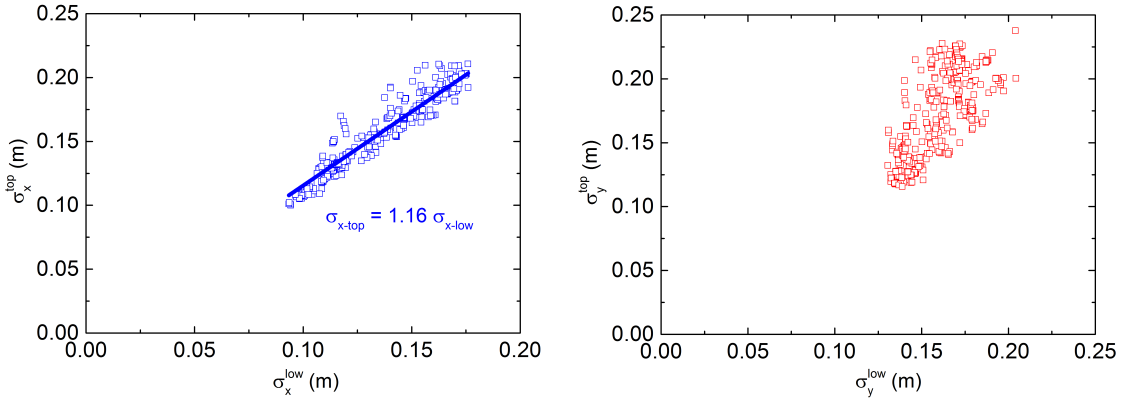

Figure 59: Beamlet group widths determined by applying a fit to the results of the IR camera. Upper half vs lower half. Left: horizontal widths. Right: vertical widths.

Focusing the attention on σ_y and on why the correlation is not so good, it is found that the vertical width in the upper half has a good correlation with perveance, whereas in the lower half it gives really broad data (see Figure 60). This behaviour could reflect some beam properties difference between the upper and lower grids or plasma behaviour in the source or could mean that σ_y^{low} is the parameter to which the fit is less sensitive. At present, no explanation was found.

As concerns the horizontal direction, it is possible to find a good correlation with divergence (almost linear) and perveance, as shown in Figure 61. In general it seems that in the two halves of the beam (upper and lower groups) the relation with divergence is slightly different, since the two data series have a poor overlap.

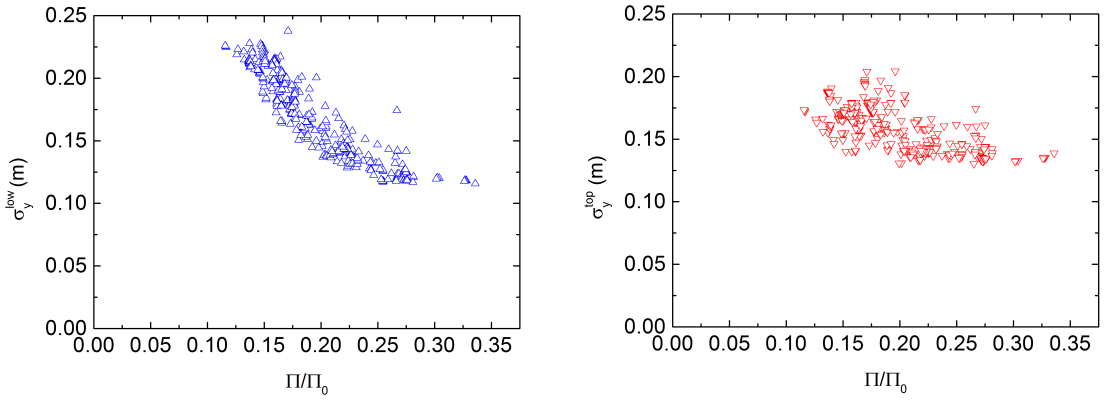

Figure 60: Beamlet group widths in the vertical direction σ_y vs normalised perveance. Left: Upper half. Right: Lower half.

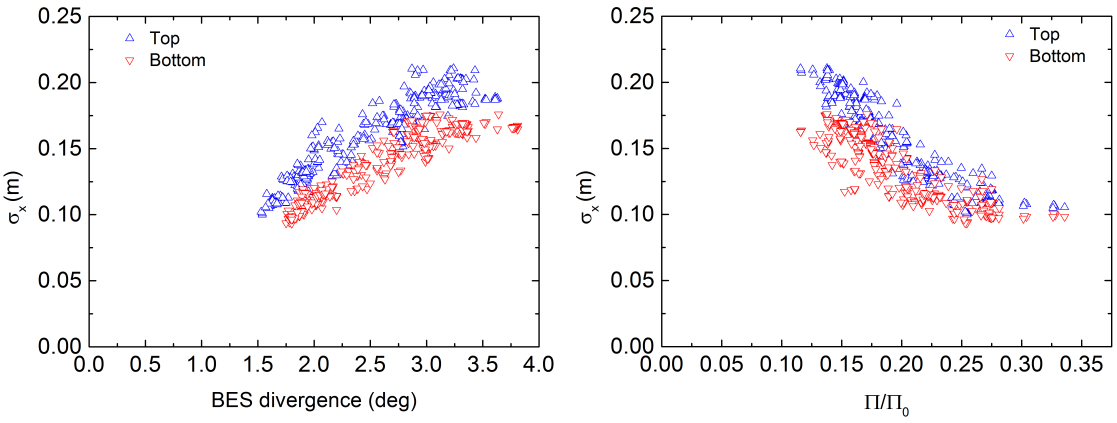

Figure 61: Beamlet group widths in horizontal direction σ_x vs divergence (left) and perveance (right).

Finally the results from simulations discussed in section 5.2 were used to derive an estimate of divergence from the beamlet group widths, i.e from the calorimeter. In Figure 62, this estimate is directly compared with the BES.

What could be infered from Figure 62 is that the value of divergence given by the calorimeter is generally larger than the value obtained by BES. A possible explanation for this difference is that the pressure in the tank is not sufficient to achieve a full space charge compensation at a distance of 2 meters from the grounded grid i.e. where the BES LoS are placed. In this case the divergence of the beamlets would still be increasing between the BES LoS and the calorimeter, while the performed simulation assumed a constant divergence for propagating the beamlets from the grounded grid to the calorimeter surface. This hypothesis could be confirmed by the preliminary results of studies on SCC that are currently run at the BATMAN test facility [49], where the tank pressure is of the same order of magnitude as the source filling pressure at ELISE. Moreover, this hypothesis could be verified in the future by applying a fitting procedure similar to the one used for the diagnostic calorimeter to the 2D profile of the intensity radiated by the W-wire calorimeter (once it will be absolutely calibrated), which is closer to the BES (1.8 meters downstream

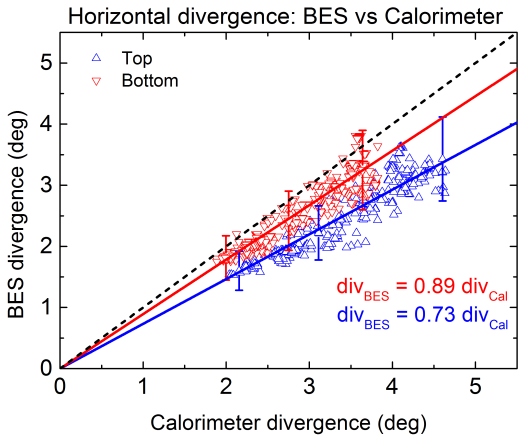

Figure 62: Result of divergence estimate in horizontal direction for pulses in hydrogen : BES vs calorimeter. The errorbars are shown only on some data points. The black dashed line represents the bisector of the first quadrant.

the grounded grid). From the resulting widths it would be possible, in the same way that was used for the diagnostic calorimeter to derive a divergence estimate.

6.1.3 Deuterium pulses

The same analysis presented in section 6.1.2 for pulses in hydrogen was performed also for pulses in deuterium. In deuterium also the widths σ_y have shown a good correlation in the upper and lower part as displayed in Figure 63, differently from what was found for hydrogen.

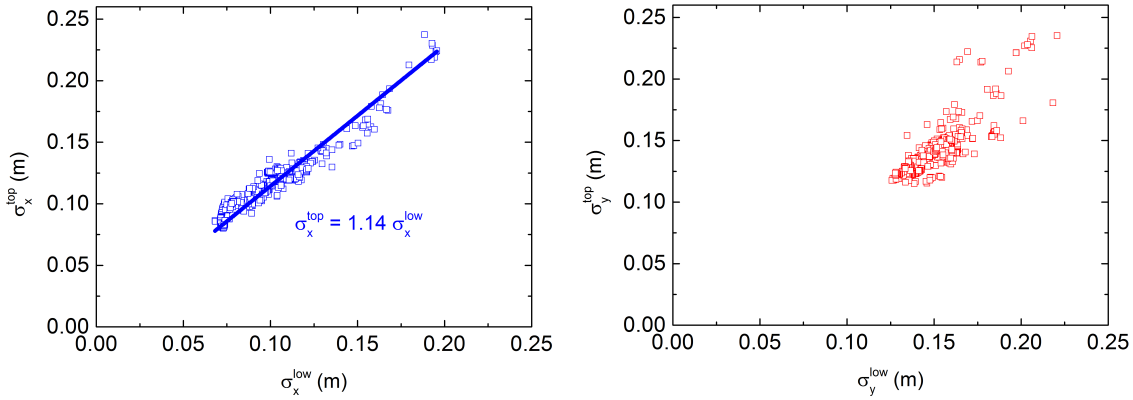

Figure 63: Beamlet group widths. Upper half vs lower half. Left: horizontal width. Right: vertical width.

The trends of the Gaussian horizontal widths with respect to perveance and divergence are shown in Figure 64. Even in this case, the results for the two isotopes are quite similar. In particular, the expected difference in the perveance optimum cannot be clearly seen by comparing this Figure to Figure 61 due to the fact that both curves (for H and D) have a very broad minimum.

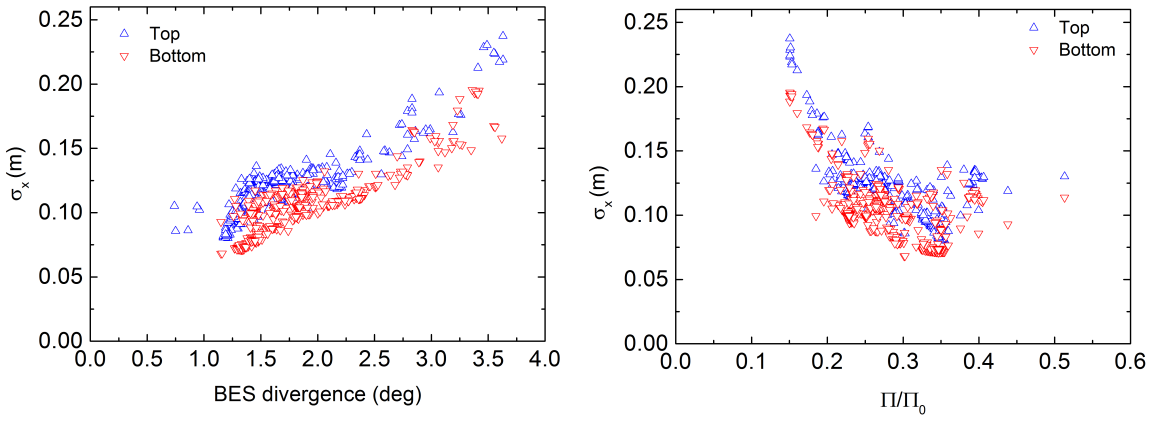

Figure 64: Beamlet group widths in horizontal direction vs perveance (left) and divergence (right).

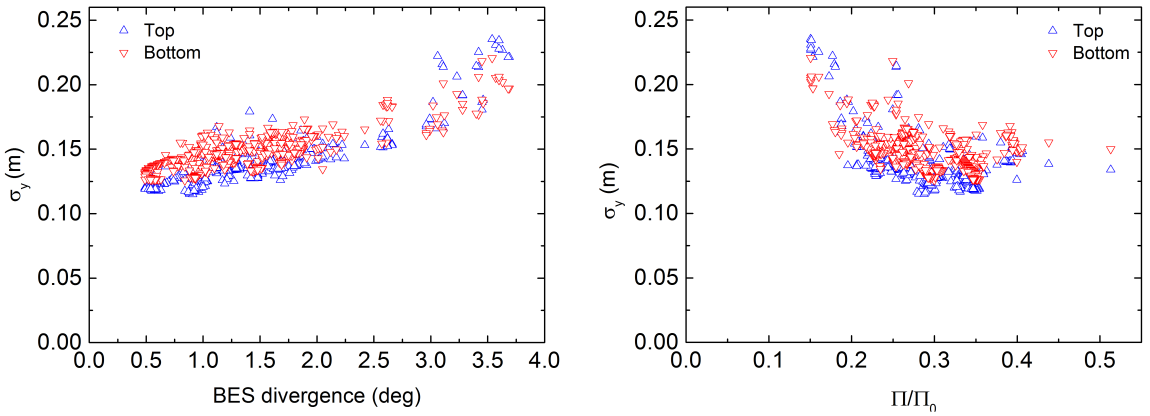

Figure 65: Beamlet group widths in vertical direction vs perveance (left) and divergence (right).

Finally the same comparison between BES and calorimeter evaluation of divergence that was performed for hydrogen, was done also for deuterium pulses, as shown in Figure 66.

The value of the lines angular coefficient for deuterium are just a bit smaller than those found for hydrogen in the previous section, confirming that the estimate of the divergence obtained by the calorimeter is larger then the divergence measured by BES.

6.2 Beam vertical deflection

The vertical deflection of the beam at the calorimeter distance from the grids may be determined as the simple difference between the position of the projection of the beamlet group centers and the position, y_{top} for the upper row and y_{low} for the lower one, which is obtained by the fit applied to the 2D map of power density. The vertical shift of the beam is expected to depend mainly on the magnetic field (i.e on the PG current) and on the particle velocity (i.e on the applied total voltage). Since the strength of the magnetic field decreases with increasing distance from the plasma grid, the extraction voltage has a larger influence than the acceleration voltage.

The typical value used for the PG current in hydrogen is around 2 kA. This is used in most of the pulses, except when a PG current scan is performed.

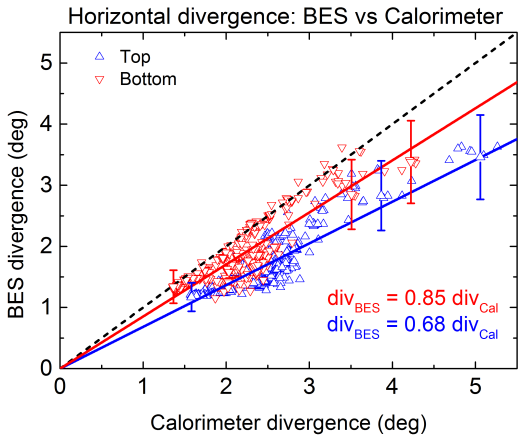

Figure 66: Divergence measurement in horizontal direction for pulses in deuterium: BES vs calorimeter. The errorbars are shown only on some points. The black dashed line represents the bisector of the first quadrant.

The left side of Figure 67 shows the trend of the beam vertical shift with respect to the PG current inside a scan. The main source parameters of this scan are listed in Table 7. As expected, the shift of the beam increases with the PG current, but it has to be noted that the shift is different in the two halves. Changing the PG current is more effective on the deflection of the bottom row of beamlet groups. By doubling the PG current in fact, also the shift is almost doubled, whereas for the upper row the dependence is definitely weaker. This difference, which is unexpected since the magnetic field lines at the aperture should be exactly symmetric, has been confirmed by the thermocouples. For the same pulses, comparing the TC results along vertical lines for the two extremes of the scan (in which the PG current changes by a factor of 2) the lower part of the beam is confirmed to have a larger position variation, as can be seen in the right-hand side of Figure 67.

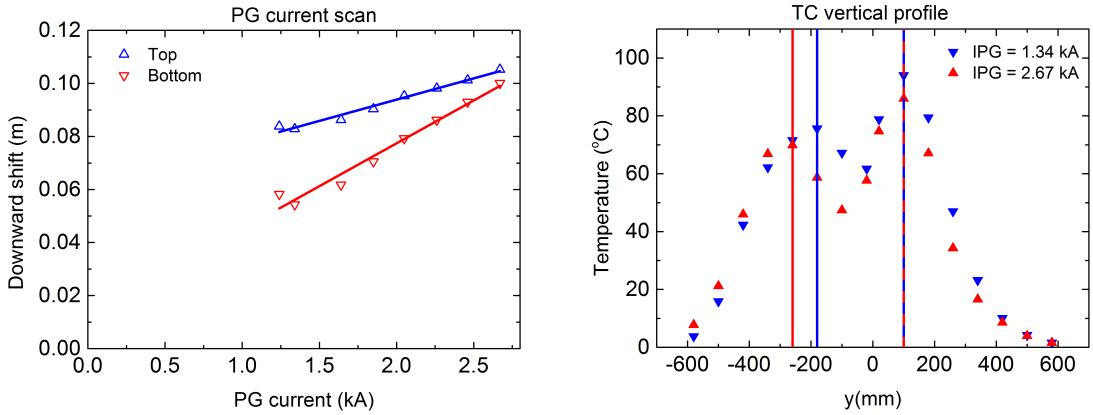

Figure 67: Left: Downward shift determined by the fit to the IR data vs PG current. Right: Temperature profiles along the left vertical TC line for the two extremes of the PG current scan $I_{min} = 1.34$ kA (in blue) and $I_{max} = 2.67$ kA (in red). The vertical solid lines give the position of the maxima of the temperature profile.

The reason for this unexpected difference in the shift of the two halves is still under investigation.

Parameter	Value
Isotope	Hydrogen
Extraction voltage	5.4 kV
Acceleration voltage	32.1 kV
RF power	125 kW
Source pressure	0.35 Pa

Table 7: Main source parameters in the PG scan.

The analysis performed in this thesis allows to correlate the vertical shift of the beam also with perveance, as shown in Figure 68, when the PG current is kept fixed.

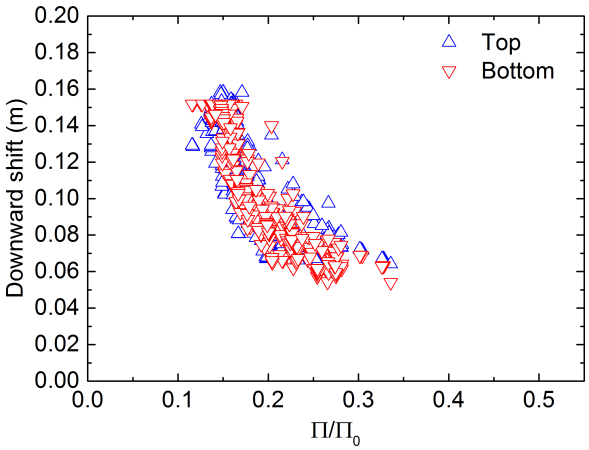

Figure 68: Downward shift of the beam evaluated by the IR camera data vs normalised perveance (at fixed magnetic filter field) for pulses in hydrogen. The two data series represent the upper and lower row of beamlet groups.

This result, which is definitely unexpected, has been confirmed also in deuterium as displayed in Figure 69.

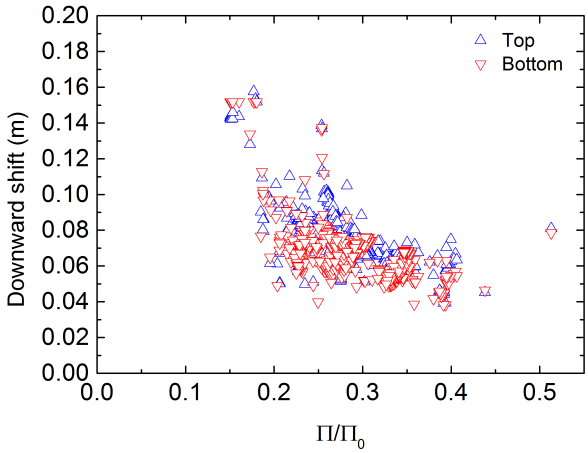

Figure 69: Downward shift of the beam evaluated by the IR camera data vs normalised perveance (at fixed magnetic filter field) for pulses in deuterium. The two data series represent the upper and lower row of beamlet groups.

From these results it can be infered that the deflection decreases with increasing Π. A possible explanation for this phenomenon is as follows: below the perveance optimum, that is generally the case at ELISE (see Figure 61), if perveance is low, than the beamlet divergence is higher and the beamlet is wider. This means that when the beamlet goes through the PG aperture, a higher percentage of current is localised in the external region of the aperture itself. Since the filter field is generated by the current flowing through the PG, a wider beamlet is closer to the inducing current and therefore experiences a higher magnetic field. So this macroscopic effect on the beam trajectory could be explained by local variations of the magnetic field intensity.

Finally the discussed correlation between the downward shift and the perveance was verified also restricting the analysis to the pulses in which very high currents were achieved (I>20 A in hydrogen), since Cs conditioning is better and these are the source relevant conditions (see Figure 70).

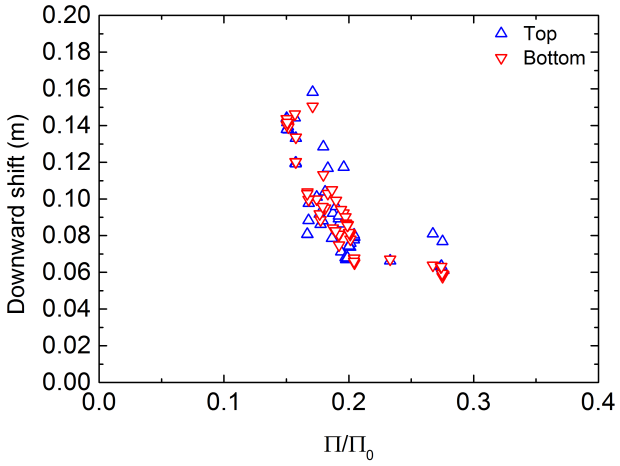

Figure 70: Downward shift of the beam evaluated by the IR camera data vs normalised perveance (at fixed magnetic filter field) for pulses in hydrogen with currents larger than 20 A. The two data series represent the upper and lower row of beamlet groups.

7 Beam homogeneity

The objetive of this chapter is to assess the beam homogeneity. As mentioned in chapter 5, even for the lowest divergences achieved at ELISE, at the calorimeter distance from the grounded grid (3.5 m), the beamlets are not distinguishable. Therefore the definition of homogeneity based on beamlets (given in section 1.3) has to be adapted. A reasonable approach is to apply that definition to the beamlet groups: the maximum difference between the current (or power) in one beamlet group and the average of all the beamlet groups will be used as a measure of the beam inhomogeneity. The total power associated to each beamlet group may be evaluated by the volume of the fitting 2D Gaussian, which is given by $V = 2\pi A\sigma_x\sigma_y$.

It has to be considered that when divergence is large (around 3° and so of no interest for an ITER NBI) even the beamlet groups cannot be distinguished. Therefore, even the fit capability to distinguish a completely homogeneous beam, in which all the beamlet groups have the same amplitude, from an inhomogeneous one has to be investigated at large divergences.

From the simulation performed in section 5.2 (see Figure 56), σ_x turned out to be about 8 cm, i.e. half of the distance between two groups in the horizontal direction, for a divergence of 1.6 °(see Figure 56). This means that when divergence is 1.6°, two close Gaussians intersect each other when they are at about the 60 % of their maximum.

Since in most of the ELISE pulses the divergence is larger than 1.6°, the superposition could be too high to correctly determine the amplitudes from the fit. This aspect will be considered again in section 7.2.

7.1 Local inhomogeneity

Since all the beamlet groups of the upper and lower row, respectively, are fitted using the same widths, the homogeneity within a row is described by the ratio of the Gaussian amplitudes A_i to the row average amplitude $<A>_{top}$ or $<A>_{bottom}$.

Figures 71 show the amplitudes of beamlet groups #1, #2, #3 and #4 with respect to the average amplitude in the upper row $<A>_{top}$ for pulses in hydrogen.

The data are fitted well by straight lines and the statistical error given by the fit on the angular slopes is very low (1 %). Using these slopes of the fitting lines as an average amplitude ratio to apply the definition of inhomogeneity to the beamlet groups, a maximum inhomogeneity for the upper line of 13 % is obtained. By looking at the slopes, it could be seen that the difference between the amplitudes of groups #1 and #2 is, on average, equal to 20%.

The respective results for the lower half of the source are shown in Figure 72. Again large fluctuation (17 %) occurs, this time between groups #7 and #8. For the lower line inhomogeneity is 9 %.

The resulting trend of the Gaussian amplitudes along the two beamlet group rows are shown in Figure 73. It is interesting to note that there is no defined profile (for example larger amplitudes in the center or at the borders), but the amplitudes have some fluctuations from group to group which tend to compensate with the closer ones. This is clear in the upper line where A_1 and A_3 are generally larger than the average, while A_2 and A_4 are generally smaller.

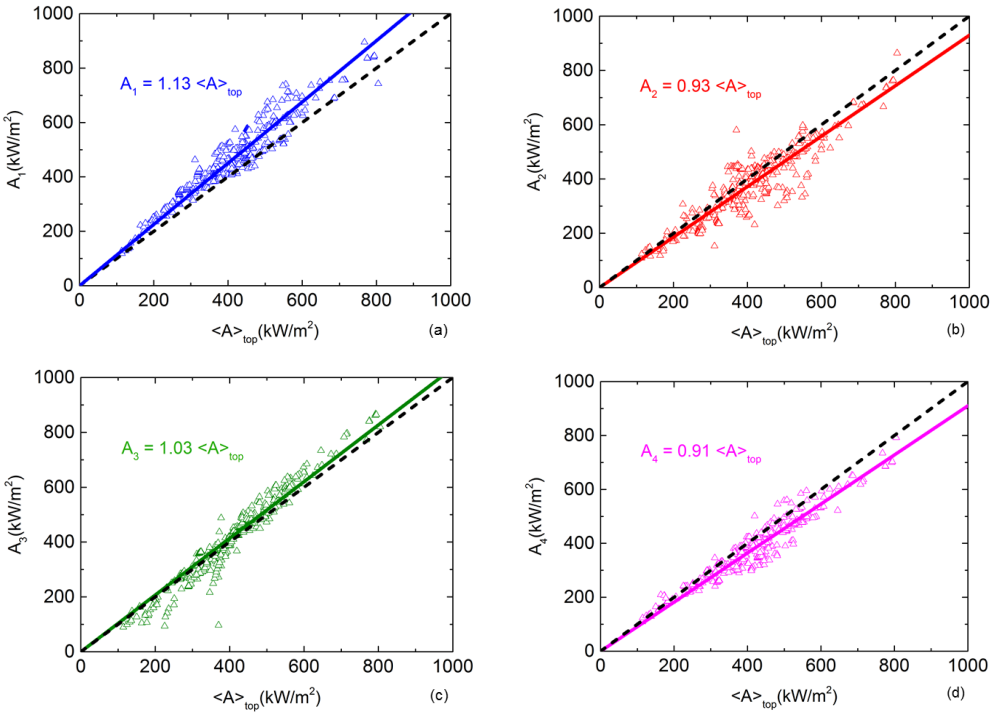

Figure 71: Amplitude of Gaussians fitting groups #1, #2, #3 and #4 vs average amplitude in the upper row for pulses in hydrogen. The solid lines give a fit to the data points (the open symbols). The black dashed lines represent the bisector of the first quadrant.

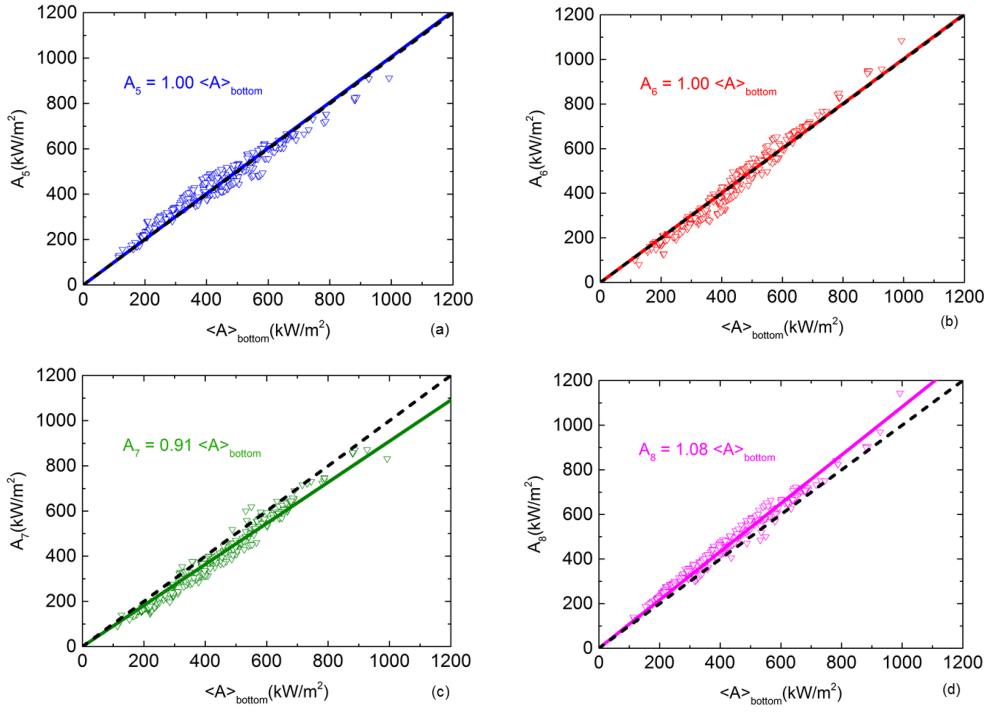

Figure 72: Amplitude of Gaussians fitting groups #5, #6, #7 and #8 vs average amplitude in the lower row for pulses in hydrogen. The solid lines give a fit to the data points (the open symbols). The black dashed lines represent the bisector of the first quadrant.

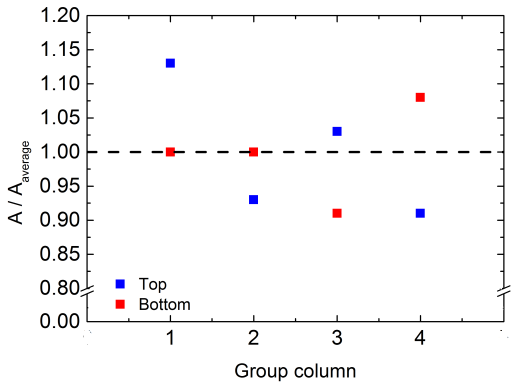

Figure 73: Ratio between the Gaussian amplitudes and their average along a row for pulses in hydrogen.

As mentioned above, these fluctuations of the angular coefficients (i.e of the amplitudes) could also be partially introduced by the fit. Because of the high superposition in fact, it is possible that some power is seen by the fit as coming from a group instead of from the neighbouring. Considering the spatial resolution of the calorimeter and the high superposition of the beamlet groups, this kind of error could be reasonable.

Similar results for the upper and lower part of the beam, were obtained in deuterium. They are shown in Figures 74 and 75.

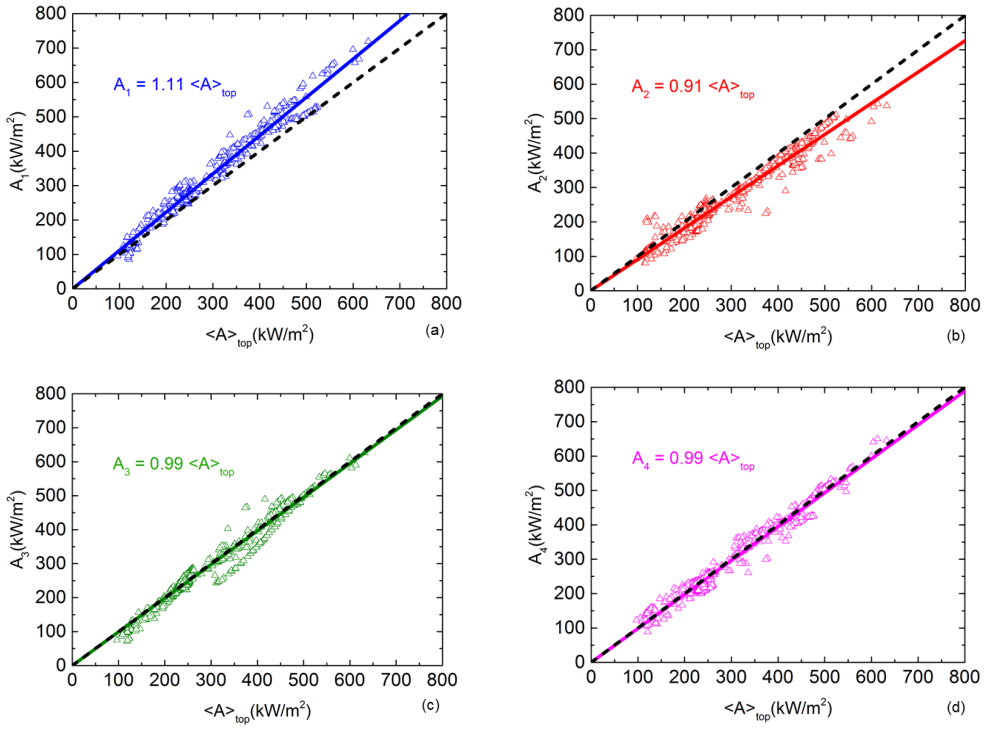

Figure 74: Amplitude of gaussians fitting groups #1, #2, #3 and #4 vs average amplitude in the upper row for pulses in deuterium. The solid lines give a fit to the data points (the open symbols). The black dashed lines represent the bisector of the first quadrant.

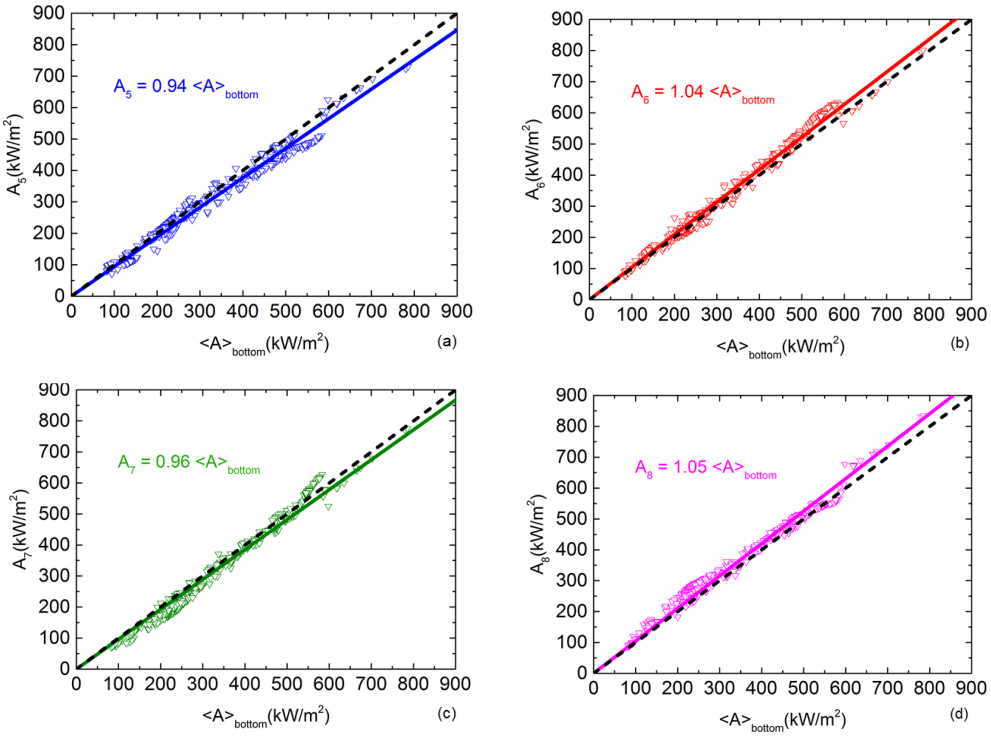

Figure 75: Amplitude of Gaussians fitting groups #5, #6, #7 and #8 vs average amplitude in the lower row for pulses in deuterium. The solid lines give a fit to the data points (the open symbols). The black dashed lines represent the bisector of the first quadrant.

The determined inhomogeneity in deuterium is slightly lower compared to hydrogen: 11 % within the upper row and 6 % within the lower one. Since in deuterium lower divergences are achieved than in hydrogen, this result is in agreement with the hypothesis of superposition as cause of larger fluctuations in the amplitudes determined by the fit, and so inhomogeneity.

From this analysis it can be deduced that the inhomogeneity within beamlet group rows, is in general quite close to the ITER requirements, especially in deuterium.

In order to further verify how divergence correlates with the beam inhomogeneity, a group of pulses performed in hydrogen with a low divergence (below 2.1° measured on LoS #3) has been selected. For these pulses the inhomogeneity within the upper row is reduced from 13 % to 7 % and the maximum difference between two close groups is reduced from 20% to 12% (see Figure 76). As further test, the trend of inhomogeneity within the upper row with respect to divergence measured on BES LoS #3 is shown in Figure 77. This result confirms that the inhomogeneity obtained from the fit grows with the beamlet divergence, which could be reasonably due to some limit in the fit.

The next section is dedicated to investigate the fit capability to determine a defined pattern of inhomogeneity (similar to the one of Figure 73). For this reason simulations of the same type as in section 5.2 will be performed for homogeneous and inhomogeneous beams with a large divergence.

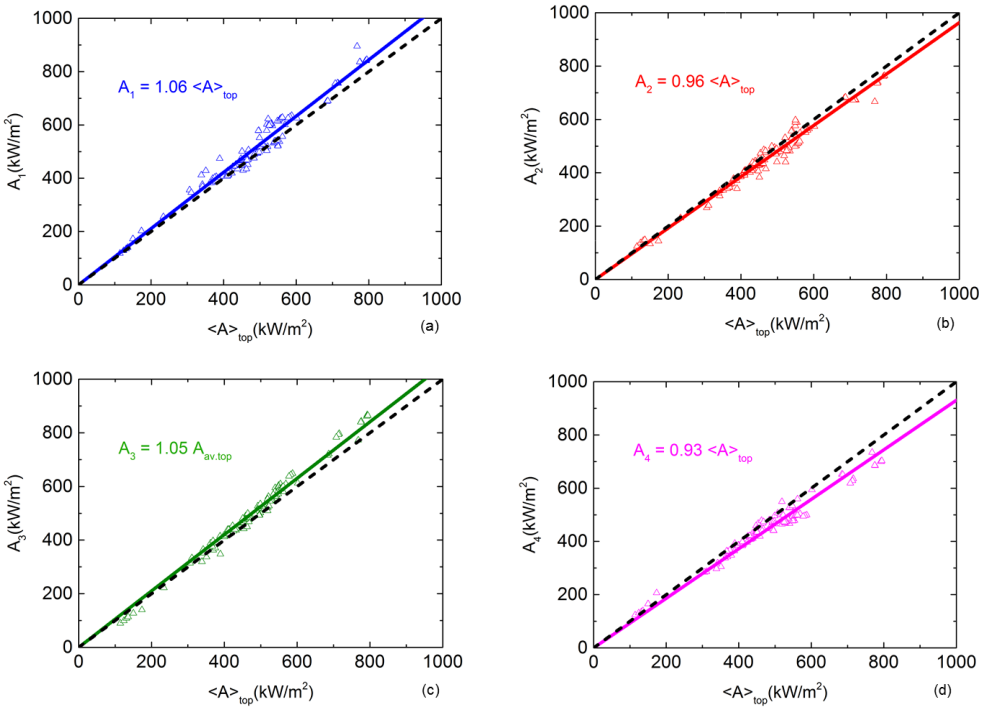

Figure 76: Amplitude of gaussians fitting groups #1, #2, #3 and #4 vs average amplitude in the upper row for pulses in hydrogen with divergence (measured on LoS #3) below 2.1°. The solid lines give a fit to the data points (the open symbols). The black dashed lines represent the bisector of the first quadrant.

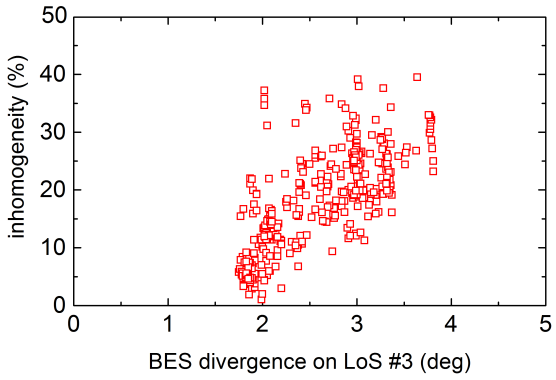

Figure 77: Inhomogeneity within the upper row from Gaussian fit to beamlet group vs measured divergence on LoS #3.

7.2 Fit sensitivity to inhomogeneity

In order to test whether the fit can really determine in a correct way the ratio between the beamlet group power density at large divergence, some simulations were performed in which an inhomogeneity of 10 % was assumed. Following the scheme of Figure 73, the power of the beamlets of groups #1, #3, #6 and #8 have been set to a value larger than the average, its 110 %, while the power of the beamlets of the other groups was set to the 90% of the average. The resulting 1D profiles of power density along a vertical

(x = -8 cm) and a horizontal (y = 20 cm) for a divergence $\delta = 3.5°$ are given in Figure 78. It has to be noted that in principle, power and divergence are related, since a larger current (i.e. power) means a larger perveance and therefore a different divergence (smaller in the under-perveant region). This effect is not taken into account in this simulation, whose only objective is to test the fit in large overlap conditions.

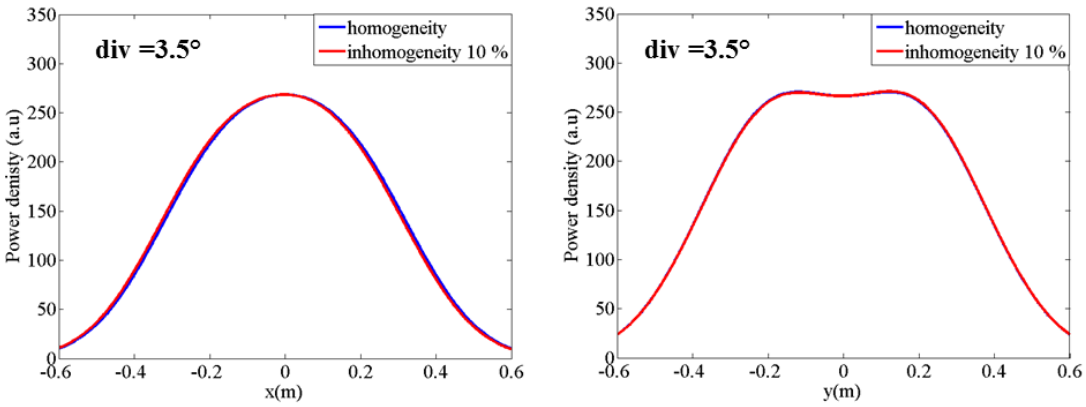

Figure 78: Simulation of the expected 1D power density profiles along the horizontal line y = 20 cm (left) and the vertical line x = -8 cm (right) for a completely homogeneous beam (in blue) and a beam with an inhomogeneity of 10 % (in red). Divergence is set to $\delta = 3.5°$.

The 1D profiles are quite superimposed (especially the vertical ones), but the fit can still discriminate the different amplitudes (see Table 8).

In a mirrored configuration, in which groups #1, #3, #6 and #8 have a current density equal to the 90 % of the average and the others have a current density equal to the 110 % of the average, specular results are achieved.

Parameters	**Simulation input (%)**	**Fit output (%)**
$A_1/ < A >$	110	(110.1±0.2)
$A_2/ < A >$	90	(89.9±0.2)
$A_3/ < A >$	110	(110.1±0.2)
$A_4/ < A >$	90	(89.9±0.2)
$A_5/ < A >$	90	(89.9±0.2)
$A_6/ < A >$	110	(110.1±0.2
$A_7/ < A >$	90	(89.9±0.2)
$A_8/ < A >$	110	(110.1±0.2)

Table 8: Simulation of a inhomogeneous beam with divergence 3.5°. Left column: Percentage of the average beamlet group power $< A >$ assigned to each beamlet group. Right: Amplitudes of the Gaussians fitting the data normalised to 100.

This result suggests that the average level of inhomogeneity which is found by the fit can be considered meaningful, and that the discussed fluctuation between the amplitudes of neighbouring groups could be real. This means that the dependence of inhomogeneity on divergence, shown in Figure 77, is probably due to some other effects, that still have to be investigated. In particular, new analysis should be performed to see whether inhomogeneity can be related to some source parameters.

7.3 Macroscopic homogeneity

While on a local scale, as described in section 7.1, the beam shows some inhomogeneity, on a more global scale the beam could be said to be homogeneous. The comparison between the total power deposited by the beam in the upper and lower half of the calorimeter is shown, for both isotopes, in Figure 79.

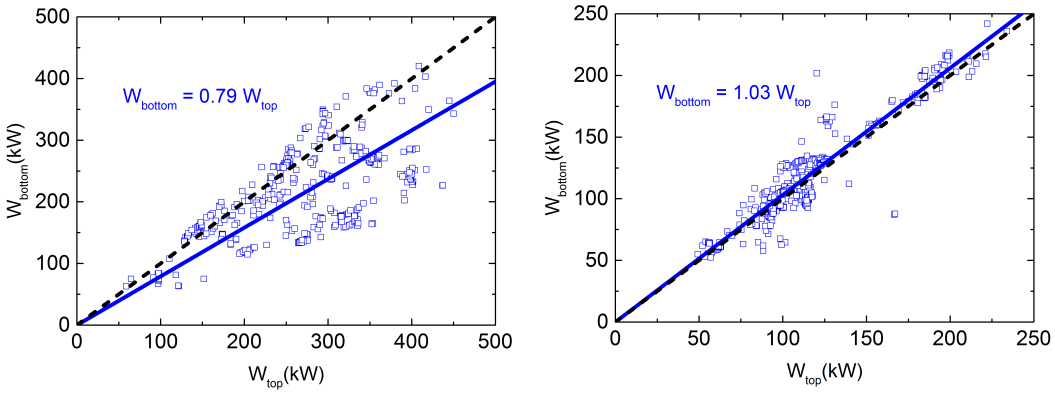

Figure 79: Total power within the bottom row of beamlet groups vs total power within the top row, as resulting from the fit of the IR camera data. The blue solid line gives a fit to the data points (the open symbols) and the black dashed lines represent the bisector of the first quadrant. Left: Hydrogen. Right: Deuterium.

The data in hydrogen (on the left-hand side of the picture) are quite broad, probably due to different source conditioning, and what results from a fit to the data points is that the upper part of the beam has a larger power. In deuterium instead (on the right-hand side of the picture), an almost perfect symmetry holds.

In Figure 80 the total power in the two left beamlet group columns is compared to that in the two right ones.

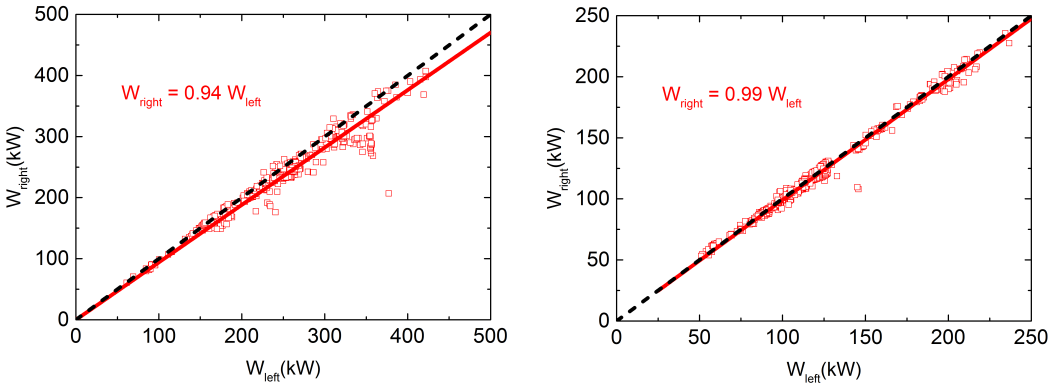

Figure 80: Total power within the two right columns of beamlet groups vs total power within the two left columns, as resulting from the fit of the IR camera data. The red solid line gives a fit to the data points (the open symbols) and the black dashed lines represent the bisector of the first quadrant. Left: Hydrogen. Right: Deuterium.

Between left and right side of the beam a very good symmetry holds. A good level of symmetry is shown also between inner and outer part of the beam, even if a slightly larger

power is found in the external groups, as shown in Figure 81.

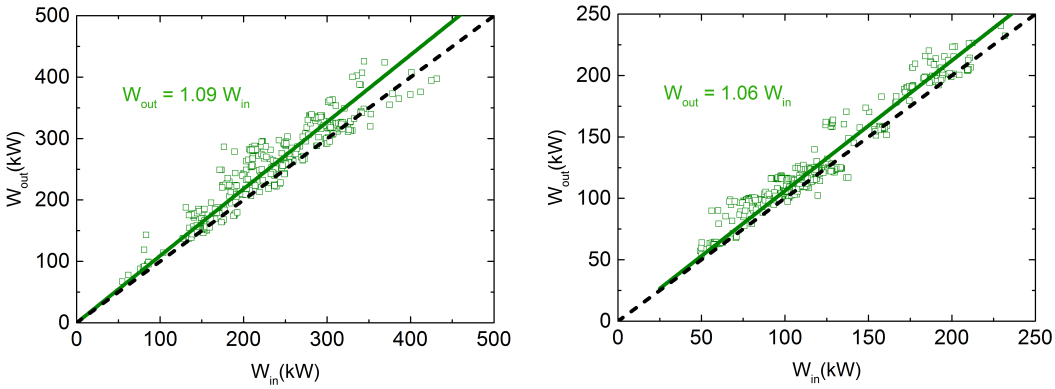

Figure 81: Total power within the two inner columns of beamlet groups vs total power within the two outer columns, as resulting from the fit of the IR camera data. The green solid line gives a fit to the data points (the open symbols) and the black dashed lines represent the bisector of the first quadrant. Left: Hydrogen. Right: Deuterium.

In summary, ELISE beam can in general be considered homogeneous on a global scale but some disuniformities occur between the beamlet groups. These inhomogeneities, which in average are not large (up to 13 %) tend to increase with the beamlet divergence. The reason for this trend is still under investigation.

8 Conclusions

8.1 Summary and conclusions

The main task of this thesis is to characterise the negative ion beam of the test facility ELISE, determining its divergence and homogeneity, by means of infrared images of its diagnostic calorimeter. The ELISE beam is made of eight beamlet groups, each formed by 5×16 beamlets. The beamlet groups are arranged in two rows.

The calorimeter is made out of copper and is formed by 30×30 blocks. It is equipped with 48 thermocouples and in order to increase its reflectivity it was covered with a black coating, whose emissivity was not precisely known. In the beam-on phase the temperature of the calorimeter may become really high (in the order of 300-400 °C), so it is cooled down from its back side by a water cooling system, that allows calorimetric estimates of the deposited power.

This thesis work started by the development of a software in BASIC to access the binary files produced by the IR camera. Once the pixel data were extracted and converted into temperature, they were averaged over the different blocks of the calorimeter.

Since the calorimeter is observed by the camera from a side port the IR image is distorted. For this reason the geometry of the calorimeter in the pixel coordinate system of the camera was determined and the appropriate pixels for the evaluation have been selected. Then, the camera was calibrated by finding the proper emissivity that had to be set for matching the temperature measurement from the thermocouples. After thorough analysis it was found that $\epsilon = 0.83$ represents a good average value to reproduce the thermocouple measurements. The performed analysis evidenced a slight decrease of the emissivity of the blackening layer in time caused by the influence of the beam on the coating.This suggests to monitor the coating erosion during time. The power deposition estimated by the IR thermography is in good agreement with water calorimetry, validating the calibration.

The analysis of the calorimeter data is based on fitting the power density matrix with eight Gaussian sub-beams, one for each beamlet group. The number of free parameters was set to 14: 8 amplitudes, two vertical coordinates (1 for each row of groups) and 4 widths (1 vertical and 1 horizontal for each row). The beamlet group horizontal coordinates were assumed to be the projection of the beamlet groups centers on the calorimeter surface. Gaussian amplitudes and widths allowed to assess inhomogeneity and divergence respectively. The vertical deflection of the beam due to the magnetic filter field was determined from the vertical position of the two rows of Gaussian used to fit the beamlet group.

In order to define a relation between the beamlet divergence and the widths of the fitting Gaussians some simulations of the beam as superposition of 640 Gaussian beamlets of given divergence were performed in IDL. The capability of the fit to give information about the beamlet divergence was verified by comparing the scaling of the Gaussian widths with the divergence determined by beam emission spectroscopy (BES), currently the beam diagnostic providing the best divergence measurement, and with the measured perveance. The results of these benchmark tests were positive: the widths of the Gaussians used for fitting the beamlet groups increase with increasing divergence. Thus a direct comparison between the two diagnostics was carried out. In this comparison the calorimeter measurements of divergence turned out to be about the 20-30 % larger than the ones from the BES.

A possible explanation for this result is that, where BES measurement takes place, i.e. about 2 meters downstream the grounded grid, the beam is not fully space charge compensated and so its divergence increases in the region between the BES lines of sight and the calorimeter surface. This effect could be reasonable since the pressure in the ELISE tank is quite low, about 10^{-4} mbar during the pulses.

Finally the fit capability to satisfactorily determine the beam inhomogeneity at large divergence was verified and the beam was determined to be mainly homogeneous and within the ITER requirements on a global scale, even if some local inhomogeneities have been identified. Beam inhomogenity was found to increase for larger divergences, but finding an explanation for this trend is still ongoing work.

Also the vertical deflection of the beam was assessed and its increase for increasing strength of the magnetic filter field was verified, even if some differences have been found between the deflections of the upper and the lower half of the beam. A very interesting result is represented by the correlation that was found between the vertical deflection of the negative ion beam (at fixed magnetic field) and the beam perveance. This result was verified both in hydrogen and in deuterium.

A possible explanation for this correlation is that, for perveances smaller than the perveance optimum, a decrease of perveance means an increase of divergence and, by thinking at the beamlets, this means that the beamlet path is closer to the edge of the plasma grid aperture. Since the magnetic filter field is realised by means of a current flowing through the plasma grid, this implies that the beamlet experiences a larger magnetic field and therefore is more deflected.

8.2 Future developments

This thesis work is the first characterisation of ELISE beam by means of its diagnostic calorimeter; the present results can certainly be enriched by future studies along the following lines. The under-estimation of the beamlet divergence obtained by the calorimeter with respect to the beam emission spectroscopy will profit from a more thorough analysis of the diagnostic operation and of the data analysis. The hypothesis according to which the beam is not yet fully space charge compensated when its divergence is measured by the BES could be verified in the future by means of the tungsten-wire calorimeter, whose position downstream the grounded grid is closer to the position of the LoS used for BES, or by higher pressure operations. Meanwhile, beam simulations should be performed to achieve a deeper understanding of the beam properties, in particular concerning the hypothesis about the mechanism producing a dependence of the vertical deflection on perveance.

Also the underlined local inhomogeneities should be further investigated, especially in order to relate them to some parameters of the source, giving indications about possible ways to control the beam homogeneity in large negative ion sources.

The emissivity of the coating layer should be regularly checked, as the performed analysis shows that it slightly decrease in time. Finally the data analysis tested during this thesis should be soon implemented as automatic procedure to provide the ELISE operator with on-line information.

References

[1] M. Kikuchi, K. Lackner, M. Tran, *Fusion physics*, International Atomic Energy Agency, Vienna (2012).

[2] A. R. Chouduri, *The physics of fluids and plasmas*, Cambridge University Press (1998)

[3] J. D. Lawson, *Some criteria for a power producing thermonuclear reactor*, Proc. Phys. Soc. **B70**, 6 (1957)

[4] IPP official website, www.ipp.mpg.de

[5] R. J. Goldston *et al.*, *Energy confinement scaling in tokamaks: some implications of recent experiments with ohmic and strong auxiliary heating*, Plasma Phys. Control. Fusion **26**, 87-103 (1984)

[6] ITER official webstite, www.iter.org

[7] Japan Atomic Energy Agency (JAEA) official webstite, www.jaea.go.jp

[8] H. P. L. De Esch *et al.*, *The optimization of neutral beam for ignition and burn control on next step reactors*, Fus. Eng. Des. **26**, 589 (1995)

[9] T. Inoue *et al.*, *ITER R&D Auxiliary system: Neutral beam heating and current drive system*, Fusion Eng. Des. **55**, 291 (2001)

[10] M. Kuriyama *et al.*, *Operation of the negative-ion based NBI for JT-60U*, Fusion Eng. Des. **39-40**, 115-121 (1998)

[11] S. Krylov, R. S. Hemsworth, *Gas flow and related beam losses in the ITER neutral beam injector*, Fusion Eng. and Des. **81**, 2239 (2006)

[12] I. A. Soloshenko, *Space Charge Compensation of Technological Ion Beams*, IEEE transactions on Plasma Science **27**, No. 4, 1097 (1999)

[13] T.Inoue *et al.*, *Design of neutral beam system for ITER-FEAT*, Fusion Eng.Des. **56-57**, 517 (2001)

[14] W.Kraus *et al.*, *Long pulse H^- beam extraction with a RF driven ion source on a high power level*, Rev. Sci. Instrum. **81**, 02B110 (2010)

[15] W.Kraus *et al.*, *Long pulse large area beam extraction with a RF driven H^-/D^- source*, Rev. Sci. Instrum. **79**, 02C108 (2008)

[16] M.Taniguchi *et al.*, *Long pulse H^- ion beam acceleration in MeV accelerator*, Rev. Sci. Instrum. **81**, 02B101 (2010)

[17] J.Jacquinot *et al.*, *Progress on the heating and current drive systems for ITER*, Fusion Eng.Des. **84**, 125 (2009)

[18] T.Bonicelli *et al.*, *Review of the EU Activities in Preparation of ITER in the Field of EC Power Sources and NB System*, ITER 2-3Rd Proc. 21st IAEA Conference Chengdu, 16-21 October 2006

[19] P.Sonato *et al.*, *The ITER full size plasma source device design*, Fusion Eng. Des. **84**, 269 (2009)

[20] P.Sonato *et al.*, *Status of PRIMA, the test facility for ITER neutral beam injectors*, AIP Conf. Proc.1515, 549 (2013)

[21] S. Peruzzo *et al.*, *Thermal analyses for the design of the ITER-NBI arc driven ion source*, Fusion Eng. Des. **82**, 933-940 (2007)

[22] R. S. Hemsworth *et al.*, *Status of the ITER neutral bem injection system*, Rev. Sci. Instr. **79**, 02C109 (2008)

[23] E. Speth *et al.*, *Overview of the RF source development programme at IPP Garching*, Nucl. Fusion **46**, S220 (2006)

[24] L. Schiesko *et al.*, *Magnetic field dependence of the plasma properties in a negative hydrogen ion source for fusion*, Plasma Phys. Control. Fusion **54**, 105002 (2012)

[25] B. Heinemann *et al.*, *Design of the "half-size" ITER neutral beam source for the test facility ELISE*, Fusion Eng. Des. **84**, 915-922 (2009)

[26] M.Bacal *et al. Basic processes of negative ion production and destruction in sources and beams* , Rev. Sci. Instrum. **67** 1138 (1996)

[27] M.Bacal *Physics aspects of negative ion sources* , Nucl. Fusion **46**, S250 (2006)

[28] Yu. I. Belchenko *et al.*, *A powerful injector of neutrals with a surface-plasma source of negative ions*, Nuclear Fusion **14**, 113 (1974)

[29] U. Fantz *et al.*, *Diagnostics of the cesium amount in an RF negative ion source and the correlation with the extracted current density*, Fusion Eng. Des. **74**, 299-303 (2005)

[30] P. Franzen *et al.*, *Progress of the development of the IPP RF negative ion source for the ITER neutral beam system*, Nucl. Fus **47**, 264 (2007)

[31] J. D. Callen, *Fundamentals of Plasma Physics*, University of Winsconsin, Madison (2003)

[32] G. Chitarin *et al.*, *Flexible magnetic design of the MITICA plasma source and accelerator*, AIP Conf. Proc. 1515, 217 (2013)

[33] P. Franzen *et al.*, *Progress of the ELISE Test Facility: Results of Cesium Operation with low RF Power*, submitted to Nucl. Fusion

[34] P. Agostinetti *et al.*, *Design of a low voltage, high current extraction system for the ITER Ion Source*, AIP Conference Proceedings **1097**, 325 (2009).

[35] R. Gutser *et al.*, *Negative hydrogen ion transport in RF-driven ion sources for ITER NBI*, Plasma Phys. Control. Fusion **51**, 045005 (2009)

[36] I. Brown, *The physics and technology of ion sources* (2003)

[37] U. Fantz *et al.*, *Physical performance analysis and progress of the development of the negative ion RF source for the ITER NBI system*, Nucl. Fusion **49**, 125007 (2009)

[38] B. Heinemann *et al.*, *The negative ion source test facility ELISE*, Fusion Eng. Des. **86**, 768-771 (2011)

[39] W. Kraus *et al.*, *The development of the radio frequency driven negative ion source for neutral beam injectors*, Rev. Sci. Instrum. **83**, 02B104 (2013)

[40] B. Heinemann *et al.*, *Negative ion test facility ELISE-Status and first results* Fusion Eng. Des. **88**, 512-516 (2013)

[41] R. Nocentini *et al.*, Fus. Eng. Des. **84**, 2131-2135 (2009)

[42] P. Franzen *et al.*, *Commissioning and first results of the ITER-relevant negative ion beam test facility ELISE*, Fusion Eng. Des. **88**, 3132-3140 (2013)

[43] P. Franzen *et al.*, *On the electron extraction in a large RF-driven negative hydrogen ion source for the ITER NBI system*, Plasma Phys. Control. Fusion **56** 025007 (2014)

[44] R. Nocentini *et al.*, *Beam diagnostic tools for the negative hydrogen ion source test facility ELISE* Fusion Eng. Des. **88**, 913-917 (2013)

[45] F. Bonomo *et al.*, *Infra-Red (IR) measurements of the beam calorimeter surface in the ELISE test facility*, Report RFX _ SPIDER _ TN _ 306, 2008-45-R01.00, F4E-RFX-PMS _ A-WP-2013, Deliverable T3.3/P1 (2013)

[46] P. Franzen, B. Ruf, *Beam modeling*, Final report F4E-GRT-313-Subtask5.4 (2011)

[47] B. Ruf, *Reconstruction of Negative Hydrogen Ion Beam Properties from Beamlin Diagnostics*, Ph. D. thesis, University of Augsburg (2014)

[48] FLIR Systems, *ThermoVision SDK, User's manual*, Program version 2.6 SP2 (2013)

[49] F. Bonomo, M. Barbisan, S. Cristofaro, B. Ruf, *et al.*, *BATMAN Beam Properties Characterization By The Beam Emission Spectroscopy Diagnostic*, 4th International Symposium on Negative Ions, Beams and Sources (NIBS 2014), 6 - 10 October 2014, IPP Garching, Germany

Acknowledgements

The first two people I would like to thank are my parents, to whom I "dedicate" this thesis, for their support in all of my choices, even when I was running out of enthusiasm. Then I thank Dr. Gianluigi Serianni, as a supervisor and as a person. For his constant supervision, even from Italy, for reading my thesis many times, providing very useful suggestions for its improvement, and for the interest he has shown for me as a person in the various sincere discussions we had in the last months. Then I thank all the IPP NBI group, physicists, engineers and technicians. As first I thank Prof. Ursel Fantz for giving me the opportunity to work in her group for my master thesis and for all her suggestions, always very precise and useful. I thank Dr. Peter Franzen for his supervision and availability, for reading my thesis in a record time and helping me to make my writing more precise. I thank Dr. Dirk Wünderlich for the help he gave me with BASIC and in the revision phase. I want to thank Dr. Riccardo Nocentini, the "father" of the diagnostic calorimeter, Frank Fackert and Dr. Rudolf Riedl, for all the patience they have shown with all the technical questions I had. Then I thank Benjamin Ruf for answering all my questions about the BES. A special thank goes to Dr. Federica Bonomo for her daily presence, as a physicist, but in particular as a person to speak with and to (why not?) loudly laugh together, especially when the work was not going as we would have wished.

Ringraziamenti

Il primo ringraziamento non può non essere per i miei genitori, cui “dedico” questa tesi, per avermi sempre sostenuto e assecondato nelle mie scelte anche quando l’orizzonte non era limpido e l’entusiasmo veniva meno. Ringrazio mia mamma per i tanti sorrisi ma anche per i contrasti e mio papà per le sue parole ben dosate, sempre le più sagge e vere nei momenti difficili.

Ringrazio poi il Dr. Gianluigi Serianni, come relatore e come persona. Per la sua supervisione costante, anche a distanza, per aver letto e riletto la mia tesi fornendo sempre suggerimenti costruttivi e utili al suo miglioramento e per l’interesse dimostrato verso di me come persona, nei vari momenti di confronto sincero che abbiamo condiviso.

Ringrazio poi tutto il gruppo NBI di IPP, fisici ingegneri e tecnici, in primis la Prof. Ursel Fantz per avermi concesso l’occasione di svolgere questa tesi all’interno del suo gruppo, e per le sue osservazioni sempre utili e puntuali. Ringrazio il Dr. Peter Franzen per la sua supervisione, la sua disponibilità, i suoi suggerimenti e per una serie di massime sul pragmatismo che difficilmente potrò dimenticare, oltre che per aver letto la mia tesi in tempo record emendandola da molti errori. Ringrazio il Dr. Dirk Wünderlich che, sempre pronto a rispondere a qualsiasi domanda su BASIC e sulla programmazione, si è rivelato preziosissimo per la parte più squisitamente informatica della tesi oltre che nella sua revisione. Ci tengo poi a ringraziare il Dr. Riccardo Nocentini, il “padre” del calorimetro diagnostico, sempre disponibile a soddisfare tutte le mie curiosità, Frank Fackert e il Dr. Rudolf Riedl per la pazienza con cui hanno affrontato tutte le questioni tecniche che ho loro sottoposto. Un grazie va poi a Benjamin Ruf per aver risposto puntualmente a tutti i miei quesiti sul funzionamento della BES. Dulcis in fundo ci tengo a ringraziare la Dr.ssa Federica Bonomo per la sua presenza quotidiana, come fisico, ma soprattutto come persona con cui confrontarsi e condividere, perchè no, qualche grassa risata, anche e soprattutto quando le cose andavano meno bene.

Venendo a ringraziamenti più “profani”, ringrazio il mio guru e fratello per la sua minacciosa loquacità e mia sorella per i divertentissimi “lavori di concetto” condivisi. Ringrazio i Mussati, Alessandro, Davide e Filippo, i miei “tre amici al bar”. Per le cene, le feste, le spese al Pam, il treno delle 22:23, i poker, i tornei di freccette, le sfide a FIFA tra “zucchina-gamberetto” e “ketchup-mayonese”. E poi ancora le corsette, il campetto, le chiacchiere notturne (chi da sveglio, chi da dormiente), le bevute e le cantate su “quanto il mondo sia meraviglioso”.

Un grazie sincero va ai Gingi Bungi, come piace loro chiamarsi, in particolare alla Finez e al Trev. Alla prima (con un saluto da Giuseppe) per aver sopportato tutte quelle che le abbiamo combinato in questi anni. Al secondo, per le tante avventure condivise, dal “sei pollo” al Coda, e per avermi sempre aiutato, senza chiacchiere o retorica, a vedere il bicchiere mezzo pieno, anche quando io non vedevo nemmeno il bicchiere.

Un grazie va anche a Valeria Rinaldi, presenza costante dei miei anni universitari, per il suo affetto sincero, e per avermi sempre colmato di fiducia e spinto a migliorare. Ringrazio poi Valeria Girardello altra presenza e confronto costante da cui ho tratto grande beneficio.

Un grazie ai miei compagni di avventura universitaria, a quelli delle interminabili “cene fisici”, degli spritz al Carpe Diem, e alla ristretta cerchia degli scommettitori compulsivi. Un grazie dovuto va a Irene, per i suoi splendidi appunti, in grado di redimere sempre le mie lievi disattenzioni o rarissime assenze alle lezioni della prima mattinata, e per il suo sopracciglio alzato, rimprovero garbato e divertente. Non si possono poi non citare l’assenteista Massimiliano, l’esperto sentimentale Emanuele, il mio compagno "terroncello"

Mattia e la Musa ispiratrice Alessio, per avermi concesso di cantare spesso le sue gesta nelle interminabili prese dati in laboratorio, oltre che per essere il principale (s)oggetto di scommesse. Ci tengo poi a ringraziare Nello il "procrastinatore" (al secolo Andrea Bertolucci) per le risate scomposte, le spiegazioni molto... alla mano (vedasi la moltiplicazione alla Townsend), per la sua sconfinata conoscenza della lingua italiana e e per aver condiviso con me le esperienze di laboratorio meno riuscite della storia del dipartimento. Ringrazio poi Alessandro Mimo, per la disponibilità e la leggerezza mai superficiale che lo contraddistinguono, per i suoi racconti in cui la realtà supera la fantasia, per gli "oggi diverge", i "gli dici di no" e gli "adesso andiamo al bar?", per le ricerche astruse in aula informatica e le canzoni "scritte" insieme per il nostro amico Nello. Un grazie speciale va poi a Sofia, con cui ho condiviso l'esperienza dell'Erasmus. Per avermi sopportato quotidianamente, per le chiacchiere su tutto, sogni, dubbi e paure nell'arco di questi sei mesi. Per la sua infinitamente superiore predisposizione informatica, soprattutto verso Latex, senza la quale questa tesi avrebbe richiesto molto più tempo per venire alla luce.